Optical Coherence Tomography: Monte Carlo Simulation and Improvement by Optical Amplification

Andreas Tycho

2 April 2002

Contents

Abstract

An advanced novel Monte Carlo simulation model of the detection process of an optical coherence tomography (OCT) system is presented. For the first time it is shown analytically that the applicability of the incoherent Monte Carlo approach to model the heterodyne detection process of an OCT system is firmly justified. This is obtained by calculating the heterodyne mixing of the reference and sample beams in a plane conjugate to the discontinuity in the sample probed by the system. Using this approach, a novel expression for the OCT signal is derived, which only depends upon the intensity distribution of the light from the sample and the reference beam. To adequately estimate the intensity distributions, a novel method of modeling a focused Gaussian beam using Monte Carlo simulation is developed. This method is then combined with the derived expression for the OCT signal into a new Monte Carlo model of the OCT signal. The OCT signal from a scattering medium are obtained for several beam and sample geometries using the new Monte Carlo model, and when comparing to results of an analytical model based on the extended Huygens-Fresnel principle excellent agreement is obtained. With the greater flexibility of Monte Carlo simulations, this new model is demonstrated to be excellent as a numerical phantom, i.e., as a substitute for otherwise difficult experiments. Finally, a new model of the signal-to-noise ratio (SNR) of an OCT system with optical amplification of the light reflected from the sample is derived, and discussed. Using this model, the conclusion is reached that an optical amplifier will enable substantial improvement of the SNR for OCT systems dominated by receiver noise. Receiver noise is of practical concern because of the (often) limited irradiance of suitable optical sources for OCT, and high insertion loss of the fast optical delay-line scanners that are necessary for fast imaging. Correspondingly, an increase in penetration depth of about 30-100% is demonstrated for OCT imaging in skin based on results obtained with the new Monte Carlo model. Accordingly, the two new models are demonstrated as valuable tools for future development and optimization of OCT systems to extend the applications of the system in biomedicine.

Dansk abstrakt

En ny avanceret Monte Carlo simulerings model af detektions processen i et optisk kohærensen tomografi (eng. OCT) system bliver præsenteret. For første gang vises det analytisk, at den inkohærente Monte Carlo metode kan anvendes til at modellere den heterodyne detektions proces i et OCT system. Dette opnås ved at beregne den heterodyne blanding af lyset fra objektet og referencen i det konjugerede plane til diskontinuiteten i objektet. Ved hjælp af denne metode udledes et nyt udtryk for OCT signalet, der kun afhænger af intensitetsfordelingen af lyset fra hhv. referencen og objektet. En ny metode til at simulere fokuserede Gaussiske stråler ved hjælp af Monte Carlo simulering er udviklet, for at kunne estimere disse intensitetsfordelinger korrekt. Denne metode er så kombineret med det nye analytiske udtryk i en Monte Carlo model af OCT signalet. OCT signal er modelleret for en række forskellige stråle- og objektgeometrier, og disse resultater er i god overensstemmelse med resultater fra en analytisk model baseret på det såkaldte udvidede Huygens-Fresnel princip. Med Monte Carlo metodens store fleksibilitet er den nye model velegnet som et numerisk fantom, dvs. som erstatning for ellers komplicerede eksperimenter, hvilket demonstreres i flere eksempler. Endelig er en ny model af signal-støj-forholdet for et OCT system med optisk forstærkning af lyset fra objektet udlet og diskuteret. En hovedkonklusion af denne model er, at signal-støj-forholdet kan forbedres væsentligt ved hjælp af optisk forstærkning, i systemer hvor støjen er domineret af den elektriske støj i detektor systemet. Elektrisk støj kan være vigtig for OCT, hvor styrken af gode lyskilder ofte er begrænset, og hvor der er et ganske betragteligt tab i de hurtige reference skannere, der er nødvendige for at opnå høje billedhastigheder. Det øgede signal-støj-forhold resulterer i en øget indtrængningsdybde for OCT systemet på ca. 30-100% i hud beregnet ved hjælp af den nye Monte Carlo model. De to nye modeller har dermed demonstreret deres værdi som praktiske værktøjer til den fremtidige udvikling og optimering af OCT systemer nødvendig, for at kunne udvide anvendelserne indenfor biomedicinsk optik.

Preface

The present thesis describes the work carried out during the period October 1998 to April 2002 at the Optics and Fluid Dynamics Department at Risø National Laboratory, Roskilde and Research Center COM, at The Technical University of Denmark, Lyngby where I was enrolled as a Ph.D. student. The project has been financed by The Technical University of Denmark, and The Center for Biomedical Optics and New Laser systems. The Ph.D. thesis work has been supervised by:

- Anders O. Bjarklev, Professor, Research Center COM, Technical University of Denmark, Lyngby.
- Peter. E. Andersen, Senior Scientist, Risø National Laboratory, Roskilde.

I would like to express my sincere gratitude to my supervisors for their kind help and continuing support during this project. I have truly enjoyed our close relations. A special thanks to Thomas M. Jørgensen from Risø National Laboratory for the close collaboration in developing the Monte Carlo model presented in this thesis, and for the many discussions of the intricacies of modeling heterodyne detection using Monte simulations. This collaboration had a great impact on the enjoyment of working with the subject during an extensive part of the Ph.D. project. Also a special thanks to Harold T. Yura from the Aerospace Corporation, USA who introduced me to the extended Huygens-Fresnel formalism and considerably contributed to this part of the theoretical analysis in this thesis. Finally, I want to thank Ida Knudsen for valuable comments on this thesis and for just being there.

I also take the opportunity to thank:

- Steen G. Hanson, Risø National Laboratory for discussions of heterodyne detection.
- Peter S. Jensen, Risø National Laboratory for always being very helpful and for many valuable discussions during the afternoon coffee break.

- Lars Thrane, Risø National Laboratory for good collaboration and fruitful discussions.

- Finn Petersen, Risø National Laboratory for valuable assistance in the lab.

- Leif Oxenløwe, Technical University of Denmark for help in the laboratory at Research Center COM.

- René S. Hansen, Risø National Laboratory for discussions of noise.

- Morten G. Dyndgaard, Technical University of Denmark for making sharing an office a positive thing and always being helpful.

Finally, I would like to thank the rest of my colleagues at Research Center COM at the Technical University of Denmark and in the Optics and Fluids Dynamics Department at Risø National Laboratory for good interactions.

Andreas Tycho, Marts 2002.

List of Publications This Ph.D. work has resulted in the following publications:

Papers:

- A. Tycho, T.M. Jørgensen, H.T. Yura, and P.E. Andersen, "Derivation of a Monte Carlo method for modeling heterodyne detection in optical coherence tomography systems", Submitted for publication, Appl. Opt., January 2002.
- A. Tycho and T.M. Jørgensen, "Comment on "Excitation with a focused, pulsed optical beam in scattering media: Diffraction effects", Accepted for publication in Appl. Opt., 2001.
- A. Tycho, T. M. Jørgensen, and L. Thrane, "Investigating the focusing problem in OCT: comparison of Monte Carlo simulations, the extended Huygens-Fresnel principle and experiments", SPIE Proc. **3915**, 25-35 (2000).
- P. E. Andersen, L. Thrane, H. T. Yura, A. Tycho, and T. M. Jørgensen, "Modeling The Optical Coherence Tomography Geometry Using The Extended Huygens-Fresnel Principle And Monte Carlo Simulations [invited paper]", SPIE Proc. **3914**, 394-406 (2000).
- A. Tycho, "Modeling of a focused beam in a semi-infinite highly scattering medium," SPIE **3597**, pp. 118-129 (1999).

Patents

- PCT/DK01/00573: "Optical amplification in coherence reflectometry", filed in the PCT system September 2001 (Danish patent application, September 2000). Inventors (alphabetically):P.E. Andersen, A. O. Bjarklev, and A. Tycho
- PCT/DK01/00721 (WO 02/21074 A2): "Optical amplification in coherent optical frequency modulated continuous wave reflectometry", filed in the PCT system October 2001 (Danish patent applica-

tion, October 2000). Inventors (alphabetically):P.E. Andersen, A. O. Bjarklev, and A. Tycho

Chapter 1

Introduction

Through the last decade, optical coherence tomography [1] (OCT) has received increased attention. This technique is viewed by many as a promising technique for a plethora of applications, especially within the area of biomedical optics [2]. OCT is an imaging technique which can obtain high-resolution cross-sectional tomographic images of microstructures within transparent and semi-transparent media with micrometer resolution. Such media may be biological tissue, polymer materials, paints etc.

OCT is an extension of optical low-coherence reflectometry (OLCR) [3, 4], which is a one-dimensional ranging technique applied to investigations of fiber-based or integrated waveguide devices (see e.g. Refs. [5–8]). The OLCR technique was transferred to the field of biomedical optics for ranging of the retina [9, 10] and other eye structures [9–11]. Then, by adding transverse scanning of the probe beam relative to the sample, D. Huang *et al.* [1] extended this technique to the two- or three-dimensional tomographic imaging modality OCT. An OCT image is a compilation of one-dimensional ranging scans, which provide a map of the reflectivity of the sample.

A schematic of an OCT system similar to the original OCT system [1] is shown in Fig. 1.1. The system is a fiber-optic Michelson interferometer where the light from a broadband light source[1] is coupled into a fiber-optic 50/50 coupler, which splits the light into the sample and reference arms.

[1] Broadband is in this context usually several tens of nm optical bandwidth.

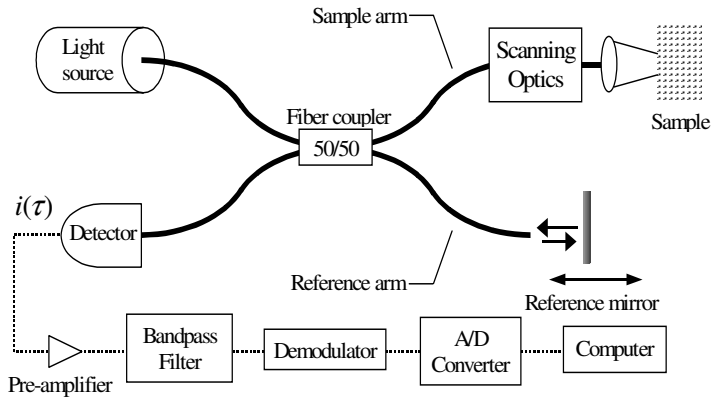

Figure 1.1: Schematic of an OCT system similar to the original system [1]. Solid lines are fiber-optic connections, whereas dotted lines are electrical connections.

The light exiting the sample arm is focused into the sample, and retroreflected light is collected back into the fiber. This light is then combined, at the detector, with the light reflected by the scanning reference mirror. A longitudinal scan is performed by scanning the position of the reference mirror and recording the interference signal. Individual reflections are distinguishable because interference only occurs when the difference in optical path length between the two arms is within the coherence length of the light source. The electrical signal obtained during the reference scan is amplified, bandpass filtered, demodulated, and finally stored on a computer in digital form. The image data is then displayed by assigning a color or tone of gray to each reflection according to the measured signal strength.

The signal from a single reflection in the sample is given by the interference term at the detector, which is proportional to [12–14]

$$i(\tau) \propto \mathrm{Re}\left[F\left\{S(\nu)\right\}\right] \cos\left(2\pi\nu_c\tau\right), \tag{1.1}$$

where $i(\tau)$ is the signal current as a function of the optical time delay, τ, ν_c is the center frequency of the source, and $F\{S(\nu)\}$ is the Fourier transform of the spectrum of the light source with argument τ. Here it has been used that the interference term is an autocorrelation of the emitted source spectrum. From Eq.1.1 it follows that the shape and width of the

source spectrum are important properties for OCT. Firstly, a wide source spectrum will result in a narrow autocorrelation and therefore yield a high axial resolution of the system. Secondly, if the Fourier transform of the source spectrum results in sidelobes, such effects may be difficult to distinguish from a signal due to a different reflection site. A Gaussian spectrum is an example of an ideal spectral shape. If such a source has a full-width-half-maximum (FWHM) bandwidth, $\Delta\lambda$, and a center wavelength λ_c, the coherence length, l_c, or axial resolution (in free space) is given by [2,14–16]

$$l_c = \frac{2\ln 2}{\pi}\frac{\lambda_c^2}{\Delta\lambda}. \tag{1.2}$$

Another, very similar, definition of the coherence length is sometimes used [13,17], but will not be discussed further here.

The light source of the first OCT system was a superluminescent diode with a coherence length of 17 μm and a center wavelength of 830 nm [1]. Light sources in the near-infrared region are suitable for biological applications because of the reduced tissue absorption in this region. Superluminescent diodes are well-established as light sources for OCT because of their relative high irradiance, smooth and wide spectrum combined with a relatively low cost [18]. However, the coherence length of superluminescent diodes, which is typically 10-20 μm, is insufficient to image individual tissue cells and cell nuclei. Such resolution has been identified as important for applications such as identification of malignant melanoma (skin cancer) [19]. Several other types of light sources have been applied to OCT [18]. Only a Ti:sapphire femtosecond laser has been demonstrated capable of producing the 1 μm resolution required to accurately image subcellular structures [20,21], although a Cr^{4+}:fosferite femtosecond laser has been shown to come close ($l_c \sim 6\,\mu$m) [22]. However the current cost and complexity solid-state laser makes their use impractical outside of a research setting [18]. Please refer to Refs. [16] and [18] for a comprehensive review of light sources for OCT. It is important to note that in a recent market study, where several leading scientists within the field where interviewed, lack of suitable high irradiance light sources were identified as a significant barrier for OCT technology [23].

In the original OCT system [1] reference scanning was performed using a stepper motor. Since then several scanning techniques have been employed in order to obtain (near) real-time imaging, because fast imaging is crucial in providing the clinician with flexible operation during *in situ* measurements [24]. It is also essential in avoiding image artifacts due to unavoidable movement in clinical measurements due to e.g. beating of the heart, involuntary muscular jittering, and micro movements in the eye [25]. Moreover, applications in sensitive areas, such as endoscopic investigations near the heart call for a fast collection of as much data as possible. The fastest reported optical delay-line scanner is based on a high-speed air turbine rotating a glass cube [25]. This scanner has a scan-speed of 176 m/s with a scan depth of 2 mm and a repetition rate of 28.5kHz, but the technique is still too unstable for practical use in OCT [26]. The present state-of-the-art OCT systems use a Fourier-domain rapid-scan optical delay line [27, 28], which, in these systems, obtain a scan depth of several millimeters with a repetition rate of a few kilohertz [14, 24, 29–31]. An important implication of fast scanning is the necessary increase in detection bandwidth B_e. As the signal-to-noise ratio (SNR) of an OCT system is inversely proportional to the detection bandwidth, an increase in scanning speed will reduce the SNR of the system. An additional decrease in SNR is also expected because fast detector systems are likely to contribute with more noise [32]. Accordingly, an increase in scanning speed must be countered by an effort to increase the SNR in order to maintain image penetration depth and contrast. For a reference scanner, which simply changes the path length of the light[2], the center frequency, ν_c, and the necessary electrical bandwidth, B_e, are given by [33]

$$\nu_\mathrm{c} = 2v/\lambda_\mathrm{c}, \tag{1.3}$$

$$B_\mathrm{e} = 2v\Delta\lambda/\lambda_\mathrm{c}^2, \tag{1.4}$$

[2]The center frequency of the beat signal can be controlled to some extent using the Fourier-domain rapid-scan optical delay line system. Therefore a relatively low center frequency may be maintained while still scanning fast. However, the center frequency varies through a scan and therefore a larger electrical bandwidth must be used, which reduces the SNR [26].

where v is the speed of the of the path length change. If, as an example, the reference is to scan 3 mm at 100 kHz with λ_c at 1300 nm and $\Delta\lambda$ is 100 nm, then ν_c becomes 460 MHz and whereas B_e is 36 MHz. For comparison, in a conventional OCT system using a translation stage, B_e is only a few kilohertz [17], and a system with a Fourier-domain rapid-scan optical delay line was reported to have a B_e of 2.6 MHz with 4kHz repetition rate. However, development of the field is toward yet faster scanning techniques [26]. For a thorough review of optical delay-line scanners in OCT, the reader is referred to Ref. [26].

The analysis of the SNR is important to enable the design of yet more effective systems with deeper penetration capabilities, as well as better contrast. Besides increasing the irradiance of the light source, which is not always possible, innovative designs of the interferometer may also provide a better SNR [31, 34–36]. Using balanced detection makes it possible to suppress intensity noise, which can be a significant source of noise caused by the large spectral width of the light source [37]. The benefits of balanced detection was recently discussed in a comparative analysis of balanced versus unbalanced detection systems [32]. Intensity and beat noise, as well as receiver noise, was included in this SNR analysis of OCT systems, whereas all previous analyses has assumed the system to be shot-noise limited [15, 38–40].

The lights interaction with the scattering sample, and how it thereafter results in a viable signal, is essential to the obtained resolution and SNR. This process has been investigated by several researchers [41–46]. However, not until an analytical model based on the so-called extended Huygens-Fresnel principle [47], published by Thrane *et al.* [48], has it been possible to include the effect of both single-scattered, and multiple-scattered light simultaneously. Accordingly, this model offers a far more complete description of the process of obtaining an OCT signal. In describing the light propagation in the sample, Thrane *et al.* [48] used the results of an earlier analytical model of Gaussian beam propagation through scattering media [49]. With this description, it is therefore also possible to investigate the properties of the focal spot inside the sample, which is essential for knowledge of the transverse resolution of the system.

The number of applications of OCT in medicine and other fields is vast [2]. However, commercially only a system for clinical examinations in ophthalmology exist (Zeiss-Humphrey Systems, Dublin, CA, USA). Several thousand patients have been examined using this system for noninvasive imaging of the anterior eye, crystalline lens, and retina. Imaging of highly scattering tissues is a topic of considerable interest, and several new companies have been established to develop systems in this area. The company Lightlab Imaging[3], is developing systems for endoscopic examination in cardiology and the gastrointestinal tract, whereas Isis-Optronics[4] aims its research primarily towards applications in dermatology (see Ref. [2] for a review of these applications). Imaging of non-transparent tissues is generally a difficult problem, primarily due to strong scattering, and the effect of multiple scattering on the OCT signal is not yet completely understood. However, the analytical model discussed above has significantly added to this understanding [48]. The preferred spectral region for imaging in highly scattering tissues is near 1.3 μm, where the effect of scattering is reduced compared to wavelengths in the visible, and the absorption (mainly due to water) is low compared to even longer wavelengths. Using light in the 1.3 μm region research has demonstrated imaging up to 2-3mm into the sample, depending on the tissue type [14, 50]. The reader may find a thorough review of the biomedical applications in Refs. [2, 50].

1.1 Scope of the thesis

The scope of this thesis is the analysis of OCT systems to aid improvement of the signal-to-noise ratio (SNR) and promote understanding of the detection of signals from highly scattering media such as dense tissue. This is accomplished by presenting two new models: An advanced Monte Carlo model of the OCT signal [51] and a detailed analytical noise model including optical amplification of the reflected light from the sample [52].

The motivation to develop a method of modeling OCT systems with a Monte Carlo model is that Monte Carlo simulations are well accepted as a

[3] LightLab Imaging, LCC. Westford, MA, USA: **www.lightlabimaging.com**
[4] Isis Optronics GMBH, Mannheim, Germany. **www.isis-optronics.de**

substitute for experiments, i.e., as a numerical phantom. With the inherent flexibility of the Monte Carlo simulation method, such a model may then be used as a supplement to the analytical model of OCT systems based on the extended Huygens-Fresnel principle discussed above [48]. The analytical model presented in Ref. [48] model will be referred to as the *analytical OCT model* in this thesis. The new Monte Carlo model may be applied to estimate the signal from sample structures, which are cumbersome to describe analytically or for which one or more of the assumptions of the analytical model fail. Finally, it may also be applied to corroborate the applicability of the analytical OCT model to sample structures, which are difficult to construct as phantoms in the laboratory. An important aspect of this thesis is thus to demonstrate the applicability of the incoherent Monte Carlo method to model the heterodyne detection process in an OCT system.

One potential method to enable faster scanning and deeper penetration depth of future OCT systems is to apply an optical amplifier to amplify the reflected light from the sample. However, to determine whether an optical amplifier will improve the SNR of practical OCT systems, a model must be constructed including all relevant parameters. Such a model must also, as a novelty, explicitly include the system constraints of detector saturation and a safety limit on the irradiation of the sample. The explicit inclusion of such limits in in general noise analysis not confined to the shot-noise limit is new to OCT analysis. Therefore, this new noise model may also be relevant for optimizing conventional OCT system. With the discussion of the importance and implications of faster scanning in the previous section, it is especially interesting to analyze the impact of optical amplification on fast scanning systems. The resulting model may then be applied by a systems designer to determine if, and how much, an optical amplifier will improve the SNR of a given system, and how to optimize this improvement. The new Monte Carlo model of the OCT signal may then be applied to quantify the increase in penetration depth for a specific application due to the expected increase in the SNR.

1.2 Organization of the thesis

In chapter 2 the applicability of incoherent Monte Carlo simulation method, in its most common usage, to model the heterodyne OCT signal from biological tissue is proven mathematically [51]. This is obtained by calculating the heterodyne mixing of the reference and sample beams in a plane conjugate to the discontinuity in the sample probed by the system. Using this approach, a novel expression for the OCT signal is derived, which only depends upon the intensity distribution of the light from the sample and the reference beam. This is a main result of this thesis that is essential to the validity of the presented Monte Carlo model of the OCT signal. To estimate the OCT signal using this result, a new method of modeling the propagation of a Gaussian beam using Monte Carlo simulation is required.

In chapter 3, the new method of modeling the propagation of a focused Gaussian beam using Monte Carlo simulation is presented [51, 53], and validated by obtaining excellent agreement with results obtained using a previously published analytical model [49]. Because intensity distributions of focused beams in random media are important to OCT (transverse resolution) and several other applications, the use of this new method as a numerical phantom is demonstrated.

In chapter 4, the results of the two previous chapters are combined to obtain a Monte Carlo model of the heterodyne detection process in an OCT system [51]. The mathematical results of chapter 2 are used to derive a so-called detection scheme, which is used to determine whether a single energy packet, simulated using the Monte Carlo simulation, contributes to the OCT signal. The new Monte Carlo model shows excellent agreement with results obtained using an analytical model based on the extended Huygens-Fresnel principle [48] for sample geometries where this model has been validated experimentally [17,48]. Finally, the applicability of the new Monte Carlo model of the OCT signal is demonstrated through examples.

In chapter 5, the applicability of an optical amplifier to improve the SNR of an OCT system is analyzed theoretically, and a new noise model of the system is presented [52]. First, the SNR of a conventional OCT system without optical amplification is analyzed, and it is found that, al-

though often inferred in the field, the shot-noise limit is only applicable in special cases. Using this analysis, and a theoretical model of an optical amplifier, it is identified when an optical amplifier will improve the SNR of an OCT system. Depending on the system and application, the optical power constraints of detector saturation and/or a safety limit on the irradiation of the sample may be important. Such constraints are therefore, as a novelty, considered explicitly in the model. From the complete model it is then possible to determine the applicability of optical amplification in a specific system, and to optimize the improvement.

The main part of chapter 6 is devoted to the quantification of the improvement obtained by using optical amplification in the fast scanning OCT systems discussed in section 1. This quantification is carried out for several cases of practical interest with resulting significant improvement of the SNR. It is then demonstrated how improvement in penetration depth, corresponding to an improvement of the SNR, may be quantified by applying the derived Monte Carlo model of the OCT signal. In the final section of chapter 6, the impact of an optical amplifier on the coherence of the amplified light and the resulting OCT signal is briefly discussed using results from a preliminary experiment.

Finally, it should be noted that during the research that led to this thesis, a similar SNR model has been derived for a special type of OCT systems, where the wavelength of a narrow band light source is scanned [54]. Such systems are not yet researched widely although the technique shows great promise. Due to the close similarity to the presented noise model of systems with a broadband light source, this analysis is not included in this thesis. The work is filed as a patent [55].

Chapter 2

Applicability of Monte Carlo simulation to OCT

In this chapter, the applicability of the incoherent Monte Carlo simulation method to model the heterodyne detection process in an optical coherence tomography (OCT) system [1] is proven mathematically [51]. This is accomplished by deriving an analytical expression for the signal depending only on the intensity of the light, and demonstrating that this expression is identical to that of an analytical model [48] based on the extended Huygens-Fresnel principle [49].

2.1 Introduction

Monte Carlo simulation [56] is a general technique, which has been applied to a wide variety of modeling efforts from nuclear fission to stock market analysis (see e.g. Refs. [57] and [58]). The name *Monte Carlo* refers to the gambling, i.e., stochastic, nature of the approach where a stochastic number generator is used to determine the specific outcome of a single realization of a random variable or collection of random variables [59, 60]. The expected value of the random variable is then determined by averaging over many such trials. For light propagation in random media, Monte Carlo simulation using a computer is equivalent to finding numerical solutions to the equation of radiative transfer [61] by tracing independent energy packets

each carrying a fraction of the total light energy [62, 63]. The scientific contributions to the field of Monte Carlo simulation of light propagation in tissue is vast. However, the most important landmarks may be listed as follows: Wilson *et al.* [63] were the first to apply the technique to laser light propagation in tissue. Flock *et al.* [64] demonstrated excellent agreement with experiments, whereas Prahl *et al.* [65] included anisotropic scattering and internal reflection in the random medium. Wang *et al.* [66] applied this work to develop a public domain computer code, MCML[1], capable of modeling light propagation in multiple layered slab geometries.

Monte Carlo simulation is simple and intuitive in nature, but in spite of this simplicity very few limitations upon the propagation geometries that can be modeled exists. Furthermore, with the recent advent of relatively cheap and powerful computers, the extensive computational power often required is no longer an obstacle. This, combined with a relatively high confidence in the results obtained using Monte Carlo simulation (see e.g. [64, 67–78]) has made the approach widely accepted as a numerical alternative to experiments, i.e., a numerical phantom. This may be seen from the publication of Monte Carlo simulations applied to a wide variety of applications for either validation and testing of a modeling approach (see e.g. [78–84]) or investigations into light-tissue effects and optimization of methods (see e.g. [82, 83, 85–88]).

With the demonstrated performance of Monte Carlo simulation in general, the motivation for developing a method of modeling OCT systems with Monte Carlo simulation is to obtain a flexible model which may be applied to complex sample structures with well-controlled properties. Such a model may then serve as a supplement, and numerical phantom, to the analytical model of an OCT system recently published by Thrane *et al.* [48]. As discussed in the main introduction, this analytical model is based upon the so-called extended Huygens-Fresnel principle and is, in this thesis, referred to as the analytical OCT model. While this model renders fast results and direct understanding of parameter dependencies, it is limited to

[1] Presently, the original ANSI C source code for the program MCML may be downloaded from Oregon Medical Laser Center at the web page: *http://omlc.ogi.edu/software/mc/*

propagation geometries which conform to the assumptions of highly forward scattering and which may be described by the $ABCD$ matrix formalism. The model was validated on a simple single-layered tissue phantom consisting of latex spheres in aqueous suspension [48], but with the incorporation of the $ABCD$ matrix formalism modeling of the OCT signal from more complex structures is possible. However, a validation of the model on such structures requires complex tissue phantoms with well-controlled properties which are, at best, difficult to produce. As the Monte Carlo simulation method is well-established for modeling light propagation through multiple layers [66, 67, 81, 86], a Monte Carlo model may be used as a reference for complex sample geometries if it can be shown to perform well for the simple sample geometries for which the analytical model is validated experimentally. The Monte Carlo model may also be used to model the signal from sample geometries which are cumbersome to describe analytically, or do not strictly conform to the assumptions of the analytical OCT model. These assumptions are reviewed in the next section.

2.1.1 Essentials of Monte Carlo simulation and photon packets: A review

To discuss the applicability of the Monte Carlo simulation method to modeling the detection process in an OCT system, the fundamentals of the commonly used approach to Monte Carlo simulation of light propagation in tissue are briefly reviewed (a more complete tutorial may be found in Ref. [89]): The simulation of each energy packet start by a launch, after which the packet follows a straight line until interaction with the sample medium. Due to the localization of the energy packet a decision must be taken for each distributed possibility the packet encounters, for example whether to be reflected or refracted by a surface of a refractive index mismatch. This is implemented by considering each set of possible outcome to a probability distribution, and then using a computer generated pseudo random number to decide which that is taken. The energy packet is traced through a random medium by determining the path length to the next interaction using a probability distribution related to the mean-free path in

the medium $L_{\mathrm{f}} = 1/\left(\mu_{\mathrm{s}} + \mu_{\mathrm{a}}\right)$, where μ_s is the scattering coefficient and μ_a is the absorption coefficient [61, 90]. Likewise, the direction of an energy packet after a scattering event is found using a probability distribution related to the so-called phase function[2] [91] or scattering function, $p\left(\theta, \varphi, g\right)$, where θ is the polar angle and φ the azimuthal angle to the direction of incidence upon the scatterer and g is the asymmetry parameter [90]. Accordingly, an energy packet experiences a continuously changing medium, and therefore an ensemble averaging over the random medium is obtained automatically by simulating many packets.[3] With each interaction, a fraction of the energy of the energy packet is absorbed and the trace of a packet ends when its energy falls below a set threshold or escapes the sample. If the sample is multilayered, the path between two interactions may be intersected by a layer interface which must be considered [66].

The energy packets discussed above are often referred to as photon packets or simply photons and this is adopted here. However, it should be emphasized that no underlying wave equation are guiding or governing these photons. Accordingly, any attempt to relate these to real quantum mechanical photons should be done with great care as argued in a recent comment by Tycho and Jørgensen [92] to a suggested approach of including diffraction effects into Monte Carlo simulations [93]. A Monte Carlo photon packet represent a fraction of the total light energy and for some, especially continuous wave, applications it may be useful to think of the path travelled by a photon as one possible path in which a fraction of the power flows. A collection of photon packets may then be perceived as constituting an intensity distribution due to an underlying field and it can, accordingly, seem tempting to infer behavior known to apply to fields upon photon packets. Consider, as an example, that one wishes to determine whether the photon packets are able to enter an optical fiber. It can then seem

[2] The name "phase function" is not related to the phase of the light. The name takes its origin from astronomy where it refers to the phases of the moon [91].

[3] It should be noted that there exists a different approach to Monte Carlo simulation than the one described here. In this approach, a realization of the random medium is constructed according to the bulk parameters, and then a large number of photon packets are traced through this realization. However, this approach is disadvantageous for modeling light propagation in tissue, because many realizations of the medium must be simulated to obtain an ensemble average for a given set of bulk parameters.

intuitive to restrict the access of photons impinging on the fiber-end to those which fall within the numerical aperture of the fiber. However, such an angular restriction may not be correct, because the individual photon packet do not carry information of the entire field and its phase distribution. It is therefore not possible to determine whether a portion of the energy carried by a photon packet will enter the fiber due to a mode match between the fiber mode and the field underlying the collective intensity distribution of the photon packets. This discussion will be given further consideration in chapter 4.

2.1.2 Monte Carlo simulation of heterodyne detection in OCT

With the above discussion in mind, it may seem futile to investigate if Monte Carlo simulation is applicable to estimate an OCT signal, which is the result of heterodyne mixing, and thus depends upon the coherence properties of the light. However, the problem may be reformulated to investigate wether or not the effect of the lack of coherence information in a Monte Carlo simulation may by circumvented, or at least minimized. In section 2.2, the extended Huygens-Fresnel principle is used to derive an expression for the OCT signal depending only on the intensity of the light. This is obtained by calculating the mixing of the reference and sample beams in the plane conjugate to the discontinuity in the sample probed by the system. The result is surprising, because the expression for the signal given in Ref. [48] depends on the coherence properties of the light. However, it is shown that the formula used for calculating the OCT signal in this plane is mathematically identical to the result presented in Ref. [48]. These results are valid for the, from a biomedical point of view, important case of a signal due to a diffusely reflecting discontinuity embedded in a scattering sample. As a novelty, this proves the viability of Monte Carlo simulation to model the OCT technique, because it is shown that only intensity, and not field and phase, is necessary for this special case.

An important assumption of the analytical OCT model is that scattering in the sample is assumed to be forward directed. With this assumption,

the relative time delay of the light, received from a single discontinuity plane in the sample, is assumed to be negligible compared to the coherence length of the light source [48]. At the same time, it is assumed that the coherence length of the light source is short enough that signal power from all other reflections may be neglected. This is equivalent to assuming that the coherence properties of the light source has no influence on the signal as long as the reference arm is matched to the diffuse discontinuity within the sample. This is a justified approximation for highly forward scattering tissues [94]. However, it does render the method unsuitable to investigate the effect of scattering on the axial resolution of an OCT system in general, because the coherence gate due to the limited coherence length of the light source (see section 1) is not incorporated explicitly. Others have suggested to use Monte Carlo simulation and the total optical path length travelled by a photon packet to determine the influence of the coherence gate [43,45,46]. While this could be a valid approach, it clear from the previous discussion of photon packets and coherence that, how intuitively correct it may seem, this may not be the case. However, no efforts have been published to establish the meaning of a photon packet in such a temporal mixing of fields, so future work is required to establish such a relation. It is the intention that the Monte Carlo model of the OCT signal presented in this thesis may be instrumental in such studies.

2.2 Analytical analysis of the OCT system

In this section, the considered system geometry is presented, and details of the analytical OCT model are described. The description of the analytical OCT model is important to the following analysis, because the intend of the new Monte Carlo model presented in this thesis is to model the same physics. In section 2.2.1, it is proven that the sample field is delta-correlated in the conjugate plane to the discontinuity reflecting the sample beam. In section 2.2.2, a new suggested way of calculating the OCT signal using the intensity distributions of the sample and reference beams is proven to be mathematically identical to the expression obtained in the analytical OCT model [48]. This essentially proves the viability of

Monte Carlo simulations in this context as discussed in section 2.1.2.

System geometry

Consider a generic OCT system as shown in Fig. 1.1 consisting of a fiber-optic Michelson interferometer with identical optics in the sample and reference arms. The sample arm focuses the light on a discontinuity within a scattering sample where a fraction of the light is reflected to be collected by the interferometer. The reference arm directs the light towards a mirror positioned such that the optical path length of the reference arm is matched to the discontinuity in the sample. Due to the short coherence length of the light source, only light from the specific discontinuity within the sample contributes to the OCT signal. The optics of the sample arm is shown in Fig. 2.1. The optical fiber end of the sample arm of the Michelson interferometer is positioned in the p-plane. The fiber emits the sample beam, which impinges on the collimating lens L1. The focusing lens L2 is positioned in the r-plane where the light distribution is a Gaussian beam with an intensity $1/e$-width, w_0. The beam is focused by L2 upon a diffusely reflecting discontinuity coinciding with the q-plane at the depth z_f inside a scattering sample a distance d from L2. The sample is taken to be a infinite slab in the transverse direction. The light reflected by the discontinuity propagates back out through the sample, through lenses L2 and L1 to the optical fiber, where it is collected by the interferometer. Throughout this thesis, the space immediately to the right of L2 is generally described by the coordinate set $(\mathbf{q}, z)$, where z is the longitudinal coordinate along the optical axis, and $\mathbf{q}$ is a transverse vector. The length of a vector $\mathbf{q}$ is generally written as q. The quantities n_0 and n_1 are refractive indices of the surroundings and sample, respectively. The lenses in L1 and L2 have a focal length f and are taken to be identical, perfect and infinite in radius. This means that the q- and p-planes are conjugate planes with a magnification of unity.

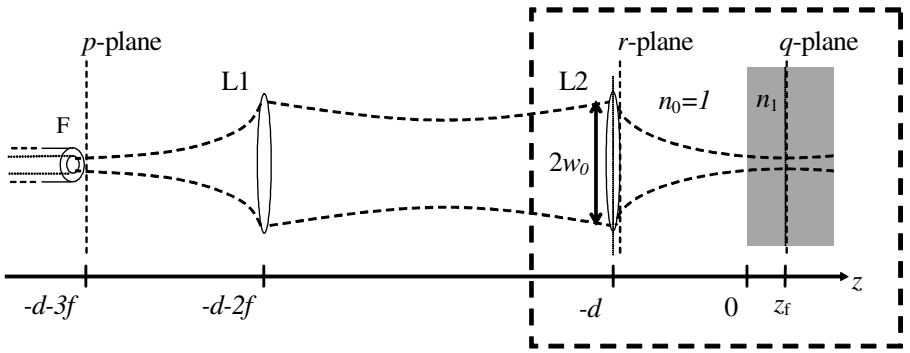

Figure 2.1: The sample arm setup of the OCT system. The lenses L1 and L2 are considered to be identical, perfect, and have infinite radius. The setup is essentially a 4F system.

analytical OCT model

As discussed in the introduction to this thesis, the OCT signal is produced by the mixing of the reference field, received from the reference mirror, and the sample field, received from the sample, on the photodetector of the OCT system. Due to the symmetry of the system one may calculate the mixing of the two fields in the r-plane, and it is therefore sufficient only to consider a propagation geometry corresponding to the section enclosed by a dashed line in Fig. 2.1 [48]. The mean square of the signal current $i\,(t)$ may be written as [47]

$$\left\langle i^2\,(t)\right\rangle = 2\alpha^2\left|g\,(\tau)\right|^2 \mathrm{Re}\left[\iint \Gamma_{\mathrm{R}}\,(\mathbf{r}_1,\mathbf{r}_2)\,\Gamma_{\mathrm{S}}\,(\mathbf{r}_1,\mathbf{r}_2)\,d^2\mathbf{r}_1 d^2\mathbf{r}_2\right] \equiv \Psi_r\left\langle i_0^2\,(t)\right\rangle \tag{2.1}$$

where $\Gamma_{\mathrm{R}}\,(\mathbf{r}_1,\mathbf{r}_2) = U_R\,(\mathbf{r}_1)\,U_R^*\,(\mathbf{r}_2)$ is the cross correlation of the scalar reference field, $\Gamma_{\mathrm{S}}\,(\mathbf{r}_1,\mathbf{r}_2) = \langle U_S\,(\mathbf{r}_1)\,U_S^*\,(\mathbf{r}_2)\rangle$ is the cross correlation of the sample field, α is a proportionality constant and $\mathbf{r}_1$ and $\mathbf{r}_2$ are vectors in the r-plane (see Fig. 2.1). Throughout this thesis it is understood that spatial integrals are to be performed over the entire plane in question. The quantity Ψ_r is the so-called heterodyne efficiency factor, which quantifies the reduction in signal due to scattering, and $i_0\,(t)$ is the OCT signal current in the absence of scattering. The mean square of the signal in the absence of

scattering, $\left\langle i_0^2(t)\right\rangle$, is relatively easily obtained [48], and the main objective of developing a Monte Carlo model is, therefore, to estimate Ψ_r. The angle brackets $\langle\rangle$ in Eq.(2.1) denotes an ensemble averaging over the statistical properties of the scattering medium and the discontinuity. The function $g(\tau)$ is the normalized temporal coherence function of the field, where τ is the time difference of propagation between the two fields when they reach the detector. It is important to note that the results of Ref. [48] limits the investigation to the paraxial regime. For OCT systems, however, the paraxial approximation is a valid assumption, since most OCT set-ups do not utilize a hard focus due to the difficulties of translating the focal region along with the position of the reference mirror [95]. In addition, most tissues are highly forward scattering in the near-infrared regime in which most OCT systems operate [96]. Due to the assumption of forward scattering, the temporal distortion of the sample field is assumed negligible relative to the coherence time of the light source and thus $g(\tau)$ is independent of $\mathbf{r}_1$ and $\mathbf{r}_2$ [94]. Because the optical path lengths of the reference and sample beams are assumed matched $g(\tau) = 1$.

It has been shown that the heterodyne efficiency factor from Eq.(2.1), may be calculated from [97]

$$\Psi_r = \frac{\int |K(\mathbf{r})|^2 \, |\Gamma_{\mathrm{PT}}(\mathbf{r})|^2 \, d^2\mathbf{r}}{\int |K(\mathbf{r})|^2 \, d^2\mathbf{r}}, \tag{2.2}$$

where $K(\mathbf{r})$ is the overlap integral of the unscattered field in the r-plane, and $\Gamma_{\mathrm{PT}}(\mathbf{r})$ the mutual coherence function is the mutual coherence function of a spherical wave in the r-plane from a point source in the q-plane [47]. These functions are defined in appendix A. Equation (2.2) is used in the following proof, and to obtain numerical results of the analytical OCT model in chapter 4.

Coherence properties

The OCT signal depends upon the lateral cross correlation of the light from the scattering sample, as indicated by Eq.(2.1). In Ref. [48] it is found that the lateral coherence length in the r-plane, ρ_0, of the sample field for a

single scattering layer in front of the discontinuity is given by

$$\rho_0 = \sqrt{\frac{3}{\mu_\mathrm{s} z_\mathrm{f}}} \frac{\lambda_\mathrm{c}}{\pi \theta_\mathrm{rms}} \left(1 + n_1 d / z_\mathrm{f}\right), \tag{2.3}$$

where $\theta_\mathrm{rms} = \arccos(g)$ is the mean scattering angle. With a non-zero lateral coherence length, ρ_0, it is given from Eq.(2.1) that the OCT signal depends upon the spatial coherence properties of the field from the sample. As discussed in section 2.1, a Monte Carlo simulation does not describe the spatial coherence properties of light and thus a direct simulation of Eq.(2.1) is not possible. However, it is noted that because it is assumed that the discontinuity is diffusely reflecting the lateral coherence will be zero immediately after reflection, i.e., delta-correlated [13, 98]. Therefore, the motivation for envisioning the system geometry, considered in Ref. [48], as part of a 4F setup is to obtain the p-plane as a conjugate plane to the q-plane (see Fig. 2.1). With the conjugate relation, the lateral coherence length of the sample field in the p-plane, $U_S(\mathbf{p})$, will also be zero in the absence of scattering. However, as it will shown in the following section, the sample field is delta-correlated in p-plane even in the presence of scattering, so that the cross correlation in this plane may be written as

$$\Gamma_\mathrm{S}(\mathbf{p}_1, \mathbf{p}_2) = \langle U_S(\mathbf{p}_1) U_S^*(\mathbf{p}_2) \rangle = \delta(\mathbf{p}_1 - \mathbf{p}_2) \langle I_\mathrm{S}(\mathbf{p}) \rangle . \tag{2.4}$$

Accordingly, if the heterodyne efficiency factor Ψ_p, and therefore also the OCT signal, may be calculated in the p-plane similarly to the calculation in the r-plane in Eq.(2.1), then

$$\begin{aligned} \Psi_p &= \frac{\langle i^2(t) \rangle}{\langle i_0^2(t) \rangle} = \frac{\mathrm{Re}\left[\iint \Gamma_\mathrm{R}(\mathbf{p}_1, \mathbf{p}_2) \Gamma_\mathrm{S}(\mathbf{p}_1, \mathbf{p}_2) \, d^2\mathbf{p}_1 d^2\mathbf{p}_2\right]}{\mathrm{Re}\left[\iint \Gamma_\mathrm{R}(\mathbf{p}_1, \mathbf{p}_2) \Gamma_{S0}(\mathbf{p}_1, \mathbf{p}_2) \, d^2\mathbf{p}_1 d^2\mathbf{p}_2\right]} \\ &= \frac{\int I_\mathrm{R}(\mathbf{p}) \langle I_\mathrm{S}(\mathbf{p}) \rangle \, d^2\mathbf{p}}{\int I_\mathrm{R}(\mathbf{p}) \langle I_{\mathrm{S},0}(\mathbf{p}) \rangle \, d^2\mathbf{p}}, \end{aligned} \tag{2.5}$$

where I_R and $I_{\mathrm{S},0}$ are the intensities of the reference beam and the sample beam in the absence of scattering, respectively.

The objective of the following analysis is thus to prove that the heterodyne efficiency factor, Ψ_p, calculated in the p-plane is mathematically

identical to the correct heterodyne efficiency factor, Ψ_r, calculated in the r-plane, so

$$\Psi_p = \frac{\int I_{\mathrm{R}}(\mathbf{p}) \langle I_{\mathrm{S}}(\mathbf{p}) \rangle \, d^2\mathbf{p}}{\int I_{\mathrm{R}}(\mathbf{p}) \langle I_{\mathrm{S},0}(\mathbf{p}) \rangle \, d^2\mathbf{p}} = \Psi_r, \tag{2.6}$$

This is the important result of this chapter that demonstrates the incoherent Monte Carlo simulation method may be applied to obtain Ψ_r and the OCT signal. It should be noted that no loss of generality has occurred in assuming a 4F setup or that the optics of the reference and sample arms are identical.

2.2.1 Delta-correlation of sample field in conjugate plane

To prove that the sample field is delta correlated in the p-plane in the presence of scattering, it must be shown that the cross-correlation of the sample field is given by

$$\Gamma_{\mathrm{S}}(\mathbf{p}_1, \mathbf{p}_2) = \langle U_S(\mathbf{p}_1) U_S^*(\mathbf{p}_2) \rangle = \delta(\mathbf{p}_1 - \mathbf{p}_2) \langle I_{\mathrm{S}}(\mathbf{p}) \rangle, \tag{2.7}$$

where $\mathbf{p}$ is a vector in the p-plane and $I_{\mathrm{S}}(\mathbf{p})$ is the intensity of the sample field, $U_S(\mathbf{p})$, which is back reflected by the diffusely reflecting discontinuity in the sample.

To outline the proof: The field $U_S(\mathbf{p})$ in the p-plane is determined by propagating a field, $U_q(\mathbf{q})$, from the reflecting discontinuity in the q-plane (refer to Fig. 2.1). This is accomplished by first calculating $U_S(\mathbf{p})$ by propagating a field from the r-plane, $U_r(\mathbf{r})$, and then finding $U_r(\mathbf{r})$ by propagating $U_q(\mathbf{q})$ from the q-plane. Noting that the field impinging on the sample is a Gaussian beam focused in the q-plane, $U_q(\mathbf{q})$ is found using a previously published result for a Gaussian beam propagating in scattering media [49] (see appendix A). Finally, the mutual coherence function is calculated. Because the final objective of the analysis is to prove Eq.(2.6) and find the ratio, Ψ_p, any multiplicative constant not related to the properties of the scattering medium are omitted in the following.

Using the Huygens-Fresnel principle [49], the sample field in the p-plane, $U_S(\mathbf{p})$, from propagating a field in the r-plane immediately to the right of

the focusing lens L2, $U_r(\mathbf{r})$, is given by

$$U_S(\mathbf{p}) = \int U_r(\mathbf{r})\, G_{r-p}(\mathbf{r},\mathbf{p})\, d^2\mathbf{r}, \tag{2.8}$$

where $G_{r-p}(\mathbf{r},\mathbf{p})$ is the Huygens-Fresnel Green's function for propagation from the r-plane to the p-plane. For a general $ABCD$ matrix system this Green's function is given by [49]

$$G_0(\mathbf{r},\mathbf{p}) = -\frac{k}{2\pi B}\exp\left[-\frac{ik}{2B}\left(Ar^2 - 2\mathbf{r}\cdot\mathbf{p} + Dp^2\right)\right] \tag{2.9}$$

where A, B, and D are the matrix elements, k is the wave number, $i=\sqrt{-1}$ and the notation r denotes the length of the vector $\mathbf{r}$. For the propagation from the r-plane to the p-plane $A=-1$, $B=f$ and $D=-1$. Using the extended Huygens-Fresnel principle [49,99], the field at the r-plane, $U_r(\mathbf{r})$, propagated from the field impinging upon the discontinuity in the q-plane, $U_q(\mathbf{q})$, is found as

$$U_r(\mathbf{r}) = \int \eta(\mathbf{q})\, U_q(\mathbf{q})\, G_f(\mathbf{q},\mathbf{r}) \exp\left[i\varphi(\mathbf{q},\mathbf{r})\right] d^2\mathbf{q} \tag{2.10}$$

where G_f is the Huygens-Fresnel Green's function for propagating the optical distance f given by Eq.(2.9) with the matrix elements $A=1$, $B=f$, and $D=1$. The function $\varphi(\mathbf{q},\mathbf{r})$ is the stochastic phase, due to the scattering medium, added to the phase of a spherical wave propagating from q-plane to r-plane, and $\eta(\mathbf{q})$ is a complex reflection coefficient of the discontinuity.

Using Eqs.(2.8)-(2.10) the cross-correlation of the field $U_S(\mathbf{p})$ is given by

$$\begin{aligned}
\Gamma_S(\mathbf{p}_1,\mathbf{p}_2) &= \langle U_S(\mathbf{p}_1)\, U_S^*(\mathbf{p}_2)\rangle \qquad (2.11)\\
&= \iiiint G_f(\mathbf{q},\mathbf{r})\, G_f^*(\mathbf{q}',\mathbf{r}')\, G_{r-p}(\mathbf{r},\mathbf{p}_1)\, G_{r-p}^*(\mathbf{r}',\mathbf{p}_2)\\
&\quad \times \left\langle U_q(\mathbf{q})\, U_q^*(\mathbf{q}')\right\rangle \langle \eta(\mathbf{q})\,\eta(\mathbf{q}')\rangle\\
&\quad \times \langle \exp\left[i\varphi(\mathbf{q},\mathbf{r}) - i\varphi(\mathbf{q}',\mathbf{r}')\right]\rangle\, d^2\mathbf{r}\, d^2\mathbf{r}'\, d^2\mathbf{q}\, d^2\mathbf{q}'
\end{aligned}$$

where primed variables are related to U_S^* , and it has been assumed that the scattering medium and the properties of the diffusely reflecting discontinuity are independent. It has also been used that the phase distortion due to forward propagation in the scattering medium may be assumed to be statistically independent of that added to the reflected field [17], so

$$\begin{aligned} & \left\langle U_q\left(\mathbf{q}\right) U_q^*\left(\mathbf{q}\acute{}\right) \exp\left[i\varphi\left(\mathbf{q},\mathbf{r}\right) - i\varphi\left(\mathbf{q}\acute{},\mathbf{r}\acute{}\right)\right]\right\rangle \\ = \; & \left\langle U_q\left(\mathbf{q}\right) U_q^*\left(\mathbf{q}\acute{}\right)\right\rangle \left\langle \exp\left[i\varphi\left(\mathbf{q},\mathbf{r}\right) - i\varphi\left(\mathbf{q}\acute{},\mathbf{r}\acute{}\right)\right]\right\rangle . \end{aligned} \tag{2.12}$$

This assumption is automatically fulfilled in a Monte Carlo simulation because, as discussed in section 2.1, a simulated photon packet experiences a continuously changing medium.

Because the discontinuity is diffusely reflecting $\langle \eta\left(\mathbf{q}\right) \eta\left(\mathbf{q}\acute{}\right)\rangle = const. \times \delta\left(\mathbf{q}-\mathbf{q}\acute{}\right)$ [47], where $\delta\left(\mathbf{q}\right)$ is the two-dimensional Dirac's delta function. Using this, Eq.(2.11) becomes

$$\begin{aligned} \Gamma_{\mathrm{S}}\left(\mathbf{p}_1,\mathbf{p}_2\right) \; = \; & \iiint G_f\left(\mathbf{q},\mathbf{r}\right) G_f^*\left(\mathbf{q}\acute{},\mathbf{r}\acute{}\right) G_{r-p}\left(\mathbf{r},\mathbf{p}_1\right) \\ & \times G_{r-p}^*\left(\mathbf{r}\acute{},\mathbf{p}_2\right) \left\langle I_q\left(\mathbf{q}\right)\right\rangle \Gamma_{\mathrm{PT}}\left(\mathbf{r}-\mathbf{r}\acute{}\right) d^2\mathbf{r} d^2\mathbf{r}\acute{} d^2\mathbf{q} \end{aligned} \tag{2.13}$$

where $\Gamma_{\mathrm{PT}}\left(\mathbf{r}-\mathbf{r}\acute{}\right) = \left\langle \exp\left[i\varphi\left(\mathbf{q},\mathbf{r}\right) - i\varphi\left(\mathbf{q},\mathbf{r}\acute{}\right)\right]\right\rangle$ is the mutual coherence function of a spherical wave in the r-plane from a point source in the q-plane [47] (see appendix A), and $I_q\left(\mathbf{q}\right)$ is the intensity of the field $U_q\left(\mathbf{q}\right)$.

The average intensity in the q-plane, $\langle I_q\left(\mathbf{q}\right)\rangle$, has previously been found for the same propagation geometry [49] (see appendix A) as

$$\left\langle I\left(\mathbf{q}\right)\right\rangle = \left(\frac{k}{2\pi B}\right)^2 \int K\left(\tilde{\boldsymbol{\rho}}\right) \exp\left(\frac{ik}{B}\tilde{\boldsymbol{\rho}}\cdot\mathbf{q}\right) \Gamma_{\mathrm{PT}}\left(\tilde{\boldsymbol{\rho}}\right) d^2\tilde{\boldsymbol{\rho}}, \tag{2.14}$$

where $\tilde{\boldsymbol{\rho}}$=$\tilde{\mathbf{r}}$-$\tilde{\mathbf{r}}\acute{}$ is difference vector of the vectors $\tilde{\mathbf{r}}$ and $\tilde{\mathbf{r}}\acute{}$ in the r-plane, and $K\left(\tilde{\boldsymbol{\rho}}\right)$ is the overlap integral of the unscattered field in the r-plane. Now, invoking sum and difference coordinates defined as

$$\mathbf{R}=\frac{1}{2}\left(\mathbf{r}+\mathbf{r}\acute{}\right) \text{ and } \boldsymbol{\rho} = \mathbf{r}-\mathbf{r}\acute{}, \tag{2.15}$$

and performing the $\mathbf{q}$-integration and the $\tilde{\boldsymbol{\rho}}$ -integration originating from

Eq.(2.14), Eq.(2.13) yields

$$\begin{aligned}\Gamma_{\mathrm{S}}(\mathbf{p}_1,\mathbf{p}_2) &= \\ &\iint \exp\left\{-\frac{ik}{2f}\left[p_2^2-p_1^2-\boldsymbol{\rho}\cdot(\mathbf{p}_1+\mathbf{p}_2)+2\mathbf{R}\cdot(\mathbf{p}_1-\mathbf{p}_2)\right]\right\} \\ &\times\left|\Gamma_{\mathrm{PT}}(\boldsymbol{\rho})\right|^2 K(-\boldsymbol{\rho})\,d^2\boldsymbol{\rho}d^2\mathbf{R}.\end{aligned} \tag{2.16}$$

Here the well known relation

$$\int \exp\left[i\mathbf{m}\cdot(\mathbf{u}+\mathbf{v})\right]d\mathbf{m}=(2\pi)^2\,\delta(\mathbf{u}+\mathbf{v}) \tag{2.17}$$

has been used. Carrying out the $\mathbf{R}$-integration then yields

$$\begin{aligned}\Gamma_{\mathrm{S}}(\mathbf{p}_1,\mathbf{p}_2) &= \delta(\mathbf{p}_1-\mathbf{p}_2) \\ &\times\int \exp\left\{-\frac{ik}{2f}\left[p_2^2-p_1^2-\boldsymbol{\rho}\cdot(\mathbf{p}_1+\mathbf{p}_2)\right]\right\} \\ &\times\left|\Gamma_{\mathrm{PT}}(\boldsymbol{\rho})\right|^2 K(-\boldsymbol{\rho})\,d^2\boldsymbol{\rho}.\end{aligned} \tag{2.18}$$

From Eq.(2.18) it is concluded that the sample field, U_S, is delta-correlated in the p-plane, thus proving Eq.(2.7).

2.2.2 Heterodyne efficiency factor

The objective of this section is to prove the identity in Eq.(2.6):

$$\Psi_p=\frac{\left\langle i^2(t)\right\rangle}{\left\langle i_0^2(t)\right\rangle}=\frac{\int I_{\mathrm{R}}(\mathbf{p})\left\langle I_{\mathrm{S}}(\mathbf{p})\right\rangle d^2\mathbf{p}}{\int I_{\mathrm{R}}(\mathbf{p})\left\langle I_{\mathrm{S},0}(\mathbf{p})\right\rangle d^2\mathbf{p}}=\Psi_r. \tag{2.19}$$

To find the intensity of the sample field $\langle I_{\mathrm{S}}(\mathbf{p})\rangle$ Eq.(2.16) is considered for the case $\mathbf{p}_1=\mathbf{p}_2=\mathbf{p}$, so

$$\Gamma_{\mathrm{S}}(\mathbf{p},\mathbf{p})=\left\langle I_{\mathrm{S}}(\mathbf{p})\right\rangle=A_{\mathrm{L2}}\int\exp\left(-\frac{ik}{f}\boldsymbol{\rho}\cdot\mathbf{p}\right)\left|\Gamma_{\mathrm{PT}}(\boldsymbol{\rho})\right|^2K(-\boldsymbol{\rho})\,d^2\boldsymbol{\rho}, \tag{2.20}$$

where A_{L2} is the area of the focusing lens L2. The implications of this finite area are discussed below. Now, to find the numerator of Eq.(2.19), it is noted that the reference beam is an unperturbed focused Gaussian beam

in the p-plane, which may be calculated using Eq.(2.14) with $\Gamma_{\mathrm{PT}}(\boldsymbol{\rho})$=1, $A = 1$ and $B = f$. Inserting this, as well as Eq.(2.20), into the numerator of Eq.(2.19), it is found that

$$\begin{aligned} \left\langle i^2(t) \right\rangle &\propto A_{\mathrm{L2}} \iint \exp\left(-\frac{ik}{f}\boldsymbol{\rho}\cdot\mathbf{p}\right) \left|\Gamma_{\mathrm{PT}}(\boldsymbol{\rho})\right|^2 \\ &\quad \times K(-\boldsymbol{\rho})\, I_{\mathrm{R}}(\mathbf{p})\, d^2\mathbf{p} \\ &= A_{\mathrm{L2}} \int \left|\Gamma_{\mathrm{PT}}(\boldsymbol{\rho})\right|^2 \left|K(\boldsymbol{\rho})\right|^2 d^2\boldsymbol{\rho}. \end{aligned} \tag{2.21}$$

To find $\langle I_{\mathrm{S},0}(\mathbf{p})\rangle$ it is noted that the mutual coherence function, $\Gamma_{\mathrm{PT}}(\boldsymbol{\rho})$, is unity in the absence of scattering, and using Eqs. (2.19) and (2.21), Ψ_p is found as

$$\Psi_p = \frac{\int \left|\Gamma_{\mathrm{PT}}(\boldsymbol{\rho})\right|^2 \left|K(\boldsymbol{\rho})\right|^2 d^2\boldsymbol{\rho}}{\int \left|K(\boldsymbol{\rho})\right|^2 d^2\boldsymbol{\rho}}. \tag{2.22}$$

Finally, noting that the $\boldsymbol{\rho}-$integration is performed over the r-plane and comparing with Eq.(2.2) it is seen that

$$\Psi_p = \Psi_r, \tag{2.23}$$

which concludes the proof of Eq.(2.6). This demonstrates that calculating Ψ_p according to Eq.(2.22) is mathematically identical to calculating the known expression for the heterodyne efficiency factor, Ψ_r, according to the analytical OCT model [48].

It is noted that there exists a mathematical ambiguity in obtaining a delta function in Eq.(2.18), and obtaining a finite area of the focusing lens in Eq.(2.20). Firstly, this area is irrelevant for the heterodyne efficiency factor and no assumption of a finite lens area is made in the derivation of Eq.(2.6) [97]. Secondly, a finite radius of the focusing lens would have yielded an Airy function in $R_A(\mathbf{p}_1 - \mathbf{p}_2)$ instead of a delta function in Eq.(2.18), where R_A is the radius of aperture. So, if the aperture is large, the sample field will be essentially delta-correlated in the p-plane; thus, with little physical difference to Eq.(2.18). It should also be noted that the identity proven in Eq.(2.22) is strictly only valid within the approximations of the extended Huygens-Fresnel principle, and thus also only within the paraxial regime. However, for sample with scattering that is not highly

forward directed, the sample field is expected to be distorted to a higher degree. Accordingly, coherence effects are expected to be of even less importance, and therefore the assumption of delta-correlation of the field from the sample in the p-plane should at least be a good first approximation.

With the proof of Eq.(2.6), it has now been proven that the heterodyne efficiency factor of the OCT system, and therefore the signal, may be calculated from the intensity distributions of the reference and sample fields in the p-plane. Accordingly, the requirement for coherence information is relaxed, rendering Monte Carlo simulation applicable.

2.3 Summary

The basic functionality of Monte Carlo simulation for modeling of light propagation in tissue-like random media were introduced and discussed. Special attention was given to the difficulty in interpreting photon packets in field related phenomena, because Monte Carlo simulation is a simulation of incoherent energy transport. The considered system geometry was introduced, and the importance of the spatial coherence for the OCT signal was identified. It was then proven that by calculating the mixing of the reference and sample beams in the conjugate plane to the discontinuity probed by the system, the OCT signal, $\langle i^2(t)\rangle$, may be calculated from the intensity distributions of the respective beams, as indicated by Eq.(2.6):

$$\Psi_p = \frac{\langle i^2(t)\rangle}{\langle i_0^2(t)\rangle} = \frac{\int I_{\mathrm{R}}(\mathbf{p})\,\langle I_{\mathrm{S}}(\mathbf{p})\rangle\, d^2\mathbf{p}}{\int I_{\mathrm{R}}(\mathbf{p})\,\langle I_{\mathrm{S},0}(\mathbf{p})\rangle\, d^2\mathbf{p}}.$$

Here $\langle i_0^2(t)\rangle$ is the signal in the absence of scattering, I_{R} is the intensity at the reference beam, and I_{S}, $I_{\mathrm{S},0}$ are the intensity of the sample beam with and without scattering, respectively. The quantity Ψ is the important heterodyne efficiency factor that quantifies the reduction in signal due to scattering, and the subscript p signifies that it is calculated in the p-plane. Because the signal in the absence of scattering, $\langle i_0^2(t)\rangle$, is relatively easily obtained, estimation of Ψ is the main focus of developing the new Monte Carlo model of the OCT signal in the following chapters. The derived

expression for Ψ proves the viability of applying Monte Carlo simulation to an OCT system, because the requirement of coherence information in calculating the heterodyne mixing resulting in the signal is relaxed. This is the first time it has been proven mathematically that Monte Carlo simulation is applicable to model a physical quantity which inherently depends on spatial coherence.

Note that the new expression for Ψ is strictly only valid within the paraxial regime. However, samples exhibiting more isotropic scattering are expected to distort the sample field to a higher degree. Accordingly, coherence in the light from the sample is expected to be of even less importance than for samples with highly forward scattering. Therefore, the assumption of delta-correlation of the sample field in the p-plane should at least be a good first approximation.

Chapter 3

Monte Carlo modeling of Gaussian beams for OCT

In this chapter, a new method of modeling focused Gaussian beams using Monte Carlo simulation will be derived and validated by comparison to an analytical model [51, 53]. The development of the method is motivated by the requirement for accurate intensity distribution to calculate the heterodyne efficiency factor using the new expression derived in chapter 2. However, the method seperate applications as a numerical phantom which is discussed and exemplified.

3.1 Introduction

In chapter 2 it was shown that the OCT signal may be calculated from the intensity distribution of the light reflected from the sample, and an expression for the heterodyne efficiency factor, Ψ, was derived. The initial beam impinging on the sample was assumed to be a focused Gaussian beam. Therefore, a suitable method of modeling the propagation of such a beam using Monte Carlo simulations must be found in order to estimate Ψ. The considered propagation geometry corresponds to the part of Fig. 2.1 inside the dashed box; shown here, for convenience, as Fig. 3.1. Due to the general nature of the considered propagation geometry, a Monte Carlo simulation method may also be a useful tool for other applications, such as

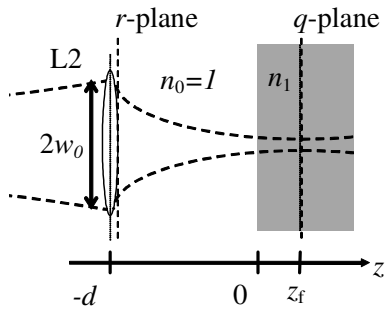

Figure 3.1: The modeled beam geometry.

laser ablation [100], requiring detailed knowledge of the intensity distribution of a focused Gaussian beam within a scattering medium.

Monte Carlo simulations have previously been applied to model the focusing of light beams in tissue. The motivations have been to study the distribution of absorbed power for photodynamic therapy (PDT) [101,102], the performance of confocal microscopy [103–105], the efficiency of 1- and 2-photon excitation microscopy [106, 107], OCT [45], and the distribution within turbid media in general [102,108,109]. In the absence of scattering, the focusing behavior of the beam is simply determined from the initial coordinates and propagation angles of the photons being launched. By carrying out Monte Carlo simulations one may then determine the distortion caused by scattering and other structures. Previously, two different ways of modeling the focusing have been employed:

1. **Geometric-focus method:** The initial position of the photon launch is found stochastically according to the initial intensity distribution and the photon packets are simply directed towards the geometric focus of the beam [45,53,102,105,108,110,111]. This method is referred to as the *geometric-focus method* in the following.

2. **Spot-focus method:** After the initial position has been found as in the geometric-focus method, the photon packets are then directed towards a random position within an area in the focal plane of the beam [103,104,106,109]. The position within the chosen spot in the

focal plane may be chosen according to different probability distributions. This method is referred to as the *spot-focus method* in the following.

To adequately model actual OCT systems, the chosen focus method must be valid for a soft as well as a hard focus. The geometric-focus method is obviously only a good approximation to a Gaussian beam for a very hard focus but even then, the infinite photon density of the unscattered photons at the geometric focus may pose a problem. Accordingly, the geometric-focus method is not suitable for the present purpose. While a suitable intensity distribution can be approximated with the spot-focus method, the drawback of this method for the present purpose lies in the stochastic nature of the photon paths. If, as discussed in section 2.1, the path lengths of the received photon packets are to be used to study the effect of scattering on the axial resolution of an OCT system, it is crucial that any stochastic spread in path lengths are caused by the interaction with the sample alone. Therefore, it is concluded that both the geometric- and spot-focus methods are unsuitable for modeling of OCT systems.

In section 3.2, a new method of launching photon packets using the hyperbolic nature of a Gaussian beam is derived. This method, in combination with Monte Carlo simulation, is in the following referred to as *the hyperboloid-method*. Furthermore, it is demonstrated that the full three-dimensional spatial intensity distribution of a Gaussian beam is obtained in free-space by launching photon packets. In section 3.3 a set of specific beam geometries and samples are selected. Intensity distributions for these propagation geometries are then obtained using the new hyperboloid method and an analytical expression [49] previously given as Eq.(2.14). This analytical model is in the following referred to as *the analytical intensity model*. The excellent agreement between the two methods are taken to validate the hyperboloid method for modeling Gaussian beam propagation in single-layered highly forward scattering samples. Finally, in section 3.4 the usefulness and performance of the hyperboloid method is demonstrated. An important result of this demonstration is that the performance is independent of choice of scattering function, which extends the method to most

realistic tissue models.

It should be noted that the derived methods in this thesis are implemented into the well known MCML computer code [66], which is then used to model the photon packet propagation through the scattering sample.

3.2 Photon packet launching algorithm

3.2.1 The hyperboloid method

Consider a Gaussian beam propagating along the z-axis from the r-plane towards the sample in the propagation geometry shown in Fig. 3.1. When the refractive indices of the sample and the surroundings are matched and no scattering occurs, the beam will be focused in the q-plane specified by $z_{\mathrm{f}} = f - d$. The $1/e$-radius, w, of the intensity as a function of z is then given by [112]

$$w^2(z) = w_{\mathrm{f}}^2 \left[1 + \frac{(z - z_{\mathrm{f}})^2}{(2z_0)^2} \right], \tag{3.1}$$

where w_{f} is the $1/e$-radius in the focal plane and z_0 is the Rayleigh range. The quantities z_0 and w_{f} are related through the relation $w_{\mathrm{f}}^2 = \lambda z_0 / (2\pi)$. It is noted that Eq.(3.1) describes a parabola in z and w with a minimum at $z = z_{\mathrm{f}}$. With $w(z) = |\mathbf{q}| = q$ as distance to the z-axis, Eq.(3.1) describes a *hyperboloid with one sheet* in ($\mathbf{q}$,z)-space immediately to the right of L2 (see Fig. 3.1). It is well known that a hyperboloid with one sheet may be constructed from one of two sets of straight lines. This is demonstrated by applying the restriction $q_y(z) = w_{\mathrm{f}}$ to Eq.(3.1) yielding:

$$q_x(z) = \pm \frac{w_{\mathrm{f}}}{2z_0} (z - z_{\mathrm{f}}), \tag{3.2}$$

where $\mathbf{q}$= (q_x, q_y). Each of these two lines may then be rotated around the z-axis to construct the hyperboloid with one sheet described by Eq.(3.1).

Now, consider a Monte Carlo photon being launched along a line belonging to the hyperboloid with one sheet given by

$$w_{\mathrm{photon}}^2(z) = C^2 w_{\mathrm{f}}^2 \left[1 + \frac{(z - z_{\mathrm{f}})^2}{(2z_0)^2} \right], \tag{3.3}$$

where C is a constant. By changing this constant, the distance, $w^2_{\text{photon}}(-d)$, from the optical axis at launch in the r-plane is controlled. It is noted that in the absence of scattering, a propagating photon will maintain its position in any transverse plane when measured relative to the intensity distribution. Hence, if a photon is launched from the r-plane with the radius from the optical axis w_0, this photon will also be in the $1/e$-intensity radius for all values of z as it propagates.

3.2.2 Launch of photon packets

When modeling the propagation geometry in Fig. 3.1, the photons are launched from the r-plane. In the MCML computer code [66] used to model the Monte Carlo photon propagation, each photon packet is initially assigned an equal amount of energy represented by a weight value, and the number of photon packets launched per area is then related to the given intensity distribution. For a Gaussian beam of with $1/e$ intensity width, w_0, the probability $\mathrm{p}(r)$ of finding a photon packet in the infinitesimal radial interval dr at radius r in the r-plane, is then given by

$$\mathrm{p}(r) = \left(\frac{2}{w_0^2}\right) \exp\left(-\frac{r^2}{w_0^2}\right) qdq \tag{3.4}$$

where the factor $2/w_0^2$ is a normalization factor. By following the method outlined by Prahl *et al.* [65] of sampling a physical quantity using a computer-generated pseudo random variable ξ evenly distributed between 0 and 1, relation between ξ and r may be obtained

$$r = w_0\sqrt{\ln(1/\xi)} = w(-d)\sqrt{\ln(1/\xi)} \tag{3.5}$$

where it has been used that the photon is launched in the r-plane for which $z = -d$ (see Fig. 3.1).

By launching photon packets at the stochastically drawn positions according to Eq.(3.5) and subsequently propagating them along a hyperboloid with one sheet given by Eq.(3.3) where $C = \sqrt{\ln(1/\xi)}$, the expected transverse intensity distribution of Gaussian beam with a $1/e$-width given by Eq.(3.1) is obtained for all values of $z > -d$. Thus, the intended full-

featured intensity distribution of a Gaussian beam is obtained in the space immediately to the right of the lens L2. Due to the cylindrical symmetry of the considered geometry, it is sufficient only to sample the variable r, saving considerable computation time. As stated earlier, the method of modeling the propagation of a Gaussian beam using the proposed launching scheme in a Monte Carlo simulation is referred to as the *hyperboloid method*.

A comparison of the three focusing models discussed above is shown in Fig. 3.2. In all three cases photons are launched from the top towards the bottom from points equidistantly positioned on a circle with centre on the optical axis. The straight lines are the photon trajectories followed in the absence of scattering. In Fig. 3.2a, the photons are launched using the geometric-focus method and the infinite photon density at the focus is observed. In Fig. 3.2b, the photons are launched using the spot-focus method, and the effect of the disordered photon trajectories may be seen in the shape and radius of the photon positions at the bottom of the box. Finally, in Fig. 3.2c, the photons are launched along a hyperboloid with one sheet producing a beam with a well-defined radius in every transverse plane including the focal plane. In order to obtain the full intensity distribution of a Gaussian beam concentric hyperboloids with different dimensions must be simulated as explained above. The transverse intensity distribution of a simulated beam propagating in free space launched from the r-plane is shown in Fig. 3.3 for $d = 0$ and $z = 0$, $z = f/2$, and $z = f$, respectively. The corresponding intensity distributions obtained by using Eq.(3.1), and the analytical expression for the intensity [112]

$$I\left(q\right) = \frac{w_0^2}{w^2\left(z\right)} \exp\left(-\frac{q^2}{w^2\left(z\right)}\right) \tag{3.6}$$

are also shown in Fig. 3.3. An excellent agreement is observed between the results obtained with the hyperboloid method and the analytical form both for the transverse and the axial distributions.

At this point, a few comments on the focusing method are relevant. The finite spot-size at the focal plane of a Gaussian beam is essentially due to the wave-nature of light, but as discussed above a Monte Carlo simulation

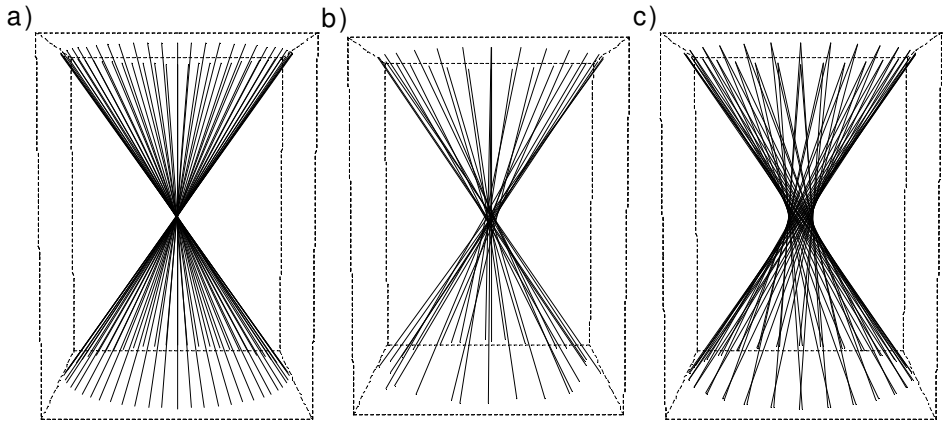

Figure 3.2: Demonstration of three methods to launch photons in a Monte Carlo simulation in order to model a focused beam. a) The photons are launched toward the geometrical focus. b) The photons are launched towards a random position within a spot in the focal plane. The size of this spot is the same as in c). c) The photons are launched along a hyperboloid with one sheet.

method of the type used here does not simulate the coherence properties of light. Instead, the result of the diffraction is being used as prior knowledge when launching the photon packets. Accordingly, one must remember that any disturbance of the light, e.g. due to scattering, is still modeled as an incoherent interaction. Furthermore, when considering the light beam as made up of a bundle of rays, the ray direction represent the directions of the energy and thus the local directions of Poynting's vector. With respect to the novel hyperboloid method, it is noted that for each point there are two possible ray directions to choose from (see Eq.(3.2)). Considering these two possibilities equally likely, the average ray direction at a certain position is given as the vectorial sum of the two line directions, and the resulting direction is equivalent to the direction of Poynting's vector for the respective Gaussian beam.

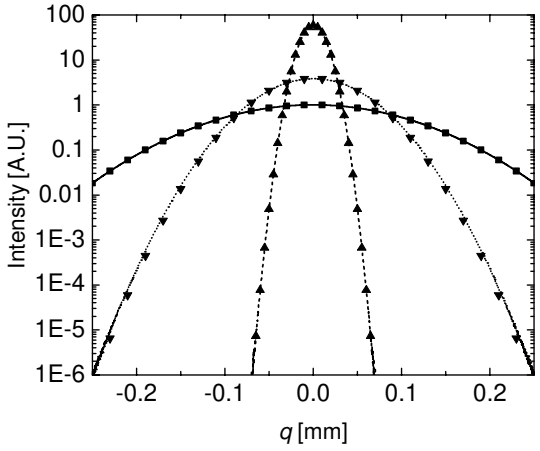

Figure 3.3: Transverse intensity distributions for a beam with $f = 16$mm, $w_0 = 0.125$mm and $d = 0$. The curves are normalized to one for (q, z)=$(0, 0)$. Symbols represent theoretical data and line plots are simulations using the hyperboloid method. ■ and solid curve: $z = 0$ (in this case coincident of the r-plane). ▼ and dotted curve: $z = f/2$. ▲ and dash-dot line: $z = f$.

3.3 Numerical validation of focusing method

3.3.1 Propagation geometries for numerical comparisons

A series of propagation geometries have been selected for numerical comparison of the analytical intensity model (Eq.(2.14)) and the hyperboloid method. These geometries are selected such that the two models are compared for different degrees of focusing and different distances between the lens L2 and the sample. The geometries are listed in Table 3.1 and are referred to as propagation geometry 1 through 5. The same geometries will be used for comparing the results of the new Monte Carlo model of the OCT signal and the analytical OCT model in the next chapter.

For all propagation geometries, the mean refractive index of the sample and the surroundings are assumed to be matched such that $n_0 = n_1 = 1$. The motivation for this choice is to avoid a distortion due to a Snell's law refraction at the interface, which will be difficult to separate from the effect of scattering. Such a distortion of the beam is not contained in the paraxial ($\sin\theta \approx \theta$) analytical intensity model based on the extended

Propagation geometry	f [mm]	d [mm]	w_0 [mm]	w_0/f
1	16.0	15.5	0.125	0.008
2	8.0	7.5	0.4	0.05
3	4.0	3.0	1.0	0.25
4	0.5	0.0	0.125	0.25
5	16.0	15.0	4.0	0.25

Table 3.1: Propagtion geometries chosen for numerical investigations

Huygens-Fresnel principle. However, as discussed in Ref. [108] this is only a severe distortion for very tightly focused beams.

In the following, the wavelength of the light is chosen to be 814nm, which is one relevant wavelength for OCT [17]. The sample is assumed to exhibit scattering described by a Gaussian scattering function given by (see e.g. chapter 13 in Ref. [61])

$$p(\theta, g) = c_{\mathrm{n}} \exp\left(-\frac{1-\cos\theta}{1-g}\right) \approx c_{\mathrm{n}} \exp\left(-\frac{\theta^2}{\theta_{\mathrm{rms}}^2}\right), \ \theta \ll 1 \tag{3.7}$$

where c_{n} is a normalization constant, $\theta_{\mathrm{rms}} = \arccos(g)$, and the approximative expression is for small angles. The motivation for this choice, is to enable comparison to an analytical model of the propagation of Gaussian beams in random media [49], which applied the Gaussian scattering function. Although not yet published [113], this model may also be applied to scattering media described by the Henyey-Greenstein scattering function [114], which is commonly employed to describe biological media. This is discussed in further detail in section 3.4.3, where a comparison between the hyperboloid method and the analytical model is made for a sample described by the Henyey-Greenstein scattering function.

Most tissues exhibit scattering with $g > 0.9$ in the near infrared, and increasing with increased wavelength [115], but examples do exist where $g < 0.9$, such as $g \approx 0.86$ for skin at 800 nm [96]. Similarly, it is noted μ_{s} is usually in the range of $5\mathrm{mm}^{-1}$ to $40\mathrm{mm}^{-1}$ depending on the density of the specific tissue, and generally decreasing with increased wavelength [96,115]. The numerical results obtained in the following are performed for various values of μ_{s} within the above range, and for two values of the asymmetry

parameter, g: Very highly forward scattering ($g = 0.99$) and highly forward scattering ($g = 0.92$). These values are chosen so comparisons can be made for a geometry where the paraxial approximation is well satisfied and for a geometry, which is somewhat closer to the limit of the paraxial approximation of $30°$($g = 0.87$). This is an interesting comparison, because the analytical intensity model [49] was derived using the paraxial extended Huygens-Fresnel principle. Accordingly, it is expected that the best agreement will be found for $g = 0.99$. However, it should be noted that the analytical OCT model (but not the analytical intensity model) has been validated by achieving excellent comparison, although with some fitting, with experimental data for $g = 0.92$ [17, 48].

3.3.2 Numerical comparison with the analytical intensity model

To investigate the performance of the proposed hyperboloid method to model a focused Gaussian beam the analytical intensity model [49] is used as a reference.

In order to validate the novel hyperboloid method, a parameter investigation is conducted for propagation geometry 1 and 2 in Table 3.1. In both of these cases, the intensity distribution are obtained in the focal plane for $g = 0.99$ and $g = 0.92$, and three different values of the scattering coefficient: $\mu_s = 5\text{mm}^{-1}$, 15mm^{-1}, and 30mm^{-1}. The results obtained for propagation geometry 1 are shown in Fig. 3.4, whereas the results for propagation geometry 2 are shown in Fig. 3.5. The results of each model have been normalized with the intensity value obtained on the optical axis for $g = 0.99$ and $\mu_s = 5\text{mm}^{-1}$, so that the parameter dependency on changes in g and μ_s of each method may be observed.

As expected, the best agreement between the analytical intensity model and the hyperboloid method is obtained when $g = 0.99$, because the case is best approximated in the paraxial approximation. The magnitude of each curve obtained using the hyperboloid method, relative to the case where $g = 0.99$ and $\mu_s = 5\text{mm}^{-1}$, follows the prediction by the analytical intensity model. As a physical curiosity, it is noted that the most confined

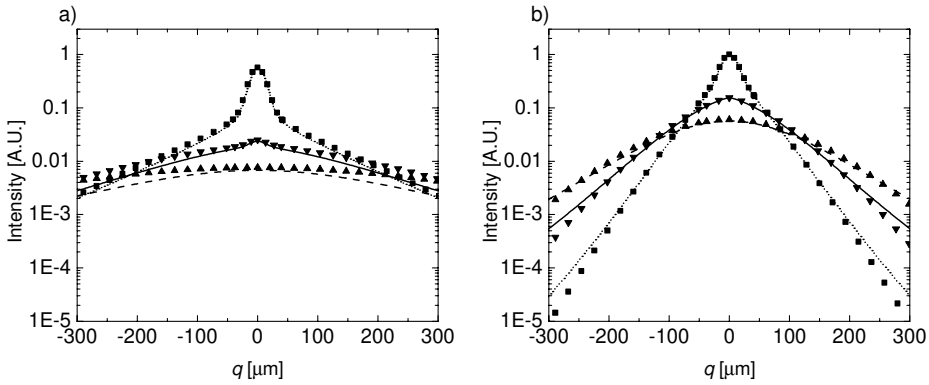

Figure 3.4: Transverse intensity distributions in the focal plane for propagation geometry 1 ($z_{\mathrm{f}} = 0.5mm$) estimated by the analytical intensity model and the hyperboloid method, respectively. a) and b) show the distributions for $g = 0.92$ and $g = 0.99$, respectively. Symbols indicate results of the analytical model whereas plots represent the results of the hyperboloid method. The distributions are normalized according to the value obtained with $(q, z, g, \mu_{\mathrm{s}})$=$(0, 0, 0.99, 5\mathrm{mm}^{-1})$. ■ and dotted line: μ_{s}=$5\mathrm{mm}^{-1}$. ▼ and solid line: μ_{s}=$15\mathrm{mm}^{-1}$. ▲ and dashed line: μ_{s}=$30\mathrm{mm}^{-1}$.

focus, as measured in the focal plane, is obtained in the case of the more isotropic scattering medium ($g = 0.92$). This is due to the fact that the scattered light in this case is being scattered further away from the optical axis than for the case with the more forward scattering medium, i.e. $g = 0.99$. From the presented curves it is seen that the deviation between the results of the two methods is increasing as a function of distance to the axis. This effect may be caused by the lack of coherence information in the scattered light in the hyperboloid method, and/or the fact that light (multiple) scattered far away from the optical axis is less well described by the paraxial approximation of the analytical intensity model. Since little spatial coherence is expected in the multiple scattered light, it is hypothesized that the latter effect is dominant. However, this can only be confirmed by experiments.

To investigate the performance of the proposed hyperboloid method for estimating the axial intensity distribution, propagation geometry 1 and 2 are simulated and compared with the analytical intensity model. Figure

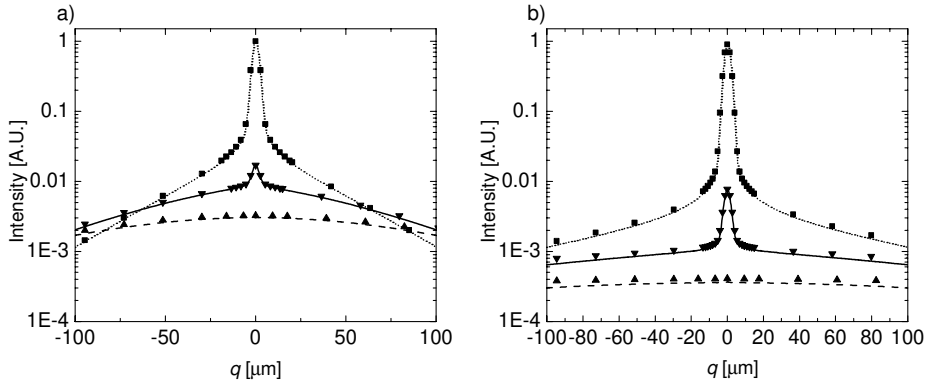

Figure 3.5: Transverse intensity distributions in the focal plane for propagation geometry 2 ($z_{\mathrm{f}} = 0.5mm$) estimated by the analytical intensity model and the hyperboloid method, respectively. a) and b) show the distributions for $g = 0.92$ and $g = 0.99$, respectively. Symbols indicate results of the analytical model whereas plots represent the results of the hyperboloid method. The distributions are normalized according to the value obtained with $(q, z, g, \mu_{\mathrm{s}})$=$(0, 0, 0.99, 5\mathrm{mm}^{-1})$. ■ and dotted line: μ_{s}=$5\mathrm{mm}^{-1}$. ▼ and solid line: μ_{s}=$15\mathrm{mm}^{-1}$. ▲ and dashed line: μ_{s}=$30\mathrm{mm}^{-1}$.

3.6a shows the intensity on axis in a sample medium with $g = 0.92$ and $\mu_{\mathrm{s}} = 15\mathrm{mm}^{-1}$ for propagation geometry 1 and 2, whereas Fig. 3.6b shows the same geometries for $g = 0.99$. Excellent overall agreement between the simulations and theory is observed.

To also investigate the performance for a more transversely confined beam a final propagation geometry is considered. Accordingly, a beam geometry with a relatively hard focus is selected (propagation geometry 3 in Table 3.1 with $z_{\mathrm{f}} = 1\mathrm{mm}$) and a sample with a scattering coefficient of $\mu_{\mathrm{s}} = 10\mathrm{mm}^{-1}$and g=0.92 is chosen so that a considerable distortion of the focus due to scattering is obtained. The beam width on the surface of the sample is $w(0) = 0.25\mathrm{mm}$, and in the absence of scattering the beam width in the focal plane is $w_{\mathrm{f}} = w(f - d) = 0.5\mu\mathrm{m}$. For such a beam, the geometric-focus method may be seen to be a good approximation. Therefore, to investigate the difference in the results obtained by using the two focusing methods, the intensity distribution is also obtained using the geometric-focus method. Figures 3.7a and 3.7b shows the axial

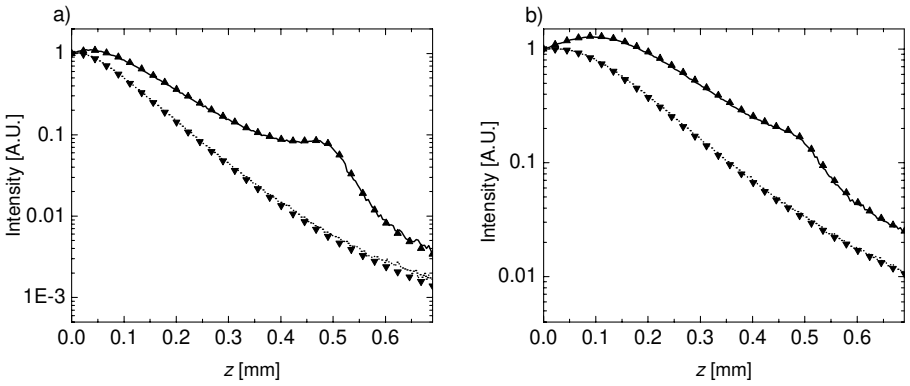

Figure 3.6: Axial intensity distribution for propagation geometry 1 and 2 with $\mu_s = 15\text{mm}^{-1}$. ▼ and dotted line is the distribution for propagation geometry 1 obtained using the analytical intensity model and the new hyperboloid method, respectively. ▲ and solid line is the distribution for geometry 2 obtained using the analytic intensity model and the hyperboloid method, respectively. a) is for $g = 0.92$ and b) is for $g = 0.99$.

distribution estimated by the geometric-focus and the hyperboloid methods, respectively. Results obtained with the analytical intensity model are also plotted as a reference (solid curve). Figures 3.7c and 3.7d show a detailed plot of the focal region of Figs. 3.7a and 3.7b, respectively. The simulation has been performed twice with the same number of photon packets (50×10^9) using each method for two sizes of discretization grid: $\Delta z = 4\mu$m, $\Delta q = 0.5$nm and $\Delta z = 2\mu$m, $\Delta q = 0.25$nm. The effect of changing grid size can be observed in Fig. 3.7c and 3.7d. The dotted curves are the results of using the larger grid size whereas the dashed curves are the results of using the smaller grid size. The solid curve in Fig. 3.7d is the result found by the analytical intensity model. The resulting intensity distributions have all been normalized to unity at $(q, z) = (0, 0)$. For the large grid size, the geometric-focus method overestimates the peak height relative to the analytical expression by a factor of 21 (dotted line, Fig. 3.7c), whereas the hyperboloid method underestimates the peak height by a factor of 0.55 (dotted line, Fig. 3.7d). It is seen that when the resolution is increased, the peak height estimated by the geometric-focus method increases even fur-

ther to a factor of 57 (dashed line, Fig. 3.7c), whereas the new hyperboloid method approaches the result of the analytical model to within a factor of 0.89 (dashed line, Fig. 3.7d). The poor result of the geometric-focus method is due to the infinite photon density of the unscattered photons in the focal plane. This demonstrates that for this method the intensity distribution will not converge as the resolution is increased. In Fig. 3.8, the transverse intensity distribution in the focal plane estimated by the geometric-focus method (dashed), the hyperboloid method (dotted) and the analytical expression (solid) are plotted, respectively. From Figs. 3.7c and 3.8, it is concluded that the geometric-focus method is an inappropriate method for estimating the detailed intensity distribution close to the focus. However, from Figs. 3.7d and 3.8 the hyperboloid method is demonstrated to perform well for a (relatively) highly focused beam.

The above results demonstrates that the novel hyperboloid method is in agreement with the analytical intensity model for a soft as well as a hard focus. Hence, the hyperboloid method for simulating focused Gaussian beams will be well suited to estimate the intensity distribution to obtain the heterodyne efficiency factor of the OCT signal given in Eq.(2.6).

3.4 Examples of the hyperboloid method as a numerical phantom

In this section, the capabilities of hyperboloid method as a numerical phantom are exemplified. As a numerical phantom, the method may be used to obtain intensity distributions difficult to obtain through experiments or investigate the performance of the analytical intensity model. This may be relevant for studies of the transverse resolution of an OCT system, but also for applications such as photodynamic therapy [101], laser ablation [100] or two-photon microscopy [116].

3.4.1 Wide-angle scattering

The extended Huygens-Fresnel principle is, strictly speaking, not valid outside the paraxial regime, which limits the considered type of scattering of

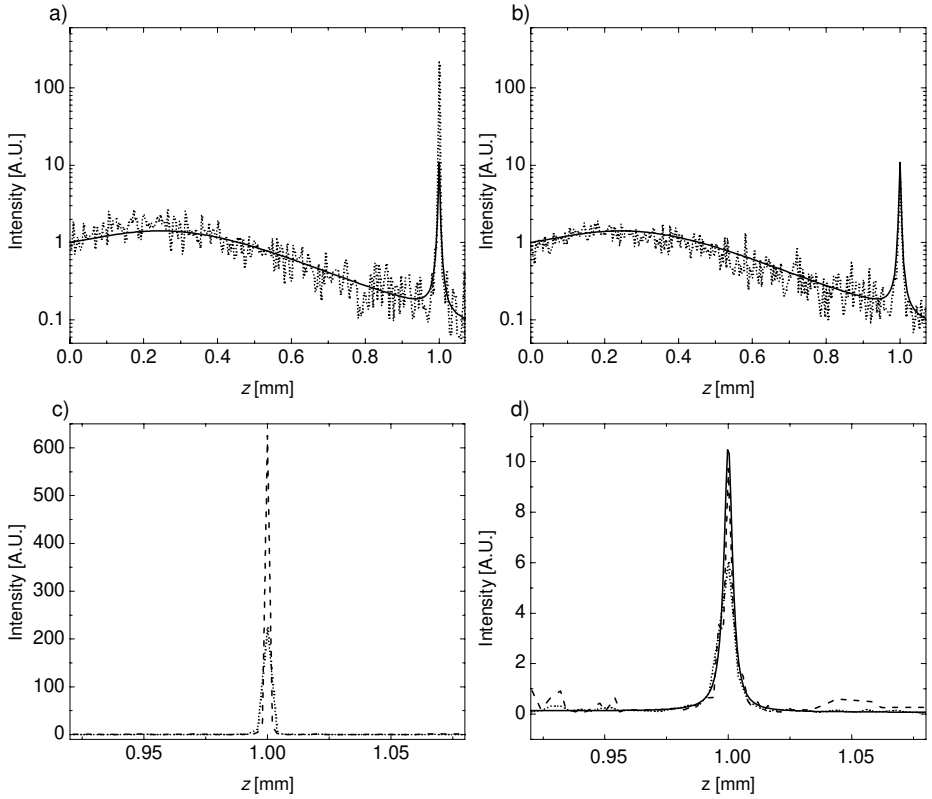

Figure 3.7: The axial intensity distribution of geometry 3 ($z_{\mathrm{f}} = 1.0$mm) in Table 3.1. Solid curves are obtained with the analytical intensity model. Dashed and dotted curves are obtained with Monte Carlo simulations with the smaller and larger grid, respectively (see text). All distributions have been normalized to unity for $(q, z) = (0, 0)$. a) and c) show results of the geometric focus method, whereas b) and d) results of the hyperboloid method.

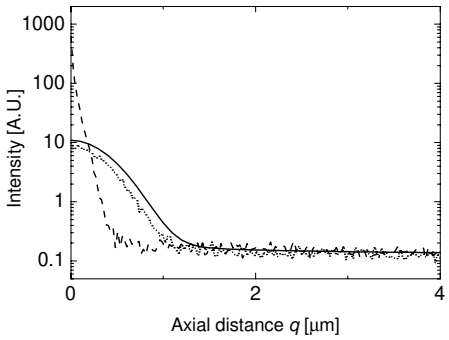

Figure 3.8: Transverse intensity distribution in the focal plane of propagtion geometry 3. Results obtained with geometric-focus method (dashed), hyperboloid method (dotted) and the analytic intensity model (solid) are shown. The Monte Carlo simulations are carried out with the small grid.

the sample to forward scattering i.e. $g \gtrsim 0.87$ [117]. However, the general Monte Carlo simulation method of modeling light-tissue interaction is not limited to paraxial scattering [63]. When moving from the near-infrared regime to shorter wavelengths most tissues exhibit scattering which is more isotropic [96, 115]. An example of an application that uses a shorter wavelength is the use of a frequency doubled Nd:YAG at 532nm focused into the skin (dermis) to treat port wine stains [118]. The asymmetry parameter of the light scattering exhibited by human dermis at 532nm is $g \approx 0.775$ [118]. It is expected that the proposed hyperboloid method is more accurate the more isotropic the scattering is, because an isotropic scattering imposes a greater distortion of the light. This implies that diffraction effects due to the scattered light, which is not included in the model, are less likely to be of any significance. Since, obtaining detailed information about the intensity distribution within the sample may be very time-consuming using a Monte Carlo approach, and it is therefore interesting to investigate whether the analytical intensity model can be used as a first approximation. For this investigation, the simulations and calculations similar to those leading to Figs. 3.4, 3.5 and 3.6 has been performed, but with $g = 0.775$ and $\lambda = 532$nm. Figures 3.9 and 3.10 show the results of these calculations. The transverse intensity graphs are performed for $\mu_s = 5\text{mm}^{-1}$, 15mm^{-1},

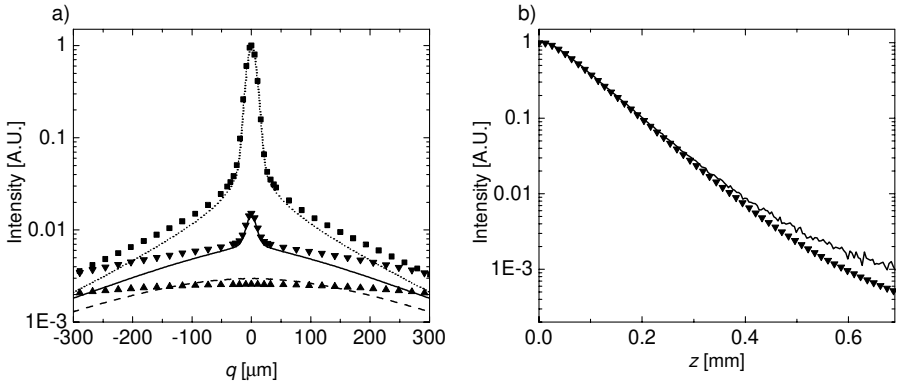

Figure 3.9: Intensity distributions for a sample with wide-angle scattering (see text) in propagation geometry 1. Symbols indicate results of the analytical model whereas plots represent the result of the hyperboloid method. The distributions are normalized according to the value obtained with (q, z, μ_s)=$(0, 0, 5\text{mm}^{-1})$. ■ and dotted line: μ_s=5mm^{-1}. ▼ and solid line μ_s=15mm^{-1}. ▲ and dashed line: μ_s=30mm^{-1}. a) Transverse intensity distributions ($z_f = 0.5mm$) with $g = 0.775$. b) Axial distribution for μ_s=15mm^{-1}.

30mm^{-1} and normalized with the intensity value at $q = 0$ and $\mu_s = 5\text{mm}^{-1}$. The longitudinal distribution is obtained for $\mu_s = 15\text{mm}^{-1}$ and normalized for $z = 0$. From Figs. 3.9 and 3.10, it is clear that, for this case, the analytical intensity model agrees well with the hyperboloid method both axially and transversely, and that the relative peak power for different values of μ_s are also well predicted. For low values of the optical depth, $\mu_s z$, this portion of the intensity distribution is dominated by the unscattered light and thus good agreement is not surprising, but even for higher values of the scattering coefficient the two models agree surprisingly well. For large values of q and z, some deviation is observed especially for propagation geometry 1. The fine overall agreement suggests that the analytical intensity model, at least as a first approximation, could be used to calculate intensity distributions outside the paraxial regime as well.

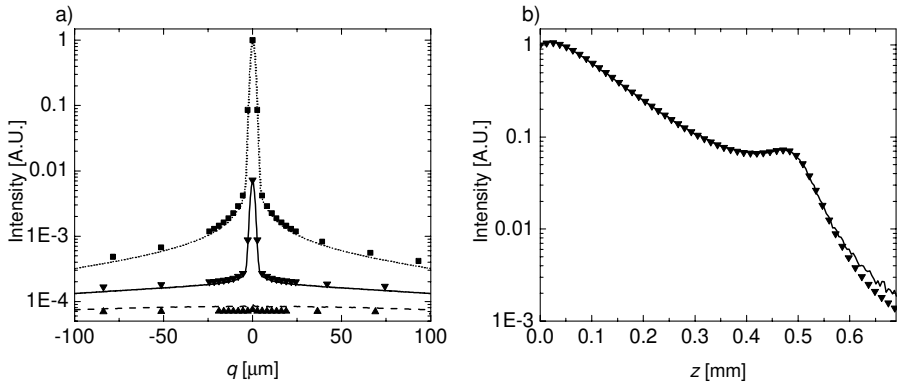

Figure 3.10: Intensity distributions for a sample with wide-angle scattering (see text) in propagation geometry 2. Symbols indicate results of the analytical model whereas plots represent the result of the hyperboloid method. The distributions are normalized according to the value obtained with (q, z, μ_s)=$(0, 0, 5\text{mm}^{-1})$. ■ and dotted line: μ_s=5mm^{-1}. ▼ and solid line μ_s=15mm^{-1}. ▲ and dashed line: μ_s=30mm^{-1}. a) Transverse intensity distributions ($z_f = 0.5mm$) with $g = 0.775$. b) Axial distribution for μ_s=15mm^{-1}.

3.4.2 Multiple layers

Through the incorporation of the *ABCD* matrix formalism in the extended Huygens-Fresnel theory [49,119] (see Eq.(A.1) in appendix A), it is straightforward to model the focusing geometry (Fig. 3.1) applied to a multi-layered sample. In order to validate such a model, laboratory experiments on multi-layered phantoms with well-controlled optical parameters and thickness of each layer is called for. Such Multi-layered structures are at best difficult to manufacture, however, simulation of such structures using Monte Carlo simulations is well established (see e.g., Refs. [66, 67, 81, 86]). With the proven performance of the present method of modeling a Gaussian beam, it is therefore interesting to compare the hyperboloid method with the analytical intensity model.

As an example, the beam specified as propagation geometry 2 in Table 3.1 is simulated. The beam is focused into a sample consisting of two layers. As in the previous examples, the refractive indices of the sample and the surroundings are matched. The first layer is 0.15mm thick and

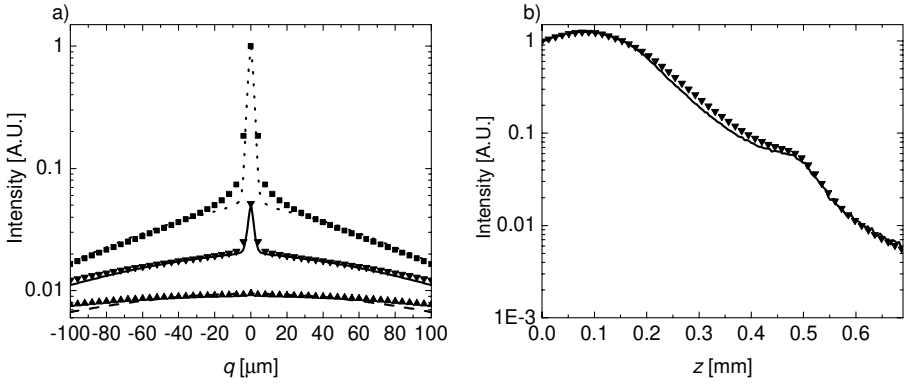

Figure 3.11: Intensity distribution in a two-layer sample (see text). Symbols indicate results of the analytical model whereas plots represent the results of the hyperboloid method. The distributions are normalized according to the value obtained with (q, z, μ_{s2})=$(0, 0, 5\text{mm}^{-1})$. ■ and dotted line: μ_{s2}=5mm^{-1}. ▼ and solid line: μ_{s2}=15mm^{-1}. ▲ and dashed line: μ_{s2}=30mm^{-1}. a) Transverse intensity distributions. b) Axial distribution for μ_{s2}=15mm^{-1}.

has a constant scattering coefficient of $\mu_{s1} = 20\text{mm}^{-1}$ and asymmetry factor $g_1 = 0.99$. The second scattering layer is taken to have infinite thickness with $g_2 = 0.92$ and a scattering coefficient μ_{s2}. In Fig. 3.11a the transverse intensity distributions in the focal plane are plotted for $\mu_{s2} = 5\text{mm}^{-1}$, 15mm^{-1} and 30mm^{-1} obtained with the analytical intensity model and the hyperboloid, respectively. Figure 3.11b shows the axial intensity distribution on the optical axis for $\mu_{s2} = 15\text{mm}^{-1}$. Excellent agreement is observed between the Monte Carlo simulations and the analytical intensity model, which corroborates that the both the analytical intensity model and the hyperboloid method are applicable to multilayered structures.

3.4.3 Choice of scattering function

For the numerical results obtained so far it has been assumed that the scattering of the sample is described by a Gaussian scattering function [61]. This choice is motivated by the fact this is the scattering function implemented in the analytical OCT model by Ref. [48]. However, it is clear that for a specific application the scattering function should be chosen in

accordance with the medium to be investigated. The Henyey-Greenstein scattering function [114] is widely accepted as a good approximation of the scattering process in most tissues [96, 120]. Accordingly, most published Monte Carlo models of light propagation in tissue applies the Henyey-Greenstein scattering function [78–88]. This is also the case for the MCML computer code [66], which is used in this thesis in a modified form to carry out the photon packet propagation. However, other scattering functions, such as the Gaussian used above, are easily implemented in this code. It has also been shown [113] that the Henyey-Greenstein scattering function may be used with the extended Huygens-Fresnel principle. The Gaussian and Henyey-Greenstein scattering functions are given by:

- Gaussian scattering function [61]:

$$p(\theta, g) = c_{\mathrm{n}} \exp\left(-\frac{1-\cos\theta}{1-g}\right) \tag{3.8}$$

- Henyey-Greenstein scattering function [114]:

$$p(\theta, g) = \frac{1-g^2}{2\left(1+g^2-2g\cos\theta\right)} \tag{3.9}$$

  The quantity c_{n} is a normalization constant.

The expressions given here follows the notation of Ref. [66], where the scattering function is written as a probability density of the deflection angle θ, so that $\int_0^{\pi} p(\theta, g) \sin\theta d\theta = 1$. Figures 3.12a and 3.12b shows a plot of the Henyey-Greenstein and the Gaussian scattering functions for three different values of g, respectively. It is noted that the Henyey-Greenstein scattering function is considerably more forward peaked ($\theta \approx 0$) than the Gaussian scattering function, but that the likelihood of a large deflection angle ($\theta > \pi/6$) is considerably larger although still relatively minute.

To demonstrate that the performance of the hyperboloid method is independent of the choice of scattering function, a beam described as propagation geometry 2 in Table 3.1, has been simulated for a sample with scattering described by the Henyey-Greenstein scattering function and $g = 0.92$, and $\mu_{\mathrm{s}} = 5\mathrm{mm}^{-1}$, $15\mathrm{mm}^{-1}$, and $30\mathrm{mm}^{-1}$, respectively. Figure 3.13a shows

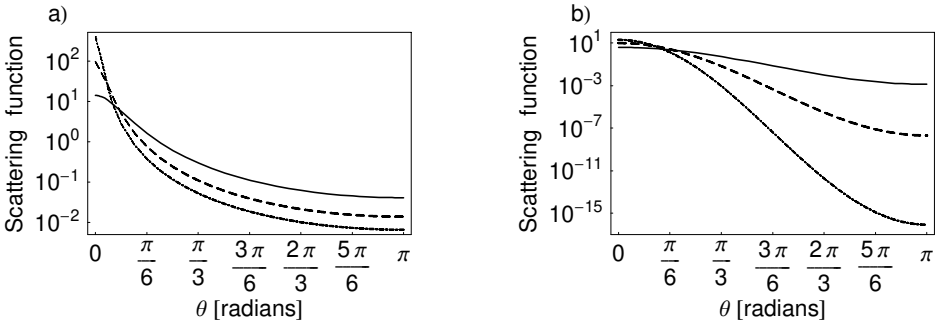

Figure 3.12: Probalilty density of the deflection angle θ as described by the Henyey-Greenstein scattering function (a) and the Gaussian scattering function (b). The asymmetry factor is $g = 0.75$ (solid), $g = 0.9$ (dash), and $g = 0.95$ (dash-dot).

the transverse intensity distribution in the focal plane for each of the simulated scattering coefficients and Fig. 3.13b shows the longitudinal on-axis intensity distribution for $\mu_s = 15\text{mm}^{-1}$. The observed excellent overall agreement (even though $g = 0.92$) is general for the other propagation geometries as well (curves not shown), and thus, the scattering function suitable for the application at hand may therefore be chosen without loss of performance.

3.5 Summary

In this chapter previously published methods of simulating focused beam using Monte Carlo simulation [45, 102–106, 108–110] were discussed and found unsuitable for modeling the sample beam of the OCT system considered in this thesis. A novel approach based on hyperboloids was derived from the analytical expression of the intensity distribution of a Gaussian beam in free-space. This method was implemented into the MCML computer code [66], and numerical results of this method were compared to a previously published analytical model [49] based on the extended Huygens-Fresnel principle [47]. Excellent agreement was obtained for a wide range of parameters relevant to tissue in the near-infrared. The use of the proposed

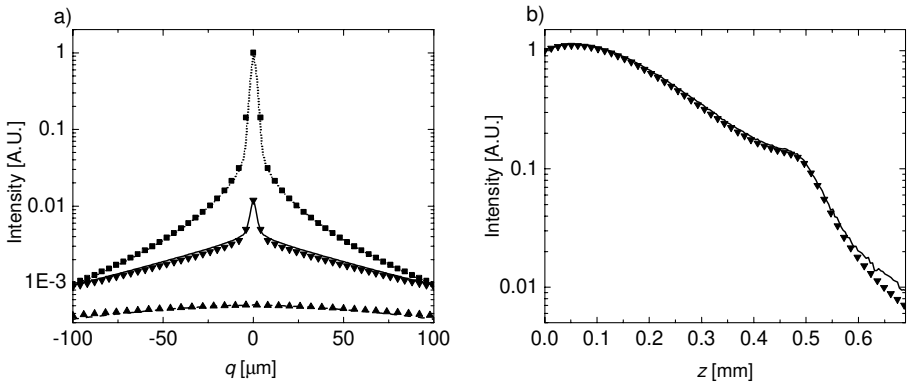

Figure 3.13: Intensity distribution in a sample described by the Henyey-Greenstein scattering function (see text). Symbols indicate results of the analytical intensity model whereas curves represent the results of the hyperboloid method. The distributions are normalized according to the value obtained with $(q, z, \mu_{s2})=(0, 0, 5\text{mm}^{-1})$: ■ and dotted: $\mu_{s2}=5\text{mm}^{-1}$. ▼ and solid line: $\mu_{s2}=15\text{mm}^{-1}$. ▲ and dashed line: $\mu_{s2}=30\text{mm}^{-1}$. a) Transverse intensity distributions for geometry 2. b) Axial distribution for $\mu_{s2}=15\text{mm}^{-1}$.

model as a numerical phantom was then illustrated through examples. As expected, excellent agreement was observed between the models when applied to modeling the propagation of a Gaussian beam through a two-layer sample. Surprisingly good agreement between the models was observed when applied to a wide-angle scattering sample. For such a sample, the paraxial approximation, and therefore also the analytical intensity model, is, strictly speaking, not valid. Finally, the good overall performance of the hyperboloid method was shown to be independent upon the choice of scattering function. This demonstrated that the hyperboloid method is not confined to samples with a specific scattering function.

With the established performance of the hyperboloid method, it is concluded that the proposed method is suitable for modeling the intensity distribution required for simulating the OCT signal according to Eq.(2.6). As an added benefit the ability of hyperboloid methods to estimate both transverse and axial confinement of a Gaussian beam may be a useful tool in applications such as photodynamic therapy [101], laser ablation [100]

or two-photon microscopy [116] where accurate intensity distributions are crucial.

Chapter 4

Monte Carlo modeling of the OCT signal

In this chapter, a new Monte Carlo model of the OCT signal [51] is derived and validated by comparison to the analytical OCT model. The performance and usefulness of the new model as a numerical phantom is then exemplified.

4.1 Introduction

In chapter 2, it was found that the heterodyne efficiency factor, and therefore also the OCT signal, may be calculated from the intensity distributions of the sample and reference beams. In the present system these beams are considered to be focused Gaussian beams, and in chapter 3 a new method of modeling the propagation of Gaussian beams through random media was derived and validated. The topic of this chapter is to combine these results to obtain a new Monte Carlo model of the heterodyne detection process in an OCT system [51]. As previously discussed, the intended purpose of the new model is that it shall function as a numerical phantom and supplement to the analytical OCT model [48]. The performance of the model as such is therefore thoroughly tested through various examples. The optical setup of the sample is, as described in section 2.2, a 4F setup as indicated in Fig. 2.1, which for convenience is repeated here as Fig. 4.1.

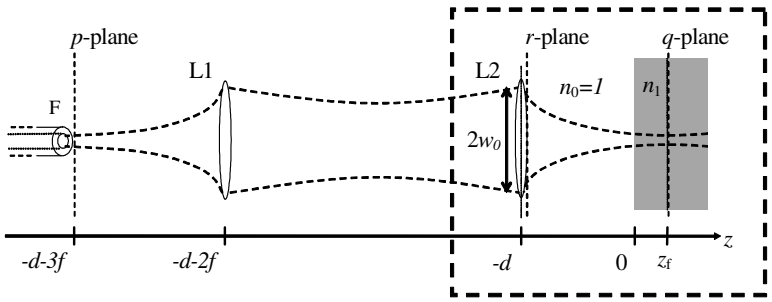

Figure 4.1: The sample arm setup of the OCT system. The lenses L1 and L2 are considered to be identical, perfect, and have infinite radius. The setup is essentially a 4F system.

Previously published attempts to model similar systems using Monte Carlo simulation have interpreted the heterodyne mixing as a rejection process in which the detected photon packets must conform to a set of criteria, on position and/or angle, in order to contribute to the signal. Here, a set of detection criteria is referred to as a *detection scheme*. Schmitt *et al.* [103] first combined geometric focusing with a detection scheme for a 4F setup to investigate confocal microscopy, and later Schmitt and Ben-Letaief [104] suggested a modification in order to reduce the simulation time. Recently, Blanca and Saloma [106] have dealt with the heterodyne detection process in the case of fluorescence confocal imaging, and Pan *et al.* [43] investigated low-coherence reflectometry using Monte Carlo simulations. They considered a collimated beam and used the path length distribution of the received photons to estimate the OCT signal according to the temporal coherence length of the light source. However, it is important to note that, as discussed in section 2.1, this method of considering the temporal coherence has not yet been thoroughly validated. The detected photons were furthermore discriminated with a criterion on the position and angle related to the numerical aperture of the receiving lens. Smithies *et al.* [45] employed a similar approach, but here the beam was focused toward the geometric focus and the Monte Carlo modelling was performed in full 3D to enable modeling of OCT imaging with oblique incidence of the focused beam. The approach to OCT modeling used by Yao and Wang [46] differed

from the previous two by using a fiber in contact with the tissue as the receiver. They used the constraint that in order for a photon to contribute to the signal, it should hit the fiber while having experienced a path length, which would fall within the coherence gate of the OCT system. Furthermore, the angle between the incoming direction and the optical axis should be less than a maximum allowable angle specified by the antenna theorem for heterodyne receivers [121].

It is important to note that the previously published detection schemes [43, 45, 46, 103, 104, 106] are all found by inspecting the optical setup, and little is discussed about the role of a single photon packet and how it should be interpreted to add to the heterodyne process. This subject was discussed in briefly section 2.1 and it will be given further consideration in section 4.3.1. Generally, one must be careful when applying angular constraints, which are derived from considerations related to field distributions, such as including an acceptance angle of a fiber mode or optical system. Such constraints may not apply to Monte Carlo photon packets, which are simple energy packets that cannot individually be said to represent a field, and, unlike real photons, are not guided by an underlying wave equation (for a discussion of this subject, see Ref. [92]).

As opposed to the previously published detection criteria, the detection scheme for the present approach is obtained from an analytical expression derived in chapter 2 (see Eq.(2.6)). This, and the description of the modeling approach, is the topic of section 4.2. In section 4.3, the new Monte Carlo model is then validated using the analytical OCT model as a reference for samples where it has previously been experimentally validated [48] . In section 4.3.1, it is demonstrated how an angular detection criterion, similar to those of the above mentioned methods, which may intuitively seem valid renders incorrect results. However, the sound foundation of the present approach, combined with the general flexibility of the Monte Carlo simulation method, renders it suitable for use as a numerical phantom and a supplement to the analytical OCT model [48]. Finally, in section 4.4, this use of the model is tested and exemplified. Here it is demonstrated, as for the hyperboloid method derived in chapter 3, that the performance of the model is independent of the choice of scattering function. This is

an important result because it extends the applicability of the modeling approach to most realistic tissue models.

4.2 Derivation of the Monte Carlo model

In section 2.2 it was found that the heterodyne efficiency factor, Ψ, of the OCT signal may be found using the only the intensity distributions of the sample and reference fields in the p-plane (see Fig. 4.1):

$$\Psi = \frac{\left\langle i^2\left(t\right)\right\rangle}{\left\langle i_0^2\left(t\right)\right\rangle} = \frac{\int I_{\mathrm{R}}\left(\mathbf{p}\right)\left\langle I_{\mathrm{S}}\left(\mathbf{p}\right)\right\rangle d^2\mathbf{p}}{\int I_{\mathrm{R}}\left(\mathbf{p}\right)\left\langle I_{\mathrm{S},0}\left(\mathbf{p}\right)\right\rangle d^2\mathbf{p}}, \tag{4.1}$$

where it is important to note that $\langle\rangle$ denotes an ensemble averaging over the scattering medium and diffusely reflecting discontinuity. Accordingly, this averaging must also be performed in the new Monte Carlo model.

As discussed in section 2.1, a simulated photon packet experiences a continuously changing medium, because the distance to the next scattering event, and resulting scattering angle, are independent of the past of the photon. Therefore an ensemble averaging over the stochastic sample in Eq.(4.1) is performed simply by simulation of many photon packets.

In order to obtain an ensemble averaging of the diffusely reflecting discontinuity, each reflected photon must experience a new realization of the discontinuity. This is obtained by considering the reflection angle as stochastic variable independent of position in the discontinuity plane. The macroscopic intensity distribution of the reflected light, I_r, is that of a Lambertian emitter [117],and hence

$$I_r\left(\theta_{\mathrm{r}}\right) = I_{\mathrm{T}}\cos\left(\theta_{\mathrm{r}}\right), \tag{4.2}$$

where I_{T} is the total reflected intensity and θ_{r} is the polar angle. Using the same method for linking a random number with a physical variable, as used in obtaining Eq.(3.5), yields

$$\theta_{\mathrm{r}} = \arcsin\left(\xi\right) \tag{4.3}$$

$$\varphi_{\mathrm{r}} = 2\pi\zeta, \tag{4.4}$$

where φ_{r} is the azimuthal angle of the reflected photon and ξ and ζ are random numbers uniformly distributed between 0 and 1.

Accordingly, the proposed method of simulating the OCT signal is performed as follows: The photon packet is launched from the focusing lens L2 in the r-plane (see Fig. 4.1) using the shape of the incident Gaussian beam, and the new hyperboloid method described in chapter 3. The interaction with specular surfaces, such as the sample surface and the propagation through the scattering medium, is performed using the MCML computer code [66]. When a photon packet is reflected off the diffusely reflecting discontinuity, Eqs.(4.3) and (4.4) are used to determine the direction of the photon after reflection. As a photon exits the sample after interaction with the discontinuity, its position and angle are used to calculate its position in the p-plane after propagation through the 4F system. To evaluate Eq.(4.1) numerically consider that the $m\acute{}$th photon packet exiting the medium, contributes to intensity at the point $\mathbf{p}_m$ in the p-plane by the amount

$$I_{\mathrm{S},m} = \frac{\mathrm{w}_m}{\Delta p^2}, \tag{4.5}$$

where the quantity w_m is the energy, or weight, carried by the photon packet and Δp^2 is a differential area around $\mathbf{p}_m$. Using this and Eq.(4.1), the Monte Carlo estimated heterodyne efficiency factor Ψ_{MC} is then given by

$$\Psi_{\mathrm{MC}} = \frac{\sum_m^M I_{\mathrm{R}}\left(p_m\right) \cdot I_{\mathrm{S},m} \cdot \Delta p^2}{\left\langle i_0^2\left(t\right)\right\rangle} = \frac{\sum_m^M I_{\mathrm{R}}\left(p_m\right) \mathrm{w}_m}{\left\langle i_0^2\left(t\right)\right\rangle} \tag{4.6}$$

where $I_{\mathrm{R}}\left(p_m\right)$ is the intensity distribution of the reference beam in the p-plane, and it is noted that the reference beam has a Gaussian intensity distribution of width w_{f} in the p-plane. The signal in the absence of scattering, $\left\langle i_0^2\left(t\right)\right\rangle$, may be either simulated or calculated. The latter is straightforward, because with the conjugate relationship between the p- and q-plane, the intensity distribution of the sample beam will be identical to that of the reference beam in the absence of scattering.

Equation (4.6) states the important detection scheme of our new method:

a photon must hit the p-plane within the extent of the reference beam to contribute to the OCT signal. It can seem counter-intuitive that photon packets contribute to the desired signal without penalty regardless of angle of incidence upon the fiber in the p-plane. However, as it will demonstrated in section 4.3.1, the inclusion of an angular criterion related to the angular extent of the reference beam, or equivalently the numerical aperture of the fiber, yields incorrect results.

4.3 Numerical validation

The heterodyne efficiency factor has been obtained with the new Monte Carlo model of the OCT signal, and calculated using the analytical OCT model [48] for several propagation geometries. These geometries, specifying the beam to the right of the focusing lens as well as the distance to the sample, are denoted as propagation geometry 1, 2, 4, and 5 in Table 3.1 (geometry 3 is not used here, due to the close resemblance to number 4 and 5). It should be noted that in the analytical OCT model, as well as in the Monte Carlo model, it is assumed that the sample beam is focused on the diffusely reflection discontinuity in the sample. In Fig. 4.2, Ψ is plotted as a function of the scattering coefficient μ_{s} and $z_{\mathrm{f}} = 0.5$mm for propagation geometry 1, 2, 4 and z_{f}=1.0mm for geometry 5. Two cases of the asymmetry parameter [90] $g = 0.99$ and $g = 0.92$ have been investigated. The motivation for choosing these two values of g is described in section 3.3.1. For reference, the case of single back-scattering at the q-plane has been included. In this case, only photons that are not scattered propagating to and from the discontinuity are assumed to contribute to the signal, i.e., $\Psi_{\mathrm{single}} = \exp(-2\mu_s z)$.

Three important observations may be made from Fig. 4.2. Firstly, fine agreement between the new Monte Carlo model and the analytical OCT model is obtained for the four tested propagation geometries. Thus, these plots are considered as validation of the new Monte Carlo model. Secondly, it is clear that the OCT signal for large optical depths is a result of multiple scattering effects, in agreement with Ref. [48]. This is seen by comparing the single scattering curve to the results of the Monte Carlo and

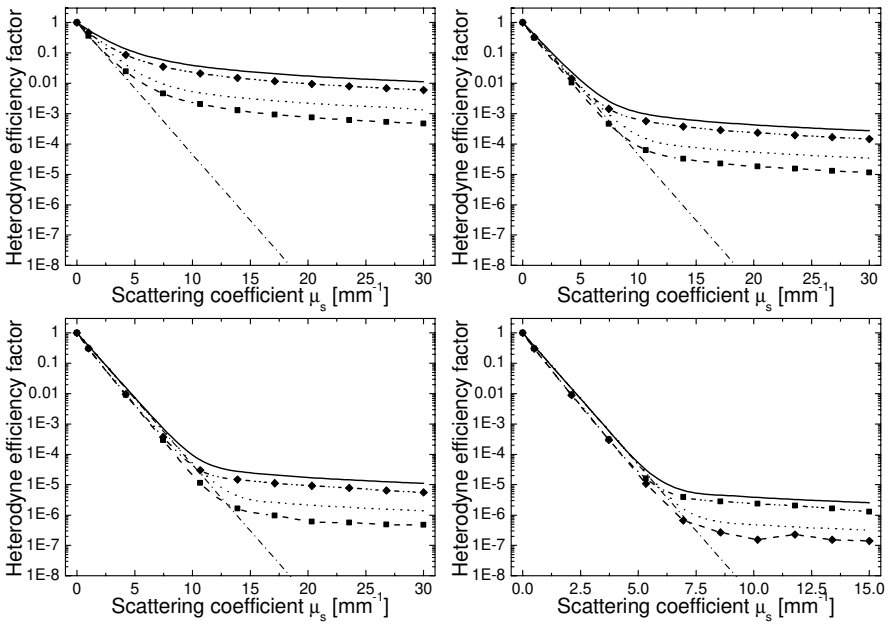

Figure 4.2: Heterodyne efficiency factors estimated using the extended Huygens-Fresnel method and the present Monte Carlo method for two cases of the anisotropy parameter g. a), b), c), and d) shows the estimated values for geometries 1,2, 4, and 5, respectively. In all cases $z_{\mathrm{f}} = 0.5$mm except for geometry 5 where $z_{\mathrm{f}} = 1.0$mm. Analytical results: $g = 0.99$ (solid) and $g = 0.92$ (dotted). Monte Carlo results: $g = 0.99$ (dash-dot and ♦) and $g = 0.92$ (dash and ■). Single scattering is showed as a thin dot-dot-dash curve.

analytical OCT model. Finally, an important result of Ref. [48] was the inclusion of the so-called shower curtain effect [47]. It is an effect caused by multiple scattering, and thus plays an important role in calculating the OCT signal as the optical depth increases. Omitting this effect leads to an underestimation of the OCT signal of several orders of magnitude [48]. Due to the fine agreement between the analytical OCT model (where the shower-curtain effect is automatically included) and the new Monte Carlo model of the OCT signal, the important result that the Monte Carlo model inherently takes this effect into account is obtained.

For cases where the approximation of the analytical OCT model is well satisfied, the observed deviation between the analytical OCT model and the Monte Carlo model is attributed to coherence effects in the intensity distribution of the sample field. Apparently, from Fig. 4.2, the lack of coherence information leads to an under-estimation of Ψ. The heterodyne efficiency factor is by definition unity in the absence of scattering. As scattering is increased deviation between the two models is expected since coherence effects due to scattered light is not described by in the propagation of the light in the Monte Carlo model. For large optical depths, $\mu_s z$, the importance of such coherence effects is expected to decrease. At the same time, the portion of multiple scattered light that is outside the paraxial regime, and thus poorly described by the analytical model, is expected to increase. To investigate the relative deviation of the two modeling methods, the ratio Ψ_{AO}/Ψ_{MC} is plotted, where Ψ_{AO} is the heterodyne efficiency factor obtained with the analytical OCT model. In order to show the deviation as a function of the effective distortion of the coherence, this ratio is plotted as a function of the transport reduced optical depth, s_{tr}, of the discontinuity given by

$$s_{tr} = \mu_s z_f (1 - g) . \tag{4.7}$$

The relative difference between the analytical OCT model and the Monte Carlo method behaves, qualitatively, identical as a function of s_{tr} independent of geometry and g. This is illustrated in Fig. 4.3 for propagation geometry 1, 2, and 4, respectively. The difference between the two approaches increases as a function of s_{tr} , but less steeply for increased scattering. This

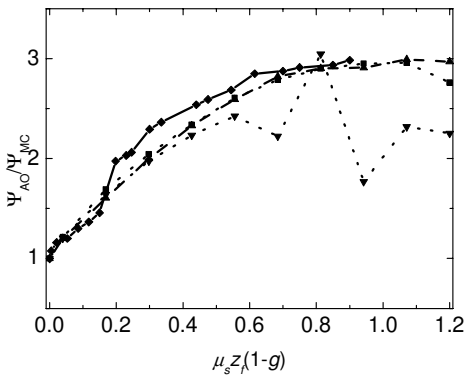

Figure 4.3: The relative difference between the results of the extended Huygens-Fresnel model and the Monte Carlo approach that were depicted in Fig. 4.2. Geometry 1 and g=0.99: The symbol ♦ and a solid curve. Geometry 1 (g=0.92): The symbol ■ and a dash-dot-dot curve. Geometry 2 (g=0.92): The symbol ▲ and a dashed curve. Geometry 4 (g=0.92): The symbol ▼ and a dotted curve.

is attributed to the lack of coherence effects in the Monte Carlo model and the paraxiality of the analytical model as discussed above. The first effect is expected to be dominant for small values of s_{tr}, whereas the latter is dominant for large values of s_{tr}. The relative importance of each effect has yet to be determined. The more abrupt behavior of the curve for geometry 4 is attributed to a higher numerical uncertainty in the case, cause by a more tightly focus beam. According to the new detection scheme, this implies that fewer photons will contribute to the signal resulting in an increased variance. This effect is also, to some degree, observed for propagation geometries 3 and 4 in Fig. 4.2.

In summary, due to the fine agreement between the results of the analytical OCT model and Monte Carlo simulations demonstrated in Figs. 4.2 and 4.3, it is concluded that the proposed novel Monte Carlo model of the OCT signal is a viable method of simulating the heterodyne efficiency factor of an OCT signal.

4.3.1 An example of an incorrect angular criterion

In sections 2.1 and 4.1 it was emphasized that caution must be taken when interpreting the role of a photon packet in phenomena that depends on coherence effects, such a heterodyne mixing. This is especially important when choosing a suitable detection scheme for a receiver system such as 4F setup studied here. In order to elaborate on this discussion, an example of an angular criterion that intuitively might seem to be in play when inspecting the optical setup is considered. This criterion is similar to criteria used in previously published methods of heterodyne detection (see section 4.1).

According to the antenna theorem [121], a field impinging on the fiber end must be incident within a certain angle to contribute to the signal through the heterodyne mixing with the reference field. This might lead one to think that the photon packets must fulfill a corresponding criterion. An equivalent criterion is that a photon must be incident within the numerical aperture of the optical fiber in order to contribute to the OCT signal. This criterion can also be realized by inserting an aperture, the size of the diameter of the reference beam, centered between the two lenses L1 and L2. Due to the Fourier transform relationship between this plane and the p-plane [122], such an aperture would serve to discriminate the ray components that represent local spatial frequency components unable to match the reference beam. In Fig. 4.4, the results of adding such a criterion to the new detection scheme introduced above is shown for propagation geometry 2 and compared to the result of the analytical OCT model. Examination of Fig. 4.4 shows that the qualitative shape of the bottom curve is similar to the correct one, but that this detection criterion estimates the signal to be more than an order of magnitude below the correct level for larger values of μ_s. This clearly demonstrates that great care must be taken when determining the detection scheme. The primary reason that the intuitive interpretation of applying such angular constraints do not hold is that the Monte Carlo simulations method only considers incoherent energy transport, and each of the above constraints are derived by tacitly assigning field properties to the individual photon packet. As an example, consider

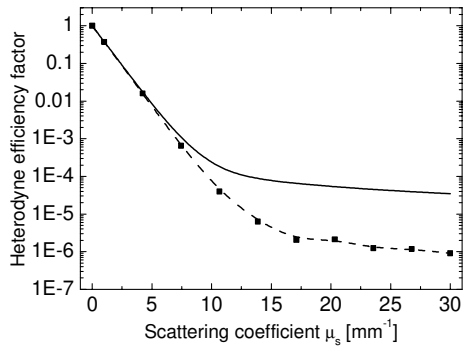

Figure 4.4: Heterodyne efficiency factors estimated by the extended Huygens-Fresnel method and a Monte Carlo method including an angular criterion for geometry 2 (z_{f}=0.5mm), respectively. The dashed curve is the results of the extended Huygens-Fresnel method whereas the symbol ■ and the solid curve are the result of the present Monte Carlo method.

again the argument of applying the antenna theorem [121] to determine whether an individual photon packet causes a heterodyne mixing with the reference field. This argument tacitly assumes that the individual photon packet is a representative of a field with a finite extend (often a plane wave), depending on the specific formulation of the theorem. However, this is inconsistent with the method of propagating the photon packets through the random medium where each scattering event is completely localized, and no underlying wave equation is guiding the propagation. This discussion if further elaborated in Ref. [92].

4.4 The new Monte Carlo model as a numerical phantom

In this section, the capabilities of the new Monte Carlo model as a numerical phantom are exemplified and discussed. With the flexibility of the Monte Carlo simulation method, the new model may be applied to model sample structures, which are cumbersome to describe analytically and/or for which one or more of the assumptions of the analytical model fail. Furthermore, it may also be applied to corroborate the applicability of the analytical OCT

model to sample structures, which are difficult to construct with suitable accuracy as phantoms in the laboratory.

4.4.1 Wide-angle scattering

As discussed in section 3.4.1, the extended Huygens-Fresnel principle is, strictly speaking, not valid outside the paraxial regime, which limits the scattering in the sample that may be described to forward scattering i.e. $g \gtrsim 0.87$ [117]. Although most tissues exhibit forward scattering in the near-infrared regime [96, 115, 123], in which most OCT systems operate, applications may exist for which this assumption is not valid. The analysis in section 2.2 was based on the extended Huygens-Fresnel principle. The analysis proved that the field reflected from the discontinuity in the sample is delta correlated in the p-plane (see Fig. 2.1 or 4.1), and this result is therefore also limited to the paraxial approximation. The delta-correlation leads to the result that the OCT signal may be calculated based on the intensities of the light from the sample and the reference. However, the field from the sample should be even less correlated for a sample with a more isotropic scattering. Accordingly, it is expected that the present Monte Carlo model of the OCT signal should perform quite well even outside the paraxial approximation. In this context it is important to note that the general Monte Carlo method of modeling light propagation is not limited to the paraxial regime [63]. Since, obtaining the OCT signal may be very time-consuming using Monte Carlo simulations, it is therefore interesting to investigate whether the analytical OCT model can be used as a first approximation for wide-angle scattering. As an example of such an investigation, the heterodyne efficiency factor has been obtained for propagation geometry 2 as in Fig. 4.2b but now with $g = 0.775$. The results are shown in Fig. 4.5 and although some deviation between the analytical OCT model and the Monte Carlo model is observed, the deviation is not significantly larger than observed in section 4.3. With the above mentioned assumption that the new Monte Carlo model of the OCT signal performs well outside the paraxial regime, this agreement could suggest that the analytical OCT model performs well, at least to a first approximation, for wide-angle

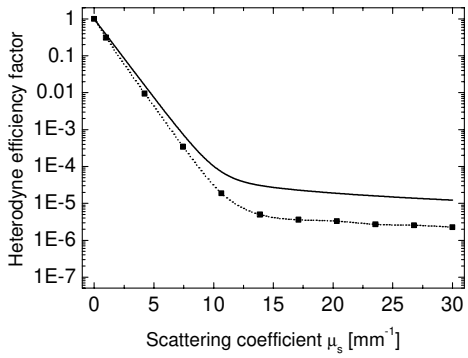

Figure 4.5: The heterodyne efficiency factor for a sample with wide-angle scattering (see text), otherwise specified by geometry 2 (z_{f}=0.5mm). The solid curve is the results of the extended Huygens-Fresnel method model whereas the symbol ■ and the dotted curve is the result of the Monte Carlo method.

scattering as well.

4.4.2 Multiple layers

It is straightforward to extend the analytical OCT model to a multi-layered samples (see appendix A of Ref. [48]). In order to validate the analytical OCT model for this case, laboratory experiments on multi-layered tissue phantoms with well-controlled optical parameters are necessary, which may be difficult to obtain. However, conventional Monte Carlo simulation of such structures is well established [66, 67, 81, 86]. This, combined with the above demonstrated performance of the new Monte Carlo model for a single layer, leads to the expectation that this model is suitable to model the OCT signal from muli-layered samples as well. It is therefore interesting to compare results of the Monte Carlo model and the analytical OCT model for this case.

As an example, consider a sample consisting of two layers. The beam and distance to the sample is specified as propagation geometry 2 in Table 3.1, and, as in the previous examples, the indices of the sample and the surroundings are matched (see section 3.3.1). The first layer of the sample is 0.15mm thick, and has a constant scattering coefficient of $\mu_{s1} = 20\mathrm{mm}^{-1}$

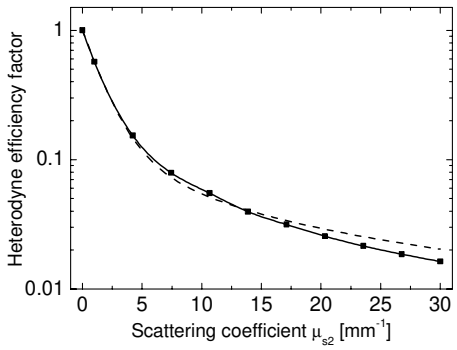

Figure 4.6: The heterodyne efficiency factor as a function of the scattering coefficient μ_{s2} of the second layer in a two-layered sample (see text). The geometry is otherwise specified by geometry 2 (z_f=0.5mm). The dashed curve is the results of the extended Huygens-Fresnel method whereas the symbol ■ and the solid curve is the result of the new Monte Carlo method.

and asymmetry factor $g_1 = 0.99$. The second layer is assumed to have infinite thickness with $g_2 = 0.92$ and a scattering coefficient μ_{s2}. In Fig. 4.6, the heterodyne efficiency factor is plotted as a function of μ_{s2}. For this example, Ψ is defined as the OCT signal relative to the OCT for $\mu_{s2} = 0$. Excellent agreement is observed between the Monte Carlo simulations and the analytical model, which corroborates that both the analytical OCT model and the novel Monte Carlo model are applicable to multilayered structures.

4.4.3 Choice of scattering function

The properties of the sample dictates the type of scattering function that must be applied in a model. In the previous sections, the modeling of OCT signals have been performed for media with a Gaussian scattering function [61]. As discussed in section 3.4.3, the Henyey-Greenstein scattering function [114] more often used as a description of the scattering process in most tissues [96, 120]. It is therefore important that the new Monte Carlo model of the OCT signal is valid for the Henyey-Greenstein scattering function. The analysis of chapter 2 is independent of the choice of scattering function, and the performance of the hyperboloid method of

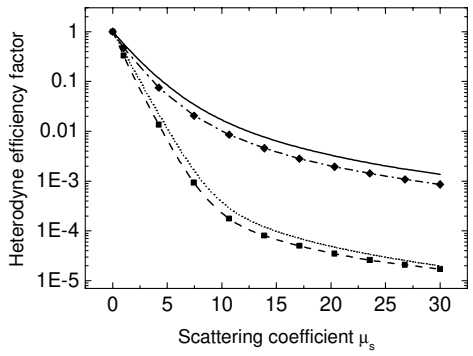

Figure 4.7: The heterodyne efficiency factor for a sample described by a Henyey-Greenstein scattering function, otherwise specified by geometry 2 (z_{f}=0.5mm). Analytical results: $g = 0.99$ (solid) and $g = 0.92$ (dotted). Monte Carlo results: $g = 0.99$ (dash-dot and ♦) and $g = 0.92$ (dash and ■).

modeling focused Gaussian beams derived in chapter 3 was also shown to be independent of the scattering function (see section 3.4.3). Accordingly, good performance of the proposed Monte Carlo model of the OCT signal is expected. To demonstrate that this is the case, the calculation and simulations performed to obtain Fig. 4.2c have been repeated with a Henyey-Greenstein scattering function. The Henyey-Greenstein scattering function is implemented into the analytical OCT model using the results of Ref. [113], and is shown in Fig. 4.7. The agreement is seen to be even better than for the Gaussian scattering function used in Fig. 4.2c. The fine agreement is also obtained between the analytical OCT model and the Monte Carlo simulations for the Henyey-Greenstein scattering function for the other geometries of Table 3.1 (curves not shown). Accordingly, it is concluded that the new Monte Carlo model also performs well for the Henyey-Greenstein scattering function. This is an important result, because it increases the versatility of the method to include most current tissue models.

4.4.4 The OCT signal as a function of depth

The numerical results for the heterodyne efficiency factor were given as a function of the scattering coefficient for constant z. For some applications it may be instrumental to plot the heterodyne efficiency factor as a function of z for constant scattering coefficient. An example of such an application is the estimation of the maximum probing depth of an OCT system with a given signal to noise ratio [17, 124]. In the chapter 6, such a curve will be used to estimate the increase in probing depth obtained by inserting an optical amplifier in an OCT system. As an example, Fig. 4.8a shows the heterodyne efficiency factor as a function of depth z in a sample with a scattering coefficient $\mu_{\mathrm{s}} = 15\mathrm{mm}^{-1}$ and an asymmetry factor of $g = 0.99$ and 0.92, respectively. The applied beam is described by propagation geometry 1 given in Table 3.1 except that the distance, d, between the lens and the sample is not constant, but given by $d = f - z$, to ensure that the beam is focused on the discontinuity. The results were estimated using both the analytical OCT model, and the new Monte Carlo model, and the relative difference is plotted in Fig. 4.8b where the maximum difference for $g = 0.92$ and $z = 1\mathrm{mm}$ is a factor 2.9. With the same arguments as for Fig. 4.3, $\Psi_{\mathrm{EHF}}/\Psi_{\mathrm{MC}}$ is expected to reach a maximum after which it decreases for increasing depth z, due to the reduced coherence of light reflected deep within in the sample. This behavior is suggested in Fig. 4.8b, where the maximum is only reached for $g = 0.92$ within the depicted range, because of the higher $s_{\mathrm{tr}}(z)$ in this case (see Eq. (4.7)). The fine comparison between the two models is taken to demonstrate the applicability of the Monte Carlo model for this application as well.

4.4.5 The absolute OCT signal

For some applications it may be desirable to obtain the absolute signal power, $\left\langle i^2(t)\right\rangle$, as opposed to the relative heterodyne efficiency factor, Ψ. The heterodyne efficiency factor was defined as (see Eq.(2.1))

$$\left\langle i^2(t)\right\rangle \equiv \Psi \left\langle i_0^2(t)\right\rangle, \tag{4.8}$$

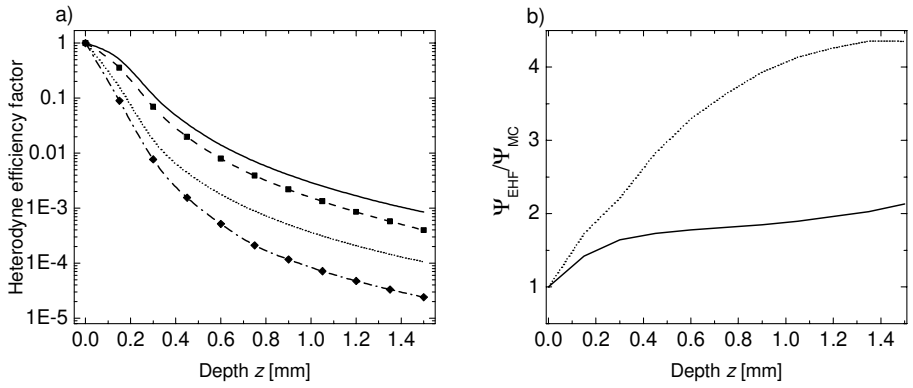

Figure 4.8: a) The heterodyne efficiency factor as a function of z for beam geometry 1, but with $d = f - z$. Analytical results: $g = 0.99$ (solid) and $g = 0.92$ (dotted). Monte Carlo results: $g = 0.99$ (dash and ■) and $g = 0.92$ (dash-dot and ♦). b) is the relative difference between the models for $g = 0.99$ (solid) and $g = 0.92$ (dotted)

where $\left\langle i_0^2(t)\right\rangle$ is the signal in absence of scattering. It may be shown [48] that the signal in the absence of scattering can be written as

$$\left\langle i_0^2(t)\right\rangle = \alpha^2 P_{\mathrm{S}} P_{\mathrm{R}} R_{\mathrm{d}} \frac{4w_0^2}{f^2} \tag{4.9}$$

where R_{d} is the reflection coefficient of the probed discontinuity, α is the responsivity of the detector, and P_{S} and P_{R} are the incident power of the sample and reference beams, respectively. Any loss of power in the transmission from the respective arms of the system to the detector can be included in P_{S} and P_{R}. From Eqs.(4.8) and (4.9) it may be seen that if the optical power from the reference power, P_{R}, and the mean square of the of the OCT signal, $\left\langle i^2(t)\right\rangle$, are known, it is straightforward to find the optical power, P_{S}, impinging on the detector of the OCT system due to the discontinuity. This property will be used in the next chapter to estimate the optical noise contribution due to the reflection from the surface of the sample.

4.5 Summary

In this chapter the results of chapter 2 and chapter 3 was used to derive a Monte Carlo model of the OCT signal. This model employs the novel hyperboloid method of modeling a focused beam (see chapter 3) and the heterodyne efficiency factor estimated using simulation is given by Eq.(4.6)

$$\Psi_{\mathrm{MC}} = \frac{\sum_{m}^{M} I_{\mathrm{R}}\left(p_m\right) \mathrm{w}_m}{\left\langle i_0^2\left(t\right)\right\rangle},$$

where $I_{\mathrm{R}}\left(p\right)$ is the intensity of the focused Gaussian reference beam in the p-plane (see Fig. 4.1), and w_m and p_m is the weight and axial distance of the m'th photon packet exiting the sample and impinging on the p-plane, respectively. Equation (4.6) reveals the important detection scheme of our new method: *a photon must hit the p-plane within the extent of the reference beam to contribute to the OCT signal*. This is the first time a detection scheme for Monte Carlo simulations has been derived analytically.

Numerical results of the model was compared to result of the analytical OCT model [48] for a single layered sample for which this model has been verified experimentally [17,48]. This was done for a wide set of parameters and excellent agreement between the two modeling methods in all cases. This demonstrated that the novel Monte Carlo model is applicable to model the OCT technique. Another important conclusion of this comparison was that the inclusion of the so-called shower-curtain effect is inherently considered in the new Monte Carlo model.

Several examples of the use of the proposed Monte Carlo model of the OCT signal as a numerical phantom were given, which demonstrated the flexibility of the model and its potential as a powerful tool in further research within the field. As expected, excellent agreement was obtained between the methods when applied to estimating the OCT signal from a two-layer sample. A surprisingly good agreement between the models was observed for the OCT signal from a wide-angle scattering sample. For such a sample the paraxial approximation, and therefore also the analytical OCT model, is, strictly speaking, not valid. Even though the derivation of the

Monte Carlo model utilized the extended Huygens-Fresnel principle, it was argued that the Monte Carlo model should perform well even for samples with wide-angle scattering. Finally, it was demonstrated that good performance of the new Monte Carlo model is independent of choice of scattering function, which is crucial since extends the applicability of the model to most realistic tissue models.

Chapter 5

Optical amplification in OCT: Theoretical analysis

In this chapter, the applicability of an optical amplifier to improve the signal-to-noise ratio (SNR) of an OCT system is analyzed theoretically, and a new model is presented [52]. An increase in SNR will enable deeper penetration depth into the sample, improve contrast, and allow faster scanning. The scope of this work is thus to identify the cases in which an optical amplifier is beneficial, and to supply design expressions with which the improvement of the SNR may be quantified and optimized for a specific system.

5.1 Introduction

As discussed in chapter 1, there are several ways to improve the signal-to-noise ratio (SNR) of an OCT system. In this chapter, the applicability of using an optical amplifier for this purpose will be investigated analytically. As with any type of amplifier, an optical amplifier amplifies the incoming power and adds noise. Since incoming noise is amplified as well as the desired signal, the SNR of the optical signal is decreased at the output of the amplifier. It is therefore clear that an optical amplifier is an advantage only when noise contributions added after the amplifier will otherwise dominate the system. In an OCT system, such noise is electrical noise added from

the, often rather involved, receiver system.

Generally speaking there are two types of optical amplifiers: Fabry-Perot amplifiers and travelling wave amplifiers. Both types use an excited medium and stimulated emission to obtain optical gain, and in that respect they are similar to light sources such as lasers, superluminescent diodes, etc. In the Fabry-Perot amplifier the end-facets of the amplifier are reflective, and therefore an effective use of the gain medium may be obtained for the resonant modes within this cavity (see e.g. Ref. [125]). In a travelling wave amplifier, the light passes the gain medium only once, enabling amplification of a broader bandwidth. Because the light source, and therefore the signal to be amplified, is broadband, the travelling wave amplifier is the preferred type for an OCT system. Since detailed amplifier analysis is outside the scope of this thesis, the results of a simple, but fully sufficient, two-level atomic model is adopted to describe the noise characteristics of an amplifier [126–128]. This amplifier model may be used for all three types of amplifiers presently relevant to OCT: Semiconductor amplifiers, doped-fiber amplifiers, and Raman fiber-amplifiers [128, 129]. Good reviews of the properties of these devices may be found in Refs. [128, 130].

With the strong demand for increased bandwidth for optical communications, research in optical amplifiers at new wavelengths and with improved characteristics is still ongoing [131, 132]. The majority of innovation has been in amplification of the 1300 nm and 1550 nm optical bands, where the fiber-loss is at its minimum. However, optical gain is obtainable in fractions of a band larger than 600 nm-1900 nm for all three amplifier types [128, 130, 133], and this band includes the wavelengths relevant to OCT. Hence, the probability that a suitable optical amplifier will be available for a specific OCT application is high, and this probability is expected to increase significantly in the near future.

The present analysis is somewhat similar to the analysis of applying an optical amplifier as a preamplifier in a coherent communication system [126,130,133]. The main difference is that in a communication system, the desired signal to be amplified is highly coherent, whereas the desired signal in an OCT system has the properties of the wide band low-coherent light source. The general conclusion of the analysis of a coherent com-

munication system is that an optical amplifier is rarely an advantage as a pre-amplifier, since shot-noise limit may, at least in theory, be obtained by increasing the power of the reference light [126, 133]. However, for OCT systems there are three reasons why this approach may not be possible: Firstly, as discussed in chapter 1, the irradiance of a suitable light source is likely to be limited to low values [23]. Secondly, the reference scanner may have a significant insertion loss further increasing the required source power. This is particularly a problem in the important class of fast scanning systems discussed in chapter 1. In the present state-of-the art fast scanning systems a Fourier-domain rapid-scan optical delay line is used [14,24,31], which has a typical insertion loss in the excess of 90% [134]. Finally, the receiver noise itself may be substantial when all components of the electrical system are included as well as any coupling of electrical noise from a clinical environment. For a fast scanning system, a suitable receiver is generally more noisy and sensitive to external noise contributions due to the necessary reduction in response time [32,130]. This is further discussed in chapter 6, where the obtainable improvement in SNR from inserting an optical amplifier is quantified for several examples of fast scanning OCT systems.

Until recently, all theoretical models considering the SNR of OCT systems were limited to considering optical shot-noise as the dominating noise contribution [15,38–40]. In January 2000 Podoleanu [32] published a comparative analysis of OCT systems with unbalanced and balanced detection, respectively. It was based on an extensive analysis of an optical low-coherence reflectometry system (OLCR) published by Takada [37], and included excess photon noise and receiver noise as significant sources of noise. Excess photon noise is caused by beating between different Fourier components of a broadband light source, and is a well known noise contribution due to spontaneous noise emission of optical amplifiers applied in communications systems [126, 127].[1]

Because of the expected importance of excess photon noise, the analyt-

[1] In the field of optical communication the terms "spontaneous-spontaneous" beat noise and "signal-spontaneous" beat noise describes the noise due to the beating of the spontaneous noise emission from an optical amplifier beating with itself and with the signal, respectively [127, 130].

ical noise model published by Takada [37] is adopted in this thesis. This model is then, as a novelty, extended to include an optical amplifier. In a realistic OCT system, detector saturation and a safety limitation on the irradiation of the sample may be important to consider when inserting an optical amplifier, and these restrictions are therefore included in this analysis. This is the first time optical power limitations have been included explicitly in OCT noise analysis which is not confined to the shot-noise limit. As an added benefit this model may also be applied to analyze conventional OCT systems confined by such limitations. For each applicable combination of these cases an design expression for the SNR is found, which may be used to optimize the system under the given constraints. The obtained SNR is then compared to the corresponding SNR for the optimized OCT system without amplification. The motivation for only considering optimized systems is that presently an optical amplifier is likely to be a relatively expensive component. A systems designer will therefore explore all options to improve the SNR by simple means, such as changing couplers, etc., before inserting an optical amplifier.

The organization of this chapter is as follows: In section 5.2 the signal-to-noise ratio of a conventional OCT system is derived in the cases of unbalanced and balanced detection, following the work of Takada [37]. In subsection 5.2.5, the assumption of shot-noise limit is given special consideration, and it will be shown that, although often inferred in the field, this assumption is only valid for special cases. In section 5.3, the two-level atomic model of an optical amplifier [126–128] is introduced into the expression for the noise of a conventional OCT system. Using this expression, it is found that the best performance from an optical amplifier is obtained when it amplifies the light from the sample in an OCT system with balanced detection, and the expression for the SNR for this configuration is then derived. This expression may serve as a design expression useful for optimizing a system. In section 5.4, an improvement factor is defined as the ratio of the SNR of an OCT system with optical amplification to the SNR of a conventional system. The improvement factor is then analyzed to determine the conditions for which an optical amplifier may improve the SNR of an optimized conventional system. This analysis

is valid for the important case of limited irradiance of the light source, so that power constraints of detector saturation and/or a safety limit on the irradiation of the sample may be ignored. Finally, in section 5.5, design expression are derived for systems with sufficient source power to impose one or both power limitations. In each case it is determined if, and for which conditions, an optical amplifier may improve the SNR.

5.2 SNR of a conventional OCT system

In this section, the different sources of noise in a conventional OCT system, i.e. in this context without optical amplification, are identified, and expressions for the SNR are derived. This analysis follows the analysis of an OLCR system by Takada [37], which was later applied to OCT systems by Poduleanu [32], and includes both balanced and unbalanced detection. Readers familiar with such analysis may review the schematics of the systems, Figs. (5.1) and (5.2), and skip to the expressions for the SNR in Eqs.(5.12) and (5.13). Systems with unbalanced as well as balanced detection is considered for two reasons: Firstly, to enable discussion of the benefits of balanced and unbalanced detection, which is essential to determining how to best insert an optical amplifier (see section 5.3 below). Secondly, to enable the discussion of the shot-noise limit, often inferred in the field, for both types of systems in section 5.2.5

The following analysis is initiated by finding the output current in each system. Then, in section 5.2.2, the structure of the sample and sample arm is described and the average signal power is derived. In section 5.2.3, the source of noise due to the broadband optical power impinging on the detector(s) are identified. In section 5.2.4 these results are combined to find expressions for the SNR for the unbalanced and balanced systems, which, combined with an amplifier model, are used in the rest of the chapter. As an added benefit, the analysis of conventional OCT systems allows for the discussion of the shot-noise limit for the two types of systems. This is the topic of Section 5.2.5, where the important conclusion is reached that the shot-noise limit is only applicable in special cases.

5.2.1 The output current of unbalanced and balanced systems

Two types of general systems are considered: an unbalanced OCT system and a balanced OCT system. In this context, balanced and unbalanced OCT system refers to OCT systems with balanced and unbalanced detection, respectively. Figure 5.1 shows an example of a unbalanced system whereas Fig. 5.2 show an example of a balanced system. In the balanced system, the split ratio $x/(1-x)$ of the first coupler from the light source has been included as a design parameter. For brevity, the quantity x is simply referred to as the split ratio. The optical circulator in Fig. 5.2 is inserted so that substantially all the reflected power from the sample is transmitted to the balanced detector. This relatively advanced system is used in this analysis such that the improvement of the SNR by inserting an optical amplifier is found relative to a state of the art system. The application of an optical circulator in OCT systems was introduced by Rollins *et al.* [36]. However, the following analysis is not limited to this specific system design. For comparison, the systems in this study are considered to have identical light sources, identical optics in the sample arm, and are probing identical samples. Subscripts u and b are used to designate quantities belonging to the unbalanced and balanced systems, respectively. The subscript p may be replaced by either u or b, and is used for quantities which are identical to the balanced and unbalanced system, respectively.

Consider the unbalanced detector shown in Fig. 5.3 with the incident fields $U_{\mathrm{sam,u}}$ and $U_{\mathrm{ref,u}}$ from the sample and reference arms, respectively. The output current from the unbalanced detector, $i_{\mathrm{u}}(t)$, is then obtained from a square-law detection [112]

$$\begin{aligned} i_{\mathrm{u}}(t) &= \eta \frac{e}{h\nu} \left| U_{\mathrm{sam,u}}(t) + U_{\mathrm{ref,u}}(t) \right|^2 \\ &= \alpha \left\{ I_{\mathrm{sam,u}}(t) + I_{\mathrm{ref,u}}(t) + 2\,\mathrm{Re}\left[U_{\mathrm{sam,u}}(t) \cdot U_{\mathrm{ref,u}}(t) \right] \right\}, \end{aligned} \tag{5.1}$$

where e is the electron charge, h Planck's constant, ν the mean optical frequency of the light source, η the quantum efficiency of the photodetectors, and $\alpha = e/h\nu$ is the responsivity of the detector [112]. The quantities

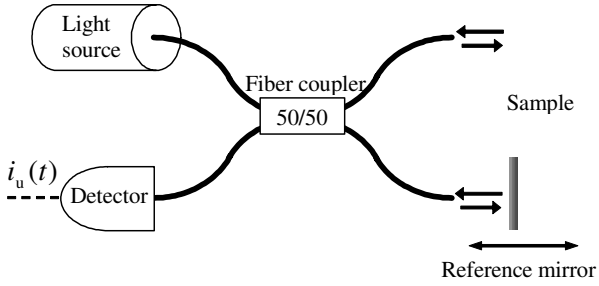

Figure 5.1: A OCT system with unbalanced detection. The light is inserted into a fiber-optic 50/50 coupler, which guides the light into the reference- and sample arms. The coupler then combines the reflected light from each arm to the detector, which returns the output current $i_u(t)$. The reference scanning system is, without loss of generality, shown as a translateable mirror.

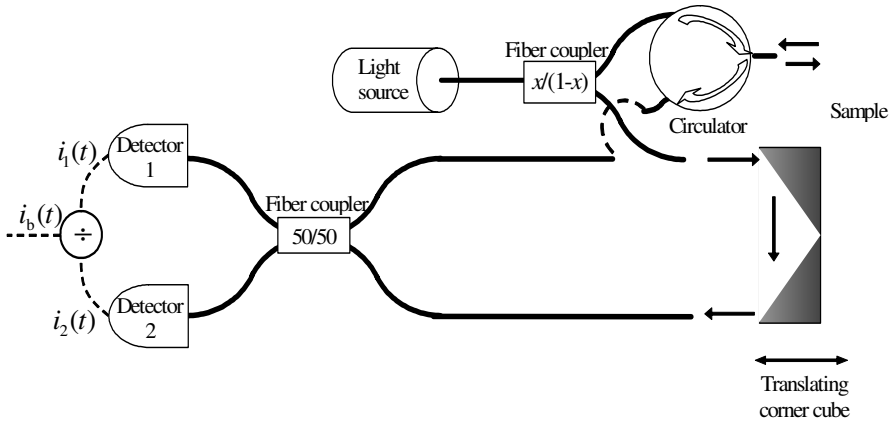

Figure 5.2: A balanced OCT system. The light from the light source is inserted into a fiber-optic coupler, with a split ratio of $x/(1-x)$, where x is a design parameter. The coupler guides the respective portions of the light to the sample- and reference arms. An optical circulator guides the light from the sample to the detector system. The light from the reference arm follows a path to the detectors different from the path of the light from the sample. In this setup this is obtained using a translatable corner cube. The balanced detector setup is described in further detail in Fig.5.4.

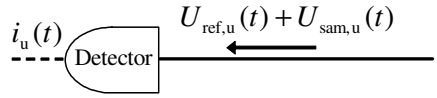

Figure 5.3: The detector of the system in Fig.5.1 with the incoming fields $U_{\mathrm{sam,u}}$ and $U_{\mathrm{ref,u}}$ from the sample- and reference arms, respectively.

$I_{\mathrm{sam,u}} = |U_{\mathrm{sam,u}}|^2$ and $I_{\mathrm{ref,u}}(t) = |U_{\mathrm{ref,u}}|^2$ are the intensities of the fields $U_{\mathrm{sam,u}}$ and $U_{\mathrm{ref,u}}$, respectively.

Similarly, consider the balanced detector shown in Fig. 5.4, with the incident fields $U_{\mathrm{sam,b}}$ and $U_{\mathrm{ref,b}}$ from the sample and reference arm, respectively. Assuming that the coupler used in the balanced detector is symmetric, the field $U_1(t)$ and $U_2(t)$ incident on detector 1 and detector 2, respectively, can be written as [136, 137]

$$\begin{bmatrix} U_1(t) \\ U_2(t) \end{bmatrix} = \begin{bmatrix} a & be^{i\varphi} \\ be^{i\varphi} & a \end{bmatrix} \begin{bmatrix} U_{\mathrm{sam,b}} \\ U_{\mathrm{ref,b}} \end{bmatrix}, \tag{5.2}$$

where φ expresses a phase change due to the coupler, a and b are coupling constants, and any common phase change to the two arms have, without loss of generality, been ignored. If the coupler is assumed lossless, this constraint will mean that $a^2 + b^2 = 1$ and $\varphi = \pm\pi/2$ [136, 137]. For the 50/50 coupler used in a balanced detector, $a = b = 1/\sqrt{2}$. Thus, for the balanced detector, the incident fields becomes

$$\begin{bmatrix} U_1(t) \\ U_2(t) \end{bmatrix} = 1/\sqrt{2} \begin{bmatrix} 1 & e^{i\pi/2} \\ e^{i\pi/2} & 1 \end{bmatrix} \begin{bmatrix} U_{\mathrm{sam,b}} \\ U_{\mathrm{ref,b}} \end{bmatrix}. \tag{5.3}$$

Using this, the photocurrents $i_1(t)$ and $i_2(t)$ from each of the respective detectors, due to a square law detection of the incident light power, is calculated as

$$\begin{aligned} \begin{bmatrix} i_1(t) \\ i_2(t) \end{bmatrix} &= \frac{1}{2}\alpha \begin{bmatrix} I_{\mathrm{sam,b}}(t) + I_{\mathrm{ref,b}}(t) \\ I_{\mathrm{sam,b}}(t) + I_{\mathrm{ref,b}}(t) \end{bmatrix} \\ &\quad + \frac{1}{2}\alpha \begin{bmatrix} e^{-i\pi/2} U_{\mathrm{sam,b}} U^*_{\mathrm{ref,b}} + e^{i\pi/2} U^*_{\mathrm{sam,b}} U_{\mathrm{ref,b}} \\ e^{i\pi/2} U_{\mathrm{sam,b}} U^*_{\mathrm{ref,b}} + e^{-i\pi/2} U^*_{\mathrm{sam,b}} U_{\mathrm{ref,b}} \end{bmatrix}, \end{aligned} \tag{5.4}$$

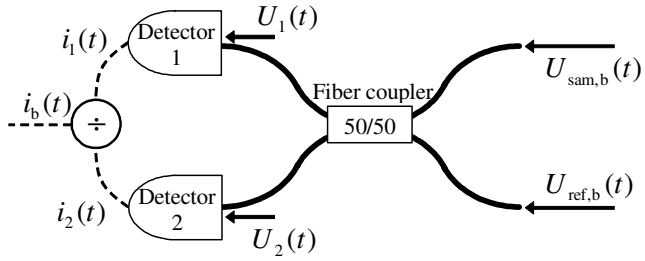

Figure 5.4: A balanced detector setup, which consist of a 50/50 coupler, two photodetectors and electronics to obtain the difference between the photocurrents $i_1(t)$ and $i_2(t)$ from the detectors 1 and 2 respectively. The fields $U_{\mathrm{sam,b}}$ and $U_{\mathrm{ref,b}}$ from the sample- and reference arms are incident on each arm of the detector system. The coupler combines the fields, and splits the power of the combination into U_1 and U_2 incident on the respective detector. Due to the phase change of π introduced by the coupler (see text) the resulting output current $i_{\mathrm{b}}(t)$ is proportional to the beat term between $U_{\mathrm{sam,b}}$ and $U_{\mathrm{ref,b}}$ alone.

where * is the complex conjugate. The electrical circuit of the balanced detector setup returns the output current of the balanced detector, $i_{\mathrm{b}}(t)$, by subtracting the photocurrents of the two detectors, such that

$$i_{\mathrm{b}}(t) = i_1(t) - i_2(t) = 2\alpha \,\mathrm{Re}\left[e^{i\pi/2} U^*_{\mathrm{sam,b}} U_{\mathrm{ref,b}}\right] = -2\alpha \,\mathrm{Im}\left[U^*_{\mathrm{sam,b}} U_{\mathrm{ref,b}}\right]. \tag{5.5}$$

Comparing Eq.(5.5) to Eq.(5.1) the advantage of the balanced receiver is clear: The balanced receiver discriminates the intensity terms which may be significant sources of noise (see section 5.2.3 below).

5.2.2 Sample structure and signal power

Generally, the field from the sample arm of an OCT system will consist of a sum of fields from different reflection sites within the sample, plus reflections from the delivery optics, such as fiber collimators and lenses. Now, consider the reflected field from the sample arm to consist of a sum of fields, such that

$$U_{\mathrm{sam,p}} = \sqrt{T_{\mathrm{p}}} \left(U_{\mathrm{coh}} + \sum_n U_{\mathrm{incoh},n} \right), \tag{5.6}$$

where p may be either u or b, and it has been used that the balanced and unbalanced systems probes identical samples and have identical optics in the sample arm. The coefficients T_{u} and T_{b} are coefficients for transmitting the field from the sample arm to the detector in the unbalanced and balanced system, respectively. For the systems shown in Fig. 5.1 and Fig. 5.2, $T_{\mathrm{u}} = 1/2$ and $T_{\mathrm{b}} = 1$, respectively. The field U_{coh} is the reflected field from the sample, which has an optical path length matched with the reference field and therefore contributes to the OCT signal. The term $\sum_n U_{\mathrm{incoh},n}$ is the sum of fields that have path length differences relative to the reference that are longer than the coherence length of the light source. These fields may therefore be taken to be incoherent with respect to the reference field. The OCT signal for each of the systems is the photocurrent due to the mixing between U_{coh} and U_{ref}, which is the only component that varies as the reference is scanned. Using Eqs. (5.1), (5.5), (5.6), and following the notation and derivation of the mean square of the signal power by Takada [37], the output current of the OCT signal is first given by

$$i_{\mathrm{p}}(t) = 2\sqrt{\langle I_{\mathrm{ref,p}}\rangle T_{\mathrm{p}} \langle I_{\mathrm{coh}}\rangle}\cos\left(2\pi f_{\mathrm{c}} t + \theta_{\mathrm{p}}\right), \tag{5.7}$$

where θ_{p} is a phase constant, f_{c} is the Doppler frequency due to the scanning of the reference, $\langle I_{\mathrm{coh}}\rangle = \left\langle |U_{\mathrm{coh}}|^2 \right\rangle$, and the brackets denotes an ensemble average. Here it is assumed that the optical path lengths of the interferometer are matched to the reflection U_{coh}. The corresponding mean square signal current is then given by [37]

$$\left\langle i_{\mathrm{p}}^2 \right\rangle = 2\alpha^2 T_{\mathrm{p}} \langle I_{\mathrm{ref,p}}\rangle \langle I_{\mathrm{coh}}\rangle . \tag{5.8}$$

Here any reduction in signal due to polarization mismatch between the reference and sample beams is neglected.

5.2.3 Sources of optical noise

To simplify the following, the reasonable assumption is made that the received intensity from the sample is dominated by the fields incoherent with respect to the reference, such that $I_{\mathrm{sam,p}}(t) \approx T_{\mathrm{p}} \left|\sum U_{\mathrm{incoh},n}\right|^2$. It has previ-

ously been shown that the current noise spectral density for a low-coherence interferometer, due to the received light, $\left\langle \Delta i^2_{\mathrm{opt,u}} \right\rangle$ for the unbalanced system is given by [37]

$$\left\langle \Delta i^2_{\mathrm{opt,u}} \right\rangle = 2e\alpha \left(\langle I_{\mathrm{ref,u}} \rangle + \langle I_{\mathrm{sam,u}} \rangle \right) + \frac{\alpha^2}{\delta\nu} \left(\langle I_{\mathrm{ref,u}} \rangle + \langle I_{\mathrm{sam,u}} \rangle \right)^2 , \qquad (5.9)$$

where $\delta\nu$ is the effective line width of the light source, and it is assumed that the light is completely unpolarized, which is most commonly the case in OCT [2]. The terms $2e\alpha \left(\langle I_{\mathrm{ref,p}} \rangle + \langle I_{\mathrm{sam,p}} \rangle \right)$ represents the shot noise, and the terms $\frac{\alpha^2}{\delta\nu} \left(\langle I_{\mathrm{ref,u}} \rangle + \langle I_{\mathrm{sam,u}} \rangle \right)^2$ represents the excess photon noise. The excess photon noise comprises of the intensity noise defined as $\frac{\alpha^2}{\delta\nu} \left(\langle I_{\mathrm{ref,u}} \rangle^2 + \langle I_{\mathrm{sam,u}} \rangle^2 \right)$ and the beat noise given by $2\frac{\alpha^2}{\delta\nu} \langle I_{m,\mathrm{u}} \rangle \langle I_{\mathrm{sam,u}} \rangle$ [37], and is caused by mixing of the different Fourier components of the spectrum of the light source. In the balanced system, the intensity noise is suppressed , so the current noise spectral density due to the light in this system is given by [37]

$$\left\langle \Delta i^2_{\mathrm{opt,b}} \right\rangle = 2e\alpha \left(\langle I_{\mathrm{ref,b}} \rangle + \langle I_{\mathrm{sam,b}} \rangle \right) + 2\frac{\alpha^2}{\delta\nu} \langle I_{\mathrm{ref,b}} \rangle \langle I_{\mathrm{sam,b}} \rangle . \qquad (5.10)$$

It should be noted that these expressions for the excess photon noise were derived assuming a broadband light source [37], and are therefore not applicable to a system where the light source is a narrow band laser.

5.2.4 Signal-to-noise ratio

To find the SNR of the systems, all relevant source of noise must be included. Besides the optical sources of noise found in the previous section, an OCT system is also subject to a noise contribution from the electrical receiver system. The importance of electrical noise contributions were justified in the introduction of this chapter and will be given more consideration in section 6.1.1. Here, it will suffice to note that since there are several other contributions to the receiver noise than the noise from the individual detector stage, the receiver noise in a balanced system is not necessarily twice that of an unbalanced system. To simplify notation, the sum of electrical noise sources are simple written as $\left\langle \Delta i^2_{\mathrm{rec,u}} \right\rangle$ and $\left\langle \Delta i^2_{\mathrm{rec,b}} \right\rangle$

for the unbalanced and balanced systems, respectively. The total current noise spectral density of each system, $\langle \Delta i_{\mathrm{p}}^2 \rangle$, is then given by

$$\langle \Delta i_{\mathrm{p}}^2 \rangle = \langle \Delta i_{\mathrm{opt,p}}^2 \rangle + \langle \Delta i_{\mathrm{rec,p}}^2 \rangle . \tag{5.11}$$

Using the signal power given by Eqs.(5.8), and the current noise spectral density given by Eqs.(5.9), (5.10) and (5.11) the SNR of the system is now obtained as:

Unbalanced system:

$$\begin{aligned} \mathrm{SNR_u} &= \frac{\langle i_s^2 \rangle}{B_{\mathrm{e}} \langle \Delta i_{\mathrm{u}}^2 \rangle} \\ &= \frac{\alpha^2}{B_{\mathrm{e}}} T_{\mathrm{u}} \langle I_{\mathrm{ref,u}} \rangle \langle I_{\mathrm{coh}} \rangle / \left[e\alpha \left(\langle I_{\mathrm{ref,u}} \rangle + \langle I_{\mathrm{sam,u}} \rangle \right) \right. \\ &\quad \left. + \frac{\alpha^2}{2\delta\nu} \left(\langle I_{\mathrm{ref,u}} \rangle + \langle I_{\mathrm{sam,u}} \rangle \right)^2 + \langle \Delta i_{\mathrm{rec,u}}^2 \rangle / 2 \right] \end{aligned} \tag{5.12}$$

Balanced system:

$$\mathrm{SNR_b} = \frac{\alpha^2 T_{\mathrm{b}} \langle I_{\mathrm{ref,b}} \rangle \langle I_{\mathrm{coh}} \rangle}{B_{\mathrm{e}} \left[e\alpha \left(\langle I_{\mathrm{ref,b}} \rangle + \langle I_{\mathrm{sam,b}} \rangle \right) + \frac{\alpha^2}{\delta\nu} \langle I_{\mathrm{ref,b}} \rangle \langle I_{\mathrm{sam,b}} \rangle + \left\langle \Delta i_{\mathrm{rec,b}}^2 \right\rangle / 2 \right]}, \tag{5.13}$$

where B_{e} is the electrical bandwidth of the receiver system.

To summarize the notation, $\langle I_{\mathrm{ref,u}} \rangle$, $\langle I_{\mathrm{sam,u}} \rangle$, and $T_{\mathrm{u}} \cdot \langle I_{\mathrm{coh}} \rangle$ are the intensities impinging on the detector system from the reference arm, sample arm, and the probed discontinuity in the unbalanced system, respectively. Similarly for $\langle I_{\mathrm{ref,b}} \rangle$, $\langle I_{\mathrm{sam,b}} \rangle$, and $T_{\mathrm{b}} \cdot \langle I_{\mathrm{coh}} \rangle$ in the balanced system. The quantities T_{u} and T_{b} are transmission coefficients that describes any reduction in $\langle I_{\mathrm{coh}} \rangle$ due to transmission from the sample arm to the detector system. The quantity $\delta\nu$ is the effective line width of the light source, e the electron charge, α the responsivity of the detector(s), and $\left\langle \Delta i_{\mathrm{rec,b}}^2 \right\rangle$ the current noise spectral density due to electrical noise in the receiver system.

Equations (5.12) and (5.13) are used in the following to determine the optimum usage of an optical amplifier, and as a reference for the obtained increase in performance. For this use it is instrumental to compare the

two types of systems. From Eqs.(5.12) and (5.13) it can be seen that for identical receiver noise, $T_{\mathrm{u}} = T_{\mathrm{b}}$, and identical power from the reference, the balanced system will always yield a better SNR, because the setup eliminates the intensity noise without reducing the signal power. However, if the noise is dominated by either the receiver noise or shot noise, the advantage of a balanced system may be minute, or even lost due to the added complexity of the system. As stated earlier, an extensive performance comparison of balanced versus unbalanced detection for a wide set of system parameters may be found in Ref. [32]. In this paper, the added complexity of attenuating the reference in the unbalanced system, as suggested by Ref. [34], was considered. A conclusion of the work was that using an unbalanced system with suitable attenuation of the reference light does not improve the performance compared to that of the balanced system, unless conservation of optical power and/or receiver noise is better. Based on Ref. [32] and the above derivation it may be concluded that if the SNR of a balanced system is improved by inserting an optical amplifier, this improvement can generally not be obtained by using an unbalanced system instead.

5.2.5 The shot noise limit

In section 5.1 it was stated that the shot-noise limit is often assumed in the analysis of OCT systems. It is therefore interesting to investigate in what cases this assumption is valid.

Firstly, it is clear that in a shot-noise limited system, receiver noise is negligible, which may be difficult to obtain. Secondly, for most practical OCT systems, the power of the reference dominates the optical power to the detector, so that $\langle I_{\mathrm{ref,p}} \rangle \gg \langle I_{\mathrm{sam,p}} \rangle$. Applying these two assumptions to Eqs.(5.12) and (5.13), it is seen that shot noise is dominant in an unbalanced system only when $\langle I_{\mathrm{ref,u}} \rangle < 2e\delta\nu/\alpha$ and in a balanced system only when $\langle I_{\mathrm{sam,b}} \rangle < e\delta\nu/\alpha$. As an example, consider a good, but no longer commercially available[2], OCT light source based on a semiconduc-

[2] The light source was produced by the Canadian company AFC Technologies, which was acquired by JDS Uniphase, Canada in September 1999. Since then, the focus of the company has changed to optical amplifiers for communication.

tor optical amplifier that has been used by several researchers [18, 31, 138]. Such a light source is currently in use in the Bio-optics Laboratory at Risø National Laboratory, Denmark. The specifications of this source are a center wavelength at 1300 nm, 60 nm line width, and 20 mW output power. With these specifications, the optical noise is shot-noise dominated when $\langle I_{\mathrm{ref,u}} \rangle < 3\,\mu\mathrm{W}$ and $\langle I_{\mathrm{sam,b}} \rangle < 1.5\,\mu\mathrm{W}$, respectively. Here, it has been used that $\alpha \approx 1.0\,\mathrm{A/W}$, which is a typical value for a InGaAs photodetector at this wavelength [112, 139].

For most unbalanced OCT systems, the power from the reference, $\langle I_{\mathrm{ref,u}} \rangle$, will be well in excess of $3\,\mu\mathrm{W}$, so for such systems the optical noise will be intensity-noise limited. It is then important to notice that both the signal power and the intensity noise is proportional to the power of the light source squared (see Eqs. (5.8) and (5.9)). Accordingly, no increase of the SNR can be obtained in an unbalanced OCT system by increasing the source power, when the system is intensity noise limited.

From the requirement $\langle I_{\mathrm{sam,b}} \rangle < 1.5\,\mu\mathrm{W}$ found above, the shot-noise limit in a balanced system depends upon the structure of the sample arm. Thus, consider the system shown in Fig. 5.2 for two cases of the incoherent reflections from the sample arm: In the first case, the optics of the sample arm includes a 4 % reflection from an air/glass interface. This case is likely unless steps are taken to reduce such reflections. With the light source from above, a source irradiance of 20 mW and x set to 50 %, then $\langle I_{\mathrm{sam,b}} \rangle \approx 50\% \times 4\% \times 20\,\mathrm{mW} = 400\,\mu\mathrm{W}$, which is considerably more than the limit of $1.5\,\mu\mathrm{W}$. Accordingly, in such a system the optical noise is beat noise dominated. In the second case, the reflections from the optics of sample arm are assumed negligible. In this case $\langle I_{\mathrm{sam,b}} \rangle$ will be dominated by reflections from the sample, and most likely by the reflection from the surface. To estimate the received power from the sample surface, consider for a moment that the OCT system is probing the surface. If the surface of the sample is assumed to be diffusely reflective, the OCT signal may then be found from Eq.(4.9). To find the intensity of the reflected light from the

surface, $\langle I_{\mathrm{coh}} \rangle$, as it is probed, Eq.(4.9) is compared to Eq.(5.8):

$$\left\langle i_{\mathrm{b}}^2 \right\rangle = 2\alpha^2 T_{\mathrm{b}} \left\langle I_{\mathrm{ref,b}} \right\rangle \left\langle I_{\mathrm{coh}} \right\rangle = \alpha^2 T_{\mathrm{b}} P_{\mathrm{S}} P_{\mathrm{R}} R_{\mathrm{d}} \frac{4w_0^2}{f^2}, \tag{5.14}$$

where R_{d} is the reflectivity of the surface, $P_{\mathrm{R}} = \langle I_{\mathrm{ref,b}} \rangle$ and $T_{\mathrm{b}} P_{\mathrm{S}}$ is the optical power incident upon the sample reduced by any power loss due to transmission from the sample arm to the detector. For $x = 50\,\%$, $T_{\mathrm{b}} P_{\mathrm{S}} = x \times 20\,\mathrm{mW} = 10\,\mathrm{mW}$ (see Fig. 5.2). From Eq.(5.14), the light power entering the fiber from the surface is given by $\langle I_{\mathrm{coh}} \rangle = R_{\mathrm{d}} \frac{4w_0^2}{f^2} \times 5\,\mathrm{mW} \approx R_{\mathrm{d}} 1.3\,\mu\mathrm{W} < 1.5\,\mu\mathrm{W}$, since $R_{\mathrm{d}} \leqq 1$. Here the sample beam was chosen to have a soft focus such as that applied in the OCT system designed by Thrane *et al.* ($w_0/f = 0.008$) [17]. Because the received power from the surface is reduced as the sample beam is focused inside the sample during imaging, this implies that the optical noise will be shot-noise limited even for high reflectivities of the surface. However, it should be noted that completely reducing reflections from the sample arm optics is, at best, cumbersome, but the importance and benefit of reducing such reflections is clear.

The main conclusion of the present discussion is that the shot-noise limit is a valid limit for some special cases, but that the specific system must be considered carefully to establish this. Accordingly, the reader is cautioned not to assume shot-noise limited operation of an OCT system by default.

5.3 SNR of an OCT system with optical amplification

In this section, the two-level atomic model [126–128] of the noise properties of an optical amplifier is presented. This model is then introduced into the expressions for the noise derived in section 5.2.3, and it is found that a balanced system with optical amplification of the light reflected from the sample is the preferable setup. The expression for the SNR of this system is then derived, which constitutes the design expression that may be used in the process of optimizing a system.

5.3.1 The amplifier model

To analyze the impact of an optical amplifier in an OCT system, a simple two-level atomic model is adopted [126–128]. As discussed in the introduction this model is, for the present purpose, applicable to most types of optical amplifiers [128, 129]. Assuming small signal amplification, i.e., no gain depletion, the output field, U_{out}, of an optical travelling wave amplifier with gain G can be written as [126–128]

$$U_{\text{out}}(t) = \sqrt{G}U_{\text{in}}(t) + U_{\text{ASE}}(t), \tag{5.15}$$

where $U_{\text{in}}(t)$ is the input field and $U_{\text{ASE}}(t)$ is a field due to the noise added by the amplifier. This noise is dominated by amplified spontaneous emission [128], often referred to as ASE , which is a broadband emission with similar characteristics to the light source of an OCT system. In fact, one suitable light source for OCT is based on the shaped spectrum of a semiconductor optical amplifier [18, 31, 138]. The intensity of $U_{\text{ASE}}(t)$ is given by

$$\begin{aligned} \langle I_{\text{ASE}} \rangle &= 2n_{sp}(G-1)h\nu B_o \\ &= (G-1)s_{\text{ASE}} \end{aligned} \tag{5.16}$$

where B_{o} is the optical bandwidth of the optical amplifier, $s_{\text{ASE}} = 2n_{sp}h\nu B_o$, and n_{sp} is the inversion parameter, which depends on the amplifier at hand [126, 127]. For an ideal amplifier $n_{sp} = 1$. Fiber amplifiers have been shown to come close to this limit, although a typical value is approximately 2 [128]. Semiconductor amplifiers have typical values above 2 depending on wavelength, and for Raman amplifiers, $n_{sp} \simeq 1$, depending on the temperature and the Stoke's shift relative to the pump source (see Ref. [128] for a more elaborate comparison). The factor 2 is included in Eq.(5.16) corresponding to the fact that there are two polarization modes in a single mode fiber, and most fiber-optic OCT systems employ single-mode fibers.

5.3.2 Application of an optical amplifier and the SNR

To find the optimum use of an optical amplifier, three possible uses must be considered.

First, the amplifier may be used to amplify the reference light as well as the signal in an unbalanced setup. However, this is disadvantageous because the noise of the amplifier will contribute to the noise of the system through intensity noise as well as through beating with the amplified reference light.

Second, the amplifier may be inserted to amplify only the reference light in a balanced setup. This is advantageous since the intensity noise is suppressed, and the beat noise contribution would only be caused by interaction with the weak sample light. However, because of the relatively large reference power, the detectors and/or amplifier will generally saturate at low gains.

Finally, the amplifier may be inserted to amplify the light from the sample alone. If large unwanted reflections in the sample are reduced to a minimum, higher gains may be possible depending on the noise characteristics of the amplifier. Accordingly, this is considered to be the most efficient use of the amplifier, and the analysis is thus limited to this case in the following.

To find the SNR of a system with amplification of the light from the sample, the current noise spectral density found in section 5.2.3 must be modified using the amplifier model of section 5.3.1. A good amplifier for OCT has a relatively flat gain and matching bandwidth to the light source, so that the spectral shape of the input light is maintained. The broadband ASE noise is assumed to have the same effective optical bandwidth as the light source, i.e., $B_\mathrm{o} = \delta\nu$. The spontaneous noise emission of the optical amplifier, U_ASE, is incoherent relative to the light source, and therefore also incoherent relative to the reference. The emission will therefore contribute to the optical noise in the same manner as a field from the incoherent reflections of the sample $\sum U_{\mathrm{incoh},n}$. Using Eqs.(5.9), (5.10), and (5.15), the current noise spectral densities for the unbalanced and balanced system

are found to be

$$\begin{aligned}\left\langle \Delta i^2_{\mathrm{opt,u}} \right\rangle &= 2e\alpha \left(\langle I_{\mathrm{ref,u}} \rangle + G \langle I_{\mathrm{sam,u}} \rangle + \langle I_{\mathrm{ASE}} \rangle \right) \\ &\quad + \frac{\alpha^2}{\delta\nu} \left(\langle I_{\mathrm{ref,u}} \rangle + G \langle I_{\mathrm{sam,u}} \rangle + \langle I_{\mathrm{ASE}} \rangle \right)^2 + \left\langle \Delta i^2_{\mathrm{rec,u}} \right\rangle ,\end{aligned} \tag{5.17}$$

and

$$\begin{aligned}\left\langle \Delta i^2_{\mathrm{opt,b}} \right\rangle &= 2e\alpha \left(\langle I_{\mathrm{ref,b}} \rangle + G \langle I_{\mathrm{sam,b}} \rangle + \langle I_{\mathrm{ASE}} \rangle \right) \\ &\quad + 2\frac{\alpha^2}{\delta\nu} \langle I_{\mathrm{ref,b}} \rangle \left(G \langle I_{\mathrm{sam,b}} \rangle + \langle I_{\mathrm{ASE}} \rangle \right) + \left\langle \Delta i^2_{\mathrm{rec,u}} \right\rangle ,\end{aligned} \tag{5.18}$$

respectively. Even for an amplifier with good noise characteristics, the power of $\langle I_{\mathrm{ASE}} \rangle$ may contribute considerably to the optical noise in an unbalanced system, through the intensity noise term $\frac{\alpha^2}{\delta\nu} \langle I_{\mathrm{ASE}} \rangle^2$. It is thus concluded that the best improvement of an OCT system from inserting an optical amplifier is obtained for the balanced system, and therefore the analysis is limited to this case in the following. Such a system may be realized as shown in Fig. 5.5.

The signal power is found using Eqs.(5.8) and (5.15), and hence

$$\left\langle i^2_{\mathrm{s}} \right\rangle = 2\alpha^2 T_{\mathrm{b}} G \langle I_{\mathrm{ref,b}} \rangle \langle I_{\mathrm{coh}} \rangle , \tag{5.19}$$

and the SNR of a balanced system with optical amplification of the light from the sample arm, $\mathrm{SNR}_{\mathrm{amp}}$, is then given as

$$\begin{aligned}\mathrm{SNR}_{\mathrm{amp}} &= \frac{\alpha^2}{B_{\mathrm{e}}} T_{\mathrm{b}} G \langle I_{\mathrm{ref,b}} \rangle \langle I_{\mathrm{coh}} \rangle / \left[e\alpha \left(\langle I_{\mathrm{ref,b}} \rangle + G \langle I_{\mathrm{sam,b}} \rangle \right. \right. \\ &\quad \left. \left. + \langle I_{\mathrm{ASE}} \rangle \right) + \frac{\alpha^2}{\delta\nu} \langle I_{\mathrm{ref,b}} \rangle \left(G \langle I_{\mathrm{sam,b}} \rangle + \langle I_{\mathrm{ASE}} \rangle \right) + \left\langle \Delta i^2_{\mathrm{rec,b}} \right\rangle / 2 \right].\end{aligned} \tag{5.20}$$

This expression constitutes the new design expression for the optimum usage of an optical amplifier in an OCT system. However, this expression may be simplified using that several of the intensity components originates from the same light source with optical power $\langle I_{\mathrm{s}} \rangle$. These components may

be written as

$$\langle I_{\mathrm{ref,b}} \rangle = T_{\mathrm{R}} \langle I_{\mathrm{s}} \rangle \tag{5.21}$$

$$T_{\mathrm{b}} \langle I_{\mathrm{coh}} \rangle = T_{\mathrm{S}} R_{\mathrm{coh}} \langle I_{\mathrm{s}} \rangle \tag{5.22}$$

$$\langle I_{\mathrm{sam,b}} \rangle = T_{\mathrm{S}} R_{\mathrm{incoh}} \langle I_{\mathrm{s}} \rangle . \tag{5.23}$$

Here R_{coh} and R_{incoh} are the effective reflection coefficients for the light that is coherent and incoherent with respect to the reference, respectively. The effective reflection coefficient is defined as the product of the reflectivity of the specific reflection and any coupling loses to the fiber system. The quantities T_{S} and T_{R} are the total transmission coefficient describing the total power reduction due to transmission to and from the sample and reference arm, respectively. For the system in Fig. 5.5, $T_{\mathrm{S}} = x$ and $T_{\mathrm{R}} = R_{\mathrm{R}}(1-x)$, where R_{R} describes any losses in the reference scanning system. Inserting Eqs.(5.21), (5.22), and (5.23) into Eq.(5.20) yields

$$\begin{aligned} \mathrm{SNR}_{\mathrm{amp}} = {} & \frac{\alpha^2}{B_{\mathrm{e}}} G T_{\mathrm{R}} T_{\mathrm{S}} R_{\mathrm{coh}} \langle I_{\mathrm{s}} \rangle^2 / [e\alpha \langle I_{\mathrm{s}} \rangle (T_{\mathrm{R}} + G T_{\mathrm{S}} R_{\mathrm{incoh}}) \\ & + e\alpha \langle I_{\mathrm{ASE}} \rangle + \frac{\alpha^2}{\delta\nu} T_{\mathrm{R}} \langle I_{\mathrm{s}} \rangle (G T_{\mathrm{S}} R_{\mathrm{incoh}} \langle I_{\mathrm{s}} \rangle + \langle I_{\mathrm{ASE}} \rangle) \\ & + \left\langle \Delta i^2_{\mathrm{rec,b}} \right\rangle / 2]. \end{aligned} \tag{5.24}$$

This is the design expression used in the following sections to determine the impact of inserting an optical amplifier in an OCT system. However, simply optimizing this expression with respect to, e.g., x and G, is only sufficient when optical power constraints, such as detector saturation, is not applicable. This is the case when the irradiance of the light source is limited, which is often the case for suitable light sources for OCT [23] (see chapter 1). The design expressions with optical power constraints are the topic of section 5.5.

5.4 Advantage of an optical amplifier

In this section, the cases where an optical amplifier is an advantage are identified using the expression for the SNR derived in the previous section.

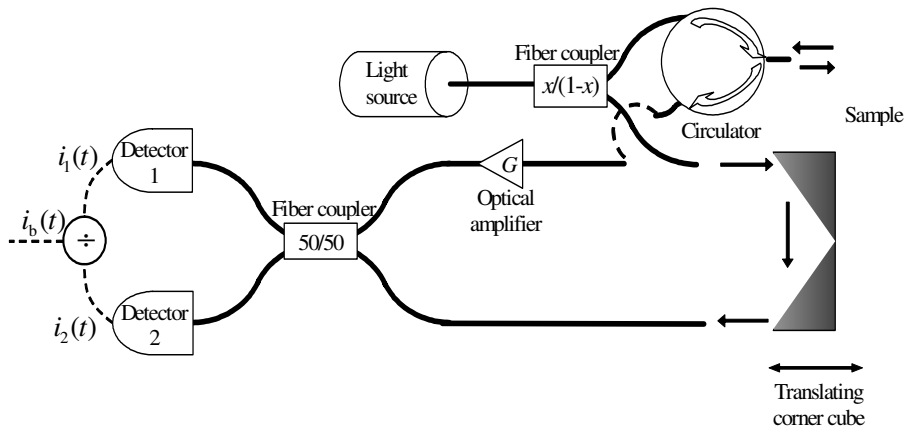

Figure 5.5: An OCT system with balanced detection and optical amplification. Besides the insertion of an optical amplifier with gain G, the setup is identical to the setup in Fig. 5.2

This is done by defining an improvement factor obtained by inserting the amplifier, and investigating when this factor is greater than unity.

To investigate the advantage of inserting an optical amplifier, the SNR is compared to the SNR of an optimized OCT system without amplification with identical light sources, identical samples, and identical reference scanning systems. In the present analysis, it is advantageous to write the current noise spectral density of the systems ($G = 1$ without amplification) as a sum of two terms:

$$\left\langle \Delta i_{\mathrm{b}}^2 \right\rangle = \left\langle \Delta i_{\mathrm{intr}}^2 \right\rangle + (G-1) \left\langle \Delta i_G^2 \right\rangle, \tag{5.25}$$

where $\left\langle \Delta i_{\mathrm{intr}}^2 \right\rangle$ is the intrinsic noise present in the system without optical amplification, and $\left\langle \Delta i_G^2 \right\rangle$ is the noise contribution from the amplifier. From Eq.(5.24) these terms may be found as

$$\left\langle \Delta i_{\mathrm{intr}}^2 \right\rangle = e\alpha \left\langle I_{\mathrm{s}} \right\rangle (T_{\mathrm{R}} + T_{\mathrm{S}} R_{\mathrm{incoh}}) + \frac{\alpha^2}{\delta\nu} T_{\mathrm{R}} \left\langle I_{\mathrm{s}} \right\rangle^2 T_{\mathrm{S}} R_{\mathrm{incoh}} + \left\langle \Delta i_{\mathrm{rec,b}}^2 \right\rangle /2, \tag{5.26}$$

and

$$\left\langle \Delta i_G^2 \right\rangle = \left(e\alpha + \frac{\alpha^2}{\delta\nu} T_{\mathrm{R}} \left\langle I_{\mathrm{s}} \right\rangle \right) (T_{\mathrm{S}} R_{\mathrm{incoh}} \left\langle I_{\mathrm{s}} \right\rangle + s_{\mathrm{ASE}}), \tag{5.27}$$

where $s_{\mathrm{ASE}} = 2n_{sp}h\nu B_o = 2n_{sp}h\nu\delta\nu$. The SNR can then be written as

$$\mathrm{SNR} = \frac{\alpha^2 G T_R T_{\mathrm{S}} R_{\mathrm{coh}} \langle I_{\mathrm{s}} \rangle^2}{\left\langle \Delta i^2_{\mathrm{intr}} \right\rangle + (G-1)\left\langle \Delta i^2_G \right\rangle}. \tag{5.28}$$

To quantify the advantage of using an optical amplifier an improvement factor, Q, is defined similarly to that in Ref. [32] as the ratio of the SNR with amplification to that without amplification:

$$\begin{aligned} Q &= \frac{\mathrm{SNR}_{\mathrm{amp}}(T_{\mathrm{S}}, T_{\mathrm{R}})}{\mathrm{SNR}_{\mathrm{b}}\left(T_{\mathrm{S},0}, T_{\mathrm{R},0}\right)} \\ &= \frac{G\left\langle \Delta i^2_{\mathrm{intr}}\left(T_{\mathrm{S},0}, T_{\mathrm{R},0}\right)\right\rangle}{\left\langle \Delta i^2_{\mathrm{intr}}\left(T_{\mathrm{S}}, T_{\mathrm{R}}\right)\right\rangle + (G-1)\left\langle \Delta i^2_G\left(T_{\mathrm{S}}, T_{\mathrm{R}}\right)\right\rangle} \frac{T_{\mathrm{S}} T_{\mathrm{R}}}{T_{\mathrm{S},0} T_{\mathrm{R},0}} \end{aligned} \tag{5.29}$$

where $T_{\mathrm{S},0}$ and $T_{\mathrm{R},0}$ are the transmission coefficient of the sample and reference arms of the system without optical amplification, respectively. The individual noise components and the SNR of each system have been written as a function of the transmission coefficients because the optimum choice of transport coefficients for each system may not be identical. It is important to note that the improvement factor is independent of the intensity of the signal reflection as long as it is negligible compared to the intensity from the reference. For large gains, the optical noise will be dominated by $\left\langle \Delta i^2_G \right\rangle$, and the maximum improvement factor is then given by

$$Q_{\max} = \frac{\left\langle \Delta i^2_{\mathrm{intr}}\left(T_{\mathrm{S},0}, T_{\mathrm{R},0}\right)\right\rangle}{\left\langle \Delta i^2_G\left(T_{\mathrm{S}}, T_{\mathrm{R}}\right)\right\rangle} \frac{T_{\mathrm{S}} T_{\mathrm{R}}}{T_{\mathrm{S},0} T_{\mathrm{R},0}}. \tag{5.30}$$

The term "maximum" is, strictly speaking, only applicable when $\left\langle \Delta i^2_{\mathrm{intr}} \right\rangle > \left\langle \Delta i^2_G \right\rangle$.

To find the cases when an optical amplifier will be an improvement, the cases for $Q > 1$ must be found. It is first noted from Eq.(5.28) that if the transmission coefficients for the system without optical amplification are optimized for maximum $\mathrm{SNR}_{\mathrm{b}}$, then

$$\mathrm{SNR}_{\mathrm{b}} = \mathrm{SNR}_{\mathrm{amp}}|_{G=1} = \frac{\alpha^2 R_{\mathrm{coh}} \langle I_{\mathrm{s}} \rangle^2 T_{\mathrm{S},0} T_{\mathrm{R},0}}{\left\langle \Delta i^2_{\mathrm{intr}}\left(T_{\mathrm{S},0}, T_{\mathrm{R},0}\right)\right\rangle} \geq \frac{\alpha^2 R_{\mathrm{coh}} \langle I_{\mathrm{s}} \rangle^2 T_{\mathrm{S}} T_{\mathrm{R}}}{\left\langle \Delta i^2_{\mathrm{intr}}\left(T_{\mathrm{S}}, T_{\mathrm{R}}\right)\right\rangle}. \tag{5.31}$$

Secondly, it is noted that the improvement factor is an monotonic function of G assuming all else is kept equal. Using Eqs.(5.29) and (5.31), the important result is obtained that inserting an optical amplifier will be an improvement if, and only if,

$$\begin{aligned} \left\langle \Delta i^2_{\text{intr}} \left(T_{\text{S},0}, T_{\text{R},0}\right)\right\rangle &> \left\langle \Delta i^2_G \left(T_{\text{S}}, T_{\text{R}}\right)\right\rangle \Longleftrightarrow \\ e\alpha \left\langle I_{\text{s}}\right\rangle T_{\text{R},0} + \left\langle \Delta i^2_{\text{rec,b}}\right\rangle /2 &> e\alpha s_{\text{ASE}} + \frac{\alpha^2}{\delta\nu}\left\langle I_{\text{s}}\right\rangle T_{\text{R}} s_{\text{ASE}}. \end{aligned} \tag{5.32}$$

Three conclusions can be made from this inequality. Firstly, an optical amplifier cannot improve an OCT system that is beat noise limited, because the beat-noise term, $\frac{\alpha^2}{\delta\nu} T_{\text{R}} \left\langle I_{\text{s}}\right\rangle^2 T_{\text{S}} R_{\text{incoh}}$, appears on both sides of Eq.(5.32). Secondly, if the system without amplification is dominated by shot noise, an optical amplifier may be able to improve the SNR. However, this requires that $eT_{\text{R},0} - T_{\text{R}} 2 n_{sp} h\nu > 0$, and if $T_{\text{R},0} \approx T_{\text{R}}$ this is not satisfied for the wavelength ranges relevant to OCT even for $n_{sp} = 1$. Finally, if the system without optical amplification is limited by receiver noise, an optical amplifier may be used to overcome this limit. Since $e\alpha \ll \frac{\alpha^2}{\delta\nu}\left\langle I_{\text{s}}\right\rangle T_{\text{R}}$ for most applications, Eq.5.32 yields

$$\begin{aligned} \left\langle \Delta i^2_{\text{rec,b}}\right\rangle &> 2\alpha^2 2 n_{sp} h\nu \left\langle I_{\text{s}}\right\rangle T_{\text{R}} - 2e\alpha \left\langle I_{\text{s}}\right\rangle T_{\text{R},0} \\ &> \left(2\frac{\alpha^2}{\delta\nu} s_{\text{ASE}} T_{\text{R}} - 2e\alpha T_{R0}\right)\left\langle I_{\text{s}}\right\rangle \end{aligned} \tag{5.33}$$

when the receiver noise dominates. This implies that the receiver noise must be larger than the added beat noise per unit gain factor of the amplifier, $2\frac{\alpha^2}{\delta\nu} s_{\text{ASE}} \left\langle I_{\text{s}}\right\rangle T_{\text{R}}$, reduced by the amount of shot noise due to the reference in order for optical amplification to be an advantage. It is also noted that the necessary $\left\langle \Delta i^2_{\text{rec,b}}\right\rangle$ is reduced for limited source irradiance, $\left\langle I_{\text{s}}\right\rangle$, and/or a high insertion loss of the reference scanner ($T_{\text{R},0} << 1$ and $T_{\text{R}} << 1$). From Eq.(5.33) it may seem tempting to reduce T_{R} in order to obtain an improvement for lower receiver noise. However, such a system would no longer have an improved SNR relative to the optimized system without amplification.

To summarize; in this section the important result was obtained that

an optical amplifier will be an advantage when receiver noise dominates, according to Eq.(5.33). As discussed in the introduction to this chapter, receiver noise is especially likely to be of practical concern for OCT systems designed for fast image acquisition. It is noteworthy that improvement is independent of the electrical bandwidth of the receiver system, B_e, (see Eq.(5.29)) for constant receiver noise density. However, the absolute SNR is inversely proportional to B_e (see Eq.(5.13)) and therefore an increase in bandwidth necessary to accommodate faster data acquisition and higher resolution (see Eqs. (1.3) and (1.4)) reduces the SNR, all else being equal. The analysis in this section is valid when the irradiance of the light source is limited, so power constraints such as detector saturation and safety limits may be ignored. The improvement and design expressions in such cases is the topic of the next section.

5.5 Detector saturation and limited power to the sample

As it will seen, the power constraints of detector saturation and an upper limit on irradiation of the sample, are important design considerations in OCT systems with optical amplification. To find the appropriate design expressions for such systems, these constraints will be considered explicitly in this section using the expression for the SNR derived above. For each case, the improvement factor, Q, is investigated similarly to the analysis in section 5.4 to determine if an improvement is possible from optical amplification. The explicit incorporation of power constraints is new within detailed noise analysis of OCT systems. This model also applied for G=1, and thus extends the capabilities of the analysis of conventional systems. This is used when the system with optical amplification is compared to the optimized conventional system to obtain the improvement factor.

In the following each power limitation will be considered separately and in combination. First, in section 5.5.1, the irradiation of the sample is limited while detector saturation is not a limiting factor. Second, in section 5.5.2, the detector saturation limit is obtained, but there is no limitation of the irradiation of the sample. The system is said to be

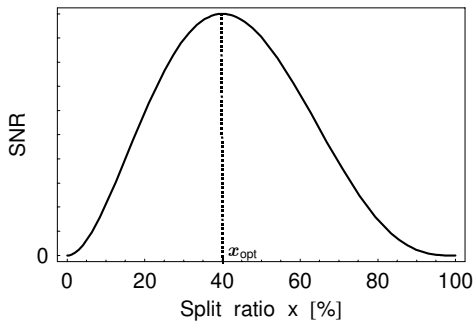

Figure 5.6: Illustrative example of the SNR as a function of split ratio x. The maximum SNR is found for the optimum split ratio x_{opt}.

in the *detector saturation limit*, when the optical power incident on the balanced detector system just saturates the detectors. Finally, in section 5.5.3, detector saturation is obtained, while the sample is irradiated by the maximum optical power according to a safety limit. This case is especially interesting, because a further increase in source power is not possible and thus cannot be used to suppress receiver noise.

In the following, the split ratio x, signifying the fraction of the optical power transmitted to the sample (see Fig. 5.2), is an important design parameter, and it is therefore illustrative first to consider the dependence on x of the SNR. With $x = 0$ or $x = 1$ there is no signal, i.e., SNR=0. Between these two extremities there is a single optimum SNR for the split ratio x_{opt}. Figure 5.6 shows an illustration of a typical curve for the SNR as a function of x, where the optimum split ratio for this example is obtained for $x_{\mathrm{opt}} = 40\%$. The shape of this curve is specific to the system configuration, but the qualitative shape is general. As it will be seen in the following sections, power constraints may influence the available settings of the split ratio, and it is thus crucial to determine which split ratio that yields the best SNR. To simplify the follow analysis, the systems previously mentioned and shown in Fig. 5.2 and Fig. 5.5 are, with little loss of generality, chosen to represent the system with and without optical amplification, respectively.

5.5.1 Safety limitation on the optical irradiation of the sample

Consider the first case where the irradiation of the sample is limited to an intensity value $\langle I_{\mathrm{sam,max}} \rangle$ due to safety considerations, and detector saturation is not a limiting factor. With sufficient source power, this restriction will limit the fraction of the source power transmitted to the sample, and thus the split ratio, x, to (see Figs. 5.2 or 5.5)

$$x \leqq \langle I_{\mathrm{sam,max}} \rangle \,/\, \langle I_{\mathrm{s}} \rangle \,. \tag{5.34}$$

To find the optimum split ratio for the system, consider the qualitative shape of the SNR as a function of x in Fig. 5.6. From this curve it is seen that if $x_{\mathrm{opt}} < \langle I_{\mathrm{sam,max}} \rangle \,/\, \langle I_{\mathrm{s}} \rangle$, then x_{opt} is the optimum choice of split ratio for the particular system. In this case, the safety limit has no influence on the settings of the system, and therefore the analysis of the SNR in section 5.4 still applies. If, on the other hand, $x_{\mathrm{opt}} > \langle I_{\mathrm{sam,max}} \rangle \,/\, \langle I_{\mathrm{s}} \rangle$ then the split ratio must be reduced from this value to accommodate the requirement of Eq.(5.34). To obtain optimum performance in this case, a systems designer will minimize the change of x from x_{opt} and use

$$x = \langle I_{\mathrm{sam,max}} \rangle \,/\, \langle I_{\mathrm{s}} \rangle \,. \tag{5.35}$$

By inserting this constraint into Eq. (5.24) the design expression for the SNR of this case is obtained.

One may then proceed to find the improvement similarly to the analysis of section 5.4. However, as the necessary shift from optimum x is independent of the optical amplifier, the impact on the improvement factor is expected to be minimal and the above conclusions from Eq.(5.32) are still valid. Therefore, this case is not considered separately in the remainder of this thesis.

5.5.2 Detector saturation limit

The topic of this section is to derive the design expression of a system with optical amplification of the reflected light from the sample, when the

detector saturation limit is obtained for $x = x_{\text{opt}}$ (or $x > x_{\text{opt}}$ as it will be seen below). This may be from the irradiance of the light source alone or in combination with the output of an optical amplifier. Furthermore, it is assumed that no safety limitation on the irradiation of the sample is inferred. The design expression is derived by first determining the best way of accommodating the added optical power in the system when the gain, G, is increased ($G = 1$ without an amplifier), and then combining this method with the expression for the SNR in Eq. (5.24). It is then important to determine the maximum gain setting of the optical amplifier. Finally, it is important to establish whether an improvement may be obtained by further increasing the gain when detector saturation is obtained, or by inserting an optical amplifier into a system where the irradiance of the light source is sufficient to saturate the detectors alone. This is not intuitively clear, since the discussed adjustment to accommodate the added optical power will reduce the SNR of the initial system, which must then be compensated by the amplifier.

Design expression

The total optical power impinging on the balanced detector system is given by

$$\begin{aligned} \langle I_{\text{det,tot}} \rangle &= \langle I_{\text{ref,u}} \rangle + G \langle I_{\text{sam,b}} \rangle + \langle I_{\text{ASE}} \rangle \\ &= \langle I_{\text{s}} \rangle (T_{\text{R}} + G T_S R_{\text{incoh}}) + s_{\text{ASE}}(G-1), \end{aligned} \tag{5.36}$$

where $G = 1$ in the system without an optical amplifier, and $\langle I_{\text{coh}} \rangle$ has been assumed negligible relative to $\langle I_{\text{sam,b}} \rangle$. With a finite detector saturation power of the balanced detector system, $\langle I_{\text{det,max}} \rangle$, and using that the transport coefficient for the considered system (see Fig. 5.5) are given by $T_{\text{S}} = x$ and $T_{\text{R}} = R_{\text{R}}(1-x)$, the restriction of detector saturation results in the inequality

$$\begin{aligned} \langle I_{\text{det,max}} \rangle &\geq \langle I_{\text{det,tot}} \rangle \\ &\geq \langle I_{\text{s}} \rangle [R_{\text{R}}(1-x) + G x R_{\text{incoh}}] + s_{\text{ASE}}(G-1). \end{aligned} \tag{5.37}$$

If detector saturation is obtained, the system must be adjusted if the gain is to be increased. From Eq.(5.37) it is then given that there two options: A reduction in power of the light source, $\langle I_\mathrm{s} \rangle$, or an increase in x away from optimum. An increase in x will guide a larger percentage of the source power toward the sample. With its lower reflectivity relative to the reference, such an increase will serve to "spill" the optical power, and thereby reduce the total power impinging on the detectors. This argument is valid when $R_\mathrm{incoh} < R_\mathrm{R}$, which should be obtainable even when the insertions loss of the reference scanner is high ($R_\mathrm{R} << 1$), if some effort has been made to reduce undesired reflections in the sample arm.

To determine which of the above options that results in the minimum reduction in SNR of the initial system, consider the signal power of the system. From Eq.(5.8)

$$\left\langle i_\mathrm{s}^2 \right\rangle \propto \langle I_\mathrm{coh} \rangle \langle I_\mathrm{ref,b} \rangle \,. \tag{5.38}$$

Now, consider the case where the power from the reference scanner $\langle I_\mathrm{ref,b} \rangle = R_\mathrm{R}(1-x)\langle I_\mathrm{s} \rangle$ is dominating the optical power impinging on the detectors, which is the case for most conventional OCT systems. From this assumption it is given that the necessary reduction in power from the reference as the gain is increased, will be of approximately the same magnitude whether it is reduced by an increase in x or a decrease in $\langle I_\mathrm{s} \rangle$. As a decrease in source power, $\langle I_\mathrm{s} \rangle$, will decrease the power from the reference as well as from the sample, it is given that an increase in x is most advantageous because it results in an increased power from the sample. If, on the other hand, the power from the sample arm is a significant contribution to the power incident on the detectors; reducing source power, and then increasing the amplification of the sample light, will result in approximately the same power from the sample to the detector, but with added amplifier noise. Thus, if the system is completely saturated, then no adjustment of the split ratio is possible to accommodate additional power, and increased gain is not an advantage.

Having established that adjusting x is the best method to accommodate the power added by increasing gain, the question is now how to determine

the most advantageous split ratio to obtain the best SNR. From Eq.(5.37) it is then found that

$$x \geq \frac{s_{\mathrm{ASE}}(G-1) + \langle I_{\mathrm{s}} \rangle R_{\mathrm{R}} - \langle I_{\mathrm{det,max}} \rangle}{\langle I_{\mathrm{s}} \rangle (R_{\mathrm{R}} - G R_{\mathrm{incoh}})}, \tag{5.39}$$

where it has been assumed that $G < R_{\mathrm{R}}/R_{\mathrm{incoh}}$ (to be discussed below). For the present case, it is assumed that detector saturation is obtained with $x \geq x_{\mathrm{opt}}$, because if x can be increased to x_{opt} the SNR would be improved (see Fig. 5.6), but the system would no longer be saturated. With $x \geq x_{\mathrm{opt}}$ given, it may now be seen from Fig. 5.6 that the best split ratio for a given amplifier gain, G, is the minimum value of x for which Eq.5.39 is maintained so

$$x = \frac{s_{\mathrm{ASE}}(G-1) + \langle I_{\mathrm{s}} \rangle R_{\mathrm{R}} - \langle I_{\mathrm{det,max}} \rangle}{\langle I_{\mathrm{s}} \rangle (R_{\mathrm{R}} - G R_{\mathrm{incoh}})}. \tag{5.40}$$

With the simple argument used to realize that x must be minimized, it was assumed that the split ratio for optimum SNR, x_{opt}, is approximately independent of G. This assumption is correct when the system is receiver noise dominated, since in this case the noise is independent of x while the signal is proportional to $GT_{\mathrm{S}}T_{\mathrm{R}} \propto Gx(1-x)$. Accordingly, the maximum SNR is obtained for maximum signal, i.e., x_{opt}= 50%. However, it is noted that from Eq.(5.24) it may be shown that the split ratio for optimum SNR, x_{opt}, will in general decrease for increased gain, which implies that the argument leading to Eq. (5.40) is general (see Fig. 5.6). Finally, it is noted that from Fig. 5.6 it may seem that increased gain will reduced the SNR due to the necessary increase in split ratio. However, it should be noted that Fig. 5.6 is plotted for constant G, and therefore any upward scaling of the curve cannot be determined. The potential of improvement by inserting an optical amplifier, or increasing the gain of an inserted optical amplifier, is determined in the analysis of the improvement factor below.

The design expression for the present case is obtained by inserting Eq.(5.40) into the expression for the SNR in Eq. (5.24) (not shown for brevity). Quantitative analysis of this design expression is exemplified in section 6.1.3 of the next chapter.

Saturation gain

To find the maximum allowable gain of the amplifier it is noted that to obtain Eq.(5.39) it was assumed that $G < R_{\mathrm{R}}/R_{\mathrm{incoh}}$. If instead $G > R_{\mathrm{R}}/R_{\mathrm{incoh}}$, it may be seen from Eq.(5.37) that the power from the sample (or amplifier output) is sufficient to require reduction in $\langle I_{\mathrm{s}} \rangle$ with an increase in G. The system may then be said to be saturated, and with the same arguments of system saturation above, it is realized that further amplification of the light from the sample reduces SNR. The maximum gain in the present case is then found as the maximum value for which

$$G < R_{\mathrm{R}}/R_{\mathrm{incoh}} \text{ and } G < \frac{\langle I_{\mathrm{det,max}} \rangle + s_{\mathrm{ASE}}}{\langle I_{\mathrm{s}} \rangle R_{\mathrm{incoh}} + s_{\mathrm{ASE}}}, \tag{5.41}$$

where the latter condition is obtained using Eq.(5.39) and that $x < 1$. This gain value is denoted the *saturation gain*. It is noted that large values of R_{incoh} will reduce the saturation gain, and therefore the obtainable improvement using an optical amplifier. This point is emphasized in the quantitative analysis of this case given in section 6.1.3.

Improvement

Finally, to determine whether inserting an optical amplifier, or increasing the gain of an inserted optical amplifier, may render an improvement for a system in the detector saturation limit, it is first noted that the SNR of the initial OCT system is reduced by the necessary adjustment of x when the gain is increased. In section 5.4 it was concluded that optical amplification is only an advantage when the system is receiver noise dominated. With the initial reduction of the SNR, it is then concluded that this is also true in the present case.

If it is assumed that receiver noise dominates the noise contributions in the system completely, and that the output from the amplifier is small relative to the power from the reference, it may be shown by using the design expression (Eqs. (5.24) and (5.40)) and Eq.(5.29) that the improvement

factor can be approximated by

$$Q \approx \frac{G\left[s_{\mathrm{ASE}}(G-1)+\langle I_{\mathrm{s}}\rangle R_{\mathrm{R}}\right]}{G_0\left[s_{\mathrm{ASE}}(G_0-1)+\langle I_{\mathrm{s}}\rangle R_{\mathrm{R}}\right]} > 1 \text{ for } G > G_0, \tag{5.42}$$

where G_0 is the gain in the amplifier in the initial system, and it is noted that $G_0 = 1$ when the initial system is saturated by the irradiance of the light source alone.

Equation (5.42) demonstrates that an optical amplifier may improve the SNR under the given assumptions. The quantification of the obtainable improvement, relieved of these assumptions, is the topic of section 6.1.3 in the next chapter. It should be noted that it cannot necessarily be inferred from Eq.(5.42) than an insertion loss of the reference scanner, i.e., a reduction in R_{R}, will result in an increased improvement. This is due to the requirement of detector saturation limit for the present case, which will require a corresponding increase in $\langle I_{\mathrm{s}}\rangle$ or G. However, if a higher gain is possible, additional improvement may be obtained as it will be seen in section 6.1.3.

The conclusion of the present analysis is that an optical amplifier will be an advantage, even when detector saturation is obtainable from the irradiance of the light source alone. It is also concluded that if detector saturation is obtained in combination with an optical amplifier, increasing gain may also be an advantage. However, in both cases the initial system must be receiver noise dominated, and the power impinging on the detector from the sample must be negligible compared to the power from the reference. Accordingly, undesired large reflections in the sample arm must be reduced to a minimum.

5.5.3 Detector saturation and maximum irradiation of the sample

The final case is the case of detector saturation combined with a limit on the irradiation of the sample. As in the previous case, the topic of this section is to determine the design expression specific to this case, the saturation gain, and whether an improvement by inserting an optical amplifier, or

increasing the gain of an inserted optical amplifier, may be obtained. The present case is applicable when the power of the light source is sufficient to irradiate the sample by the maximum optical power according to a safety limit, while detector saturation is obtained. This is the maximum allowable source power and thus the system may be said to be completely saturated. However, in contrast to the previous case, the optical power from the sample is *not* necessarily a significant contributor to the saturation of the detectors. As in the previous case, the initial system must be adjusted in order to accommodate the added optical power when increasing gain ($G = 1$ without amplification). Because the split ratio is determined by the restriction that the maximum power is sent to the sample, an increase in x is not possible. Instead a reduction of the source power is necessary to accommodate the power added from the increased gain of an optical amplifier.

Design expression

With the assumption of saturation, the maximum intensity, $\langle I_{\mathrm{sam,max}} \rangle$, is transmitted to the sample. Accordingly the split ratio is determined by

$$x = \langle I_{\mathrm{sam,max}} \rangle \,/\, \langle I_{\mathrm{s}} \rangle \tag{5.43}$$

(see section 5.5.1). Using this, and the condition for detector saturation from the previous section, Eq.(5.37), the maximum source power for the system and therefore the best SNR is found as

$$\langle I_{\mathrm{s}} \rangle = \frac{\langle I_{\mathrm{det,max}} \rangle - s_{\mathrm{ASE}}(G-1) + \langle I_{\mathrm{sam,max}} \rangle \left(R_{\mathrm{R}} - GR_{\mathrm{incoh}}\right)}{R_{\mathrm{R}}}. \tag{5.44}$$

Inserting Eq.(5.44) into the expression for the SNR in Eq. (5.24), yields the design expression for the SNR for the present case (not shown for brevity). Quantitative analysis of this design expression is exemplified in section 6.1.4 of the next chapter.

Saturation gain

The saturation gain for the present case is reached when a negative source power is required from Eq.(5.44). The saturation gain is then found as

$$G = \frac{\langle I_{\mathrm{det,max}} \rangle + R_{\mathrm{R}} \langle I_{\mathrm{sam,max}} \rangle + s_{\mathrm{ASE}}}{R_{\mathrm{incoh}} \langle I_{\mathrm{sam,max}} \rangle + s_{\mathrm{ASE}}}. \tag{5.45}$$

As in the previous case the reflectivity of the incoherent reflections is seen to reduce the saturation gain, and must therefore be minimized to obtain the optimum increase in SNR from inserting an optical amplifier.

Improvement

Finally, to investigate whether optical amplification is beneficial in the present case, it is assumed that receiver noise completely dominates the system, and that the light from incoherent reflections is small relative to the detector saturation limit, $\langle I_{\mathrm{det,max}} \rangle >> R_{\mathrm{incoh}} \langle I_{\mathrm{sam,max}} \rangle$. From the design expression (Eqs. (5.24) and (5.45)) and Eq.(5.29) it may then be shown that

$$Q \approx \frac{G\left[\langle I_{\mathrm{det,max}} \rangle - s_{\mathrm{ASE}}(G-1) - GR_{\mathrm{incoh}} \langle I_{\mathrm{sam,max}} \rangle\right]}{G_0\left[\langle I_{\mathrm{det,max}} \rangle - s_{\mathrm{ASE}}(G_0-1) - G_0 R_{\mathrm{incoh}} \langle I_{\mathrm{sam,max}} \rangle\right]} > 1, \; G > G_0 \tag{5.46}$$

for moderate values of G and R_{incoh}. For the case where the initial system is without amplification, the improvement is given by

$$Q \approx G \frac{\left[\langle I_{\mathrm{det,max}} \rangle - s_{\mathrm{ASE}}(G-1) - GR_{\mathrm{incoh}} \langle I_{\mathrm{sam,max}} \rangle\right]}{\langle I_{\mathrm{det,max}} \rangle} > 1. \tag{5.47}$$

The quantification of the obtainable improvement, relieved of these assumptions, is the topic of section 6.1.4 in the next chapter. From Eqs.(5.46) and (5.47) it is seen that the improvement may be reduced for higher gain values and/or large values of R_{incoh}. Accordingly, the improvement factor is expected to increase with increased gain to a maximum value, after which it decreases again. However, all details of Eqs.(5.24) and (5.44) are necessary to determine the optimum gain, and this is therefore best done numerically.

From Eqs.(5.46) and (5.47) it is concluded that improvement of the SNR is obtainable for the present case when increasing optical gain. Either in a system with an optical amplifier, or by inserting an optical amplifier into a system where the irradiance of the light source is sufficient to obtain saturation. This case is particularly important because source irradiation cannot be increased to suppress receiver noise.

5.6 Summary

In this section, a new analytical noise model of an OCT system with an optical amplifier inserted to amplify the reflected light from the sample was presented. First, a detailed noise analysis of a conventional OCT system was derived for a balanced, as well as an unbalanced detection system based on a previously published model [37]. Because optical shot-noise limited operation is often assumed in the literature, the applicability of this assumption was given special attention. The somewhat surprising conclusion of this analysis was that shot-noise limit is only obtained in special cases. From the analysis of conventional OCT systems, it was concluded that it is necessary to use a balanced detector system to obtain the best advantage of an optical amplifier, and the best use of an amplifier is obtained when it is inserted to amplify only the reflected light from the sample. To describe the effect of an optical amplifier, a theoretical two-level atomic model was introduced [126–128] and a new design expression for the SNR of a system with optical amplification was derived. To quantify the improvement obtained using an optical amplifier, an improvement factor was defined as the ratio of the SNR with amplification to the SNR without amplification. The new model of the SNR, and the improvement factor was accompanied by a detailed analysis of the effects of detector saturation and/or a safety limit on the irradiation of sample. The analysis of each applicable case of these power constraints resulted in specific design expressions. When applicable, the maximum gain factor of the optical amplifier was determined. The explicit inclusion of power constraints is new to noise analysis of OCT systems, which are not necessarily shot-noise limited. Therefore, this analysis also extends the capabilities of the analysis of conventional systems.

The main conclusion of the analytical noise model was that an optical amplifier will improve the SNR of a system that is receiver noise dominated. This improvement may be obtained in spite of the above mentioned power limitations. For several of the discussed cases, the sum of the reflections from the sample arm incoherent with respect to the reference, R_{incoh}, turned out to be an important parameter, which must be minimized to obtain optimum SNR. The derived design expressions for the SNR may now serve as a design model for future systems, and be applied to determine whether an optical amplifier may be an advantage in a specific OCT system.

Chapter 6

Optical amplification in OCT: Results and implications

In this chapter, the improvement of SNR by inserting an optical amplifier in an OCT system will be quantified for fast-scanning OCT systems using the new model presented in the chapter 5. The effect of such an improvement on the imaging penetration depth of the system is then exemplified for skin using the results of chapter 4. Finally, as a novelty, the impact of an optical amplifier on the coherence of the amplified light, and the resulting OCT signal, is briefly discussed using the results of a preliminary experiment.

6.1 Quantitative analysis of a fast-scanning system

In this section, the quantitative improvement of inserting an optical amplifier to amplify the light reflected from the sample is investigated in a set of specific cases of fast scanning OCT systems. The analysis is focused on fast-scanning systems because of their practical importance (see chapter 1), and because of the larger potential of SNR improvement by inserting an optical amplifier in such systems (see section 5.1). The new model presented

in the previous chapter included a relatively large set of parameters, each with several values all relevant for practical OCT systems. In the following, the analysis is divided into three important cases depending on the power of the light source at hand, and the sample being probed. Case 1, where the irradiance of the light source is limited, so that power limitations are not a consideration; Case 2, where the power of the light source if sufficient to saturate the detector system, and Case 3, where a constraint is added on the optical power impinging on the sample due to safety considerations. In all of these cases special attention is given to the important case of a high insertion loss in the reference scanner, and the impact of a large undesired reflection in the sample arm. As in the analytical analysis of chapter 5, the improvement in SNR due to the amplifier is measured relative to an optimized system without amplification for identical light sources, samples, and reference scanners.

Besides the quantification of the impact of optical amplification, the presented numerical examples are also included to aid the reader in getting a qualitative understanding of the new noise model. The discussion of the functionality of the improvement factor is, therefore, sometimes slightly elaborated.

6.1.1 System parameters

In the following numerical examination of the improvement factor, the design expression relevant to each case is used. These expressions are given by Eq.(5.24) in Case 1, Eqs.(5.40) in combination with Eq.(5.24) in Case 2, and Eq.(5.44) in combination with Eq.(5.24) in Case 3. The OCT systems in Fig. 5.2 and Fig. 5.5 are chosen as the system with and without optical amplification, respectively. The following set of system parameters are

common to the examples when nothing else is stated:

$$
\begin{aligned}
R_{\text{incoh}} &= \begin{cases} 3 \times 10^{-5}, \text{ coated case} \\ 0.04, \text{ uncoated case} \end{cases} \\
\langle I_{\text{det,max}} \rangle &= 2\,\text{mW, detector saturation power} \\
\alpha &= 1.0\,\text{A/W, detector responsivity at } 1300\,\text{nm.} \\
\lambda_{\text{c}} &= 1300\,\text{nm} \\
\Delta\lambda &= 80\,\text{nm } (\delta\nu = 14.2\,\text{THz}) \\
T_{\text{S}} &= x, \text{ where } x \text{ is set to the value for best SNR.} \\
T_{\text{R}} &= R_{\text{R}} \times (1 - x) \\
R_{\text{R}} &= \begin{cases} 1.0, \text{ ideal reference scanner} \\ 0.1, \text{ 90\% insertion loss} \end{cases} \\
n_{sp} &= 2
\end{aligned}
$$

The coated and uncoated case refers to the specifications of the accumulated incoherent reflections in the sample arm of the system. The accumulated incoherent reflections is the sum of light reflected in the sample arm, which may be considered incoherent with respect to the light from the reference. In the uncoated case, these reflections are dominated by a single undesired air-to-glass interface in the optics related to the sample arm. In the coated case, this reflection has been reduced, i.e., by coating or by angling of the interface. The value of R_{incoh} is then an estimated value based on the sum of the Rayleigh backscattering in the fiber (approximately 10^{-5} [32, 37]), a diffusely reflecting surface of the sample with reflectivity of 0.05 (see section 5.2.5), discontinuities within the sample and distributed backscattering from the sample. The detector saturation power, $\langle I_{\text{det,max}} \rangle$, and responsivity, α, are specifications of the New Focus 1611reciever discussed below [139]. When loss in the reference arm is considered, the quantity $R_{\text{R}} = 0.1$ is used, corresponding to the 90% insertion loss of the Fourier-domain rapid-scan optical delay line [26]. The quantities λ_{c} and $\Delta\lambda$ are the center wavelength and optical bandwidth of the light source, respectively. Finally, $\delta\nu$ and B_{o} are the matched optical linewidths of the broadband light source and optical amplifier, respectively.

Receiver noise

In chapter 5, it was concluded that the benefit of an optical amplifier is the suppression of noise contributions from the electrical receiver noise system relative to the optical noise. Accordingly, the receiver noise is an essential parameter for the following investigations. The front-end receiver, i.e., photodiode and the first electrical amplifier, is especially important. Firstly, any degradation of the SNR by the front-end cannot be reduced by a subsequent electrical amplification. Secondly, the gain in the front-end determines, to some degree, the vulnerability of the system to other electrical noise sources. With low gain, any noise sources added to the electrical system after the front-end, either from other electrical devices in the system, or from environmental coupling, will be proportionally larger compared to the signal. Estimating this noise is, at best, difficult when the entire electrical system of filters, digital-to-analog converters, etc., are included. Finally, any electrical field coupling into the electrical circuits from a laboratory- or clinical environment must also be included. Together, these contributions may be quite significant compared to the noise of the photoreceiver itself. Therefore, a more descriptive term for the total receiver noise could be *electrical noise*.

Because detailed analysis of the receiver front-end, is outside the scope of this thesis, the specifications of the New Focus 1617 balanced detector front-end are used throughout the cases of this section [139]. This detector has been chosen because of its relatively wide bandwidth of 40 kHz to 850 MHz, which is considered to be suitable for fast scanning applications now and in the near future (see chapter 1). The saturation power of this detector system is $\frac{1}{2}\langle I_{\mathrm{det,max}}\rangle = 1\,\mathrm{mW}$ incident on each detector, and the minimum noise equivalent power (NEP) is $20\,\mathrm{pW\,Hz^{-1/2}}$. The current noise spectral density due to optical shot noise corresponding to maximum incident optical power is $2\alpha \times e \times 2\,\mathrm{mW} = 6.4 \times 10^{-22}\,\mathrm{A^2\,Hz^{-1}}$, whereas the current noise spectral density due to receiver noise is $\alpha^2\mathrm{NEP}^2 = 4\times10^{-22}\,\mathrm{A^2\,Hz^{-1}}$. This implies that with maximum incident optical power, the front-end will be either shot-noise limited or beat-noise limited. However, it is clear that with a small reduction in incident optical power, or with

a small contribution to the electrical noise introduced after the front-end, the electrical noise will dominate the noise of the system.

As discussed above, the gain of the receiver front-end is essential to noise rejection of the electrical system. To accommodate a lower response time in a faster detector, the gain of the receiver front-end must be reduced [130]. The 1617 detector has a conversion gain of 700 V/A, which is relatively low compared to 1.5×10^7 V/A, which is the maximum conversion gain of the slower (200 kHz) New Focus 2011 receiver [140]. The increased noise sensitivity due to a low conversion gain is well illustrated by an experiment in which the electrical noise was measured from a balanced receiver setup comprising of two 2011 receivers and circuitry to obtain the difference signal. The results and details of the experiment may be found in Appendix B. The electrical noise added to the receiver noise is, in the following, incorporated by considering three cases of the electrical noise $\left\langle \Delta i^2_{\mathrm{rec,b}} \right\rangle$: 1, 10 and 100 times the specified receiver noise of the 1617 balanced receiver. These cases are denoted the low-, medium- and high-noise case, respectively:

$$\left\langle \Delta i^2_{\mathrm{rec,b}} \right\rangle = \begin{cases} 4 \times 10^{-22}\,\mathrm{A^2\,Hz^{-1}}, & \text{low-noise case} \\ 4 \times 10^{-21}\,\mathrm{A^2\,Hz^{-1}}, & \text{medium-noise case} \\ 4 \times 10^{-20}\,\mathrm{A^2\,Hz^{-1}}, & \text{high-noise case} \end{cases}$$

The remaining parameters, such as source power and gain of the amplifier, are specified in the following examples.

6.1.2 Case 1: Low-irradiance light source

As discussed in chapter 1 and section 5.1, the power of a suitable OCT light source is likely to be limited to low values. With limited irradiance of the light source, it is assumed that power limitations, such as detector saturation, can be ignored. However, for the discussion of the functionality of the noise model, some graphs are extended into a regime where power limitations are considered in subsequent sections. Accordingly, for high values of the source power or amplifier gain the shown improvement should not be considered physically obtainable, unless a detector with a high satu-

ration power can be obtained. The present case was described analytically in section 5.4, and the improvement factor was given as Eq.(5.29).

Improvement for lossless reference scanner; $R_{\mathbf{R}} = 1$

In Figs. 6.1a and 6.1b the improvement factor is plotted as function of source power for the coated and uncoated case, respectively. The amplifier gain is set to $G = 20\,\mathrm{dB}$, and the improvement factor is plotted for the three cases of receiver noise power. It is seen that there is a substantial improvement over the optimized system without amplification for all three cases of the receiver noise.

From the graphs it is seen that the best improvement is obtained in the high noise case. This is expected, since the advantage of an optical amplifier is the suppression of electrical noise relative to the optical noise (see section 5.4). For all three cases of the electrical noise, it can be seen that the improvement factor is decreasing for increased source power. This corresponds to the optical noise increasing relative to the receiver noise, and thereby reducing the impact of the amplifier. The effect of beat noise, due to the incoherent reflections in the sample arm, is observed for modest and high values of the source power where a significant power is reflected, see section 5.2.3. The added optical noise reduces the impact of suppressing the electrical noise, and therefore the improvement factor. The added beat noise in the uncoated case also has the effect of masking the penalty of inserting the amplifier, when the system is dominated by optical noise due to higher values of the source power.

Improvement for high insertion loss in the reference scanner; $R = 0.1$

A loss in the reference arm increases the necessary power of the light source for which the optical noise dominates. This is vital because the power of the light source may be limited to a low value [23]. Since the split ratio, x, is optimized for maximum SNR for the system for a given set of system parameters, any loss in the reference arm is expected to act as a scaling factor on the power of the light source. This effect can be seen in Fig. 6.2a

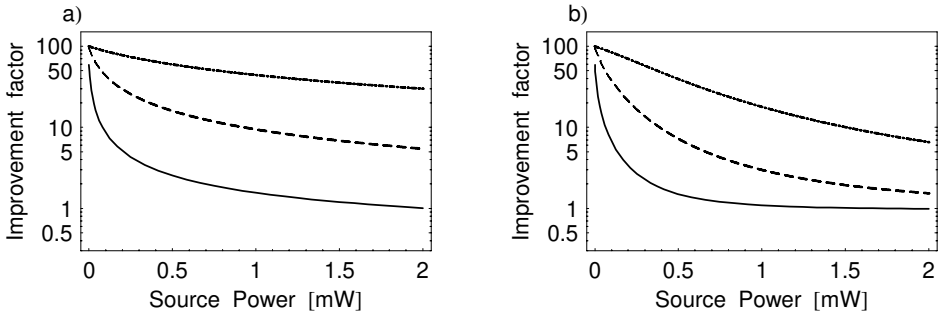

Figure 6.1: Improvement factor as a function of source power for the low-noise case (solid), medium-noise case (dash) and high-noise case (dot-dash). a) The coated case. b) the uncoated case. The gain of the optical amplifier is 20dB.

where Fig. 6.1a has been replotted for a 90% insertion loss of the reference scanner. As expected, the improvement factor for $\langle I_s \rangle = 10\,\mathrm{mW}$ in Fig. 6.2a corresponds to the improvement factor for $\langle I_s \rangle = 1\,\mathrm{mW}$ in Fig. 6.1a. This means that for a given source power, an optical amplifier will be more advantageous with increased insertion loss of the reference system.

In Fig. 6.2b the improvement factor is plotted as a function of amplifier gain for $\langle I_s \rangle = 2\,\mathrm{mW}$. This plot is included to illustrate two important functionalities: Firstly, this plot illustrates that the improvement factor is a monotonic function of the gain, G, as discussed in section 5.4. Secondly, Fig. 6.2b shows, as expected from Eq.(5.30), that a maximum improvement factor is reached after which additional gain has no effect. This limit corresponds to the electrical noise being completely dominated by optical noise. However, it should be noted that for the New Focus 1611 receiver, the amplifier noise alone saturates the detectors for $G = 23.4\,\mathrm{dB}$. The effects of saturation due to the amplifier are included in Case 2.

Improvement for limited source power and amplifier output

It was previously discussed that high demands on spectral width and shape of the light source is likely render to the available optical source power limited to a low value [23]. From Figs. 6.1 and 6.2 it was concluded that an optical amplifier is especially advantageous for low levels of the source

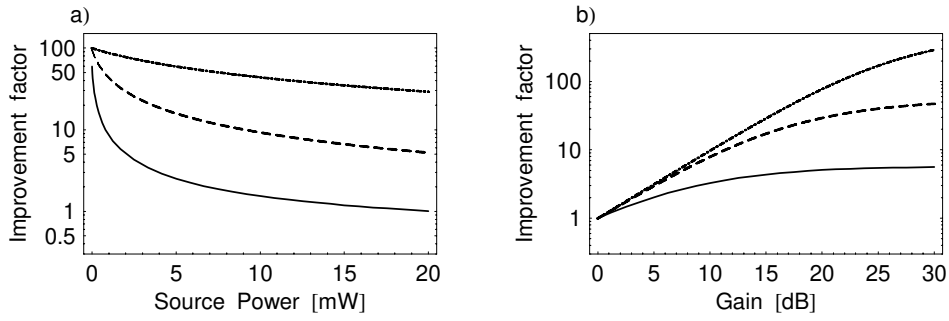

Figure 6.2: Improvement factor for a system with a 90% insertion loss of the reference scanner in the coated case for the three cases of electrical noise: low-noise case (solid), medium-noise case (dash) and high-noise case (dot-dash). a) Improvement factor as a function of source power with a gain of 20 dB. b) The improvement factor as a function of gain with $\langle I_s \rangle = 10\,\mathrm{mW}$.

power. However, the stringent requirements of the light source will naturally also apply to the amplifier rendering the total output power the amplifier limited[1]. It is therefore considered likely that a while system designer is unable to obtain a light source with sufficient irradiance, a suitable amplifier may will be available instead.

Consider an example where a suitable light source with 150nm bandwidth has been constructed together with a corresponding amplifier. Such devices have, to the best of my knowledge, not yet been constructed. However, bandwidths of this order may be necessary for very high-resolution applications, and it is considered likely that both devices will have a limited output power. Both devices are taken to have a maximum output power of $\langle I_s \rangle$ =0.4mW. For such a low source power, the amplifier output will be dominated by amplifier noise. The maximum obtainable gain may then be found from the limitation of the output to (see Eq. (5.15))

$$\begin{aligned} G\langle I_{\mathrm{sam,b}}\rangle + \langle I_{\mathrm{ASE}}\rangle &= GT_S R_{\mathrm{incoh}}\langle I_s\rangle + (G-1)s_{\mathrm{ASE}} \\ &\approx (G-1)2n_{sp}h\nu\delta\nu = \langle I_s\rangle \Leftrightarrow \end{aligned} \tag{6.1}$$

[1] If this was not the case, it is likely that the technology used to construct the amplifer, is just as well used to construct a suitable broadband light source.

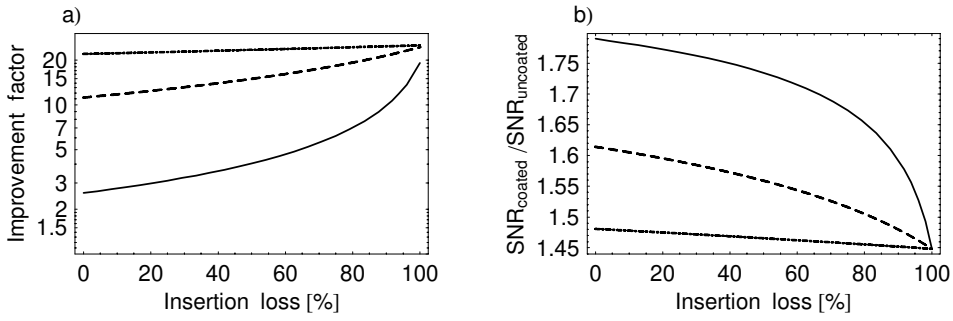

Figure 6.3: Improvement factor for a system with low optical power of the light source and amplifier for the three cases of electrical noise: low-noise case (solid), medium-noise case (dash) and high-noise case (dot-dash). a) Improvement factor as a function of insertion loss of the reference scanner. b) The SNR of the system in the uncoated case relative to the system in the coated case.

$$G = \frac{\langle I_{\rm s} \rangle}{s_{\rm ASE}} + 1 \approx 14{\rm dB},$$

where $s_{\rm ASE} = 2n_{sp}h\nu\delta\nu$, and it is noted that the bandwidth of the optical amplifier is assumed to match the light source.

The improvement factor obtained by inserting the amplifier to amplify the light reflected from the sample is plotted in Fig. 6.3a as a function of the insertion loss of the reference system for the coated case. Compared to results given in Figs. 6.1 and 6.2, the improvement is reduced substantially for the medium- and high noise cases due to the reduction of the amplifier gain. However, the obtainable improvement is still substantial for all three cases of the electrical noise. With the modest source power, the added beat noise due to the specular reflection in the uncoated case, is expected to have little influence. This is demonstrated in Fig. 6.3b, where the ratio of the SNR with optical amplification in the coated case to the SNR in uncoated case is plotted.

In summary; The examples of this subsection illustrated the important result that a substantial improvement is obtainable for all three cases of the electrical noise, especially for the important case of low source power and high insertion loss of the reference scanner. This was also observed for the important case, where a wideband light source and amplifier, both

with a limited output power, were considered. Reduction of the specular reflection has a modest effect in this regime, whereas it is clearly seen for higher values of the source power. For the low-noise case, the amplifier was, as expected, seen to be a disadvantage for higher values of source power.

6.1.3 Case 2: High-irradiance light source

In this section, the power of the light source is sufficient to obtain detector saturation limit, and it is assumed that there is no safety limitation on the power impinging on the sample. Accordingly, the examples of this section is related to the theoretical discussion of section 5.5.2. In the saturation limit, the optical noise power will be slightly larger than the receiver noise from the balanced receiver front-end alone. It is then clear that an optical amplifier will not be an advantage in the low-noise case. This case is, therefore, not considered here. The improvement factors in this case are obtained by optimizing the SNR using the design expressions (Eqs.(5.40) in combination with Eq.(5.24)) with and without amplification, respectively.

Optimum source power in a conventional OCT system

Consider an OCT system without amplification that is operated in the saturation limit with the optimum splitting ratio of the first coupler from the light source. Similarly to the discussion of section 5.5.2, an increase in the power of the light source must then be accompanied by an adjustment of the splitting ratio, sending more light towards the sample. This will serve to "spill" the power because of the low reflectivity of the sample relative to the reference. Accordingly, the total optical power impinging on the detectors is kept constant. Since adjusting the split ratio away from optimum will reduce the SNR for constant source power, it may be interesting to investigate whether such an increase in source power is advantageous. This is studied in Fig. 6.4 for an example with a lossless reference scanner. In Fig. 6.4a the split ratio, x, is plotted as a function of $\langle I_\mathrm{s} \rangle$. With an optimum split ratio of 50%, detector saturation is obtained when $\langle I_\mathrm{s} \rangle \approx 4\,\mathrm{mW}$, after which the split ratio is increased. In Fig. 6.4b the SNR of the system is plotted as function of source power relative to the SNR for $\langle I_\mathrm{s} \rangle = 4\,\mathrm{mW}$.

From this graph it can be seen that increasing the source power, and adjusting the split ratio accordingly, is an advantage in the coated case. This is expected in this case, because with the low accumulated incoherent reflectivity of the sample arm the added power from the sample arm impinging on the detector is small relative to the power from the reference. The power to reference arm is therefore kept approximately constant, while the power to the sample is increase with increased source power. However, in the uncoated case, the obtainable improvement is modest because the system quickly reaches the beat noise limit. At approximately $\langle I_{\mathrm{s}} \rangle = 50\mathrm{mW}$ the system saturates in the uncoated case when all the optical power must be sent to the sample resulting in a diminishing SNR. Accordingly, the conclusion of this investigation is that increasing the optical power of the light source beyond the saturation limit is an advantage, at least in the coated case. It is important to note that the advantage of increasing the source power is a feature of the circulator used in the example system. If, instead, the first coupler from the light source was used to transmit the reflected sample light to the balanced detector, the sample transmission coefficient would be $T_s = x(1-x)$. The factor $(1-x)$ will limit the obtainable SNR considerably, as seen in Fig. 6.5 where Fig. 6.4 is replotted with $T_s = x(1-x)$. Accordingly, very little can be gained with additional source power in such a system once detector saturation limit has been obtained. However, it can be shown that the obtainable improvement using an optical amplifier is comparable to that obtainable in the system with a circulator (curves not shown).

Improvement for lossless reference scanner; $R_{\mathbf{R}} = 1$

When an optical amplifier is inserted into a system operating in the detector saturation limit, the additional optical power added by the amplifier must be compensated by a corresponding adjustment in split ratio. This was discussed theoretically in section 5.5.2. Figures 6.6a and 6.6b shows the improvement factor for inserting an optical amplifier into a system with a lossless reference scanner and $\langle I_{\mathrm{s}} \rangle = 4\,\mathrm{mW}$ and $15\,\mathrm{mW}$, respectively. From these graphs it is seen that, depending on the case, a substantial

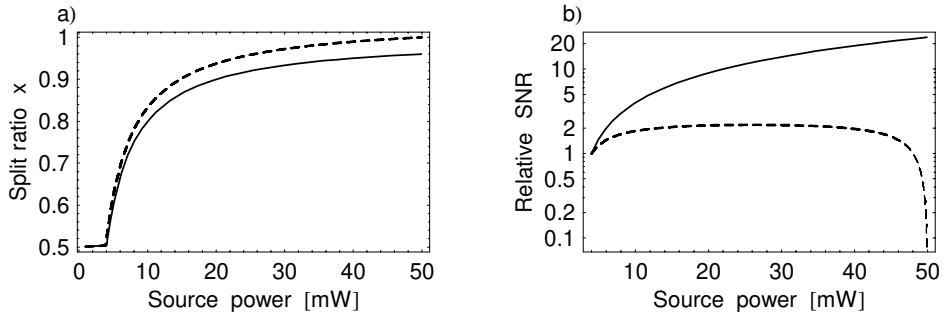

Figure 6.4: Demonstration of the advantage of increased source power in a conventional OCT system with an optical circulator. a) The split ratio x as a function of source power for the coated case (solid) and uncoated case (dash). b) The improvement factor relative to $\langle I_s \rangle = 4\,\mathrm{mW}$ as a function of source power for the coated case (solid) and uncoated case (dash).

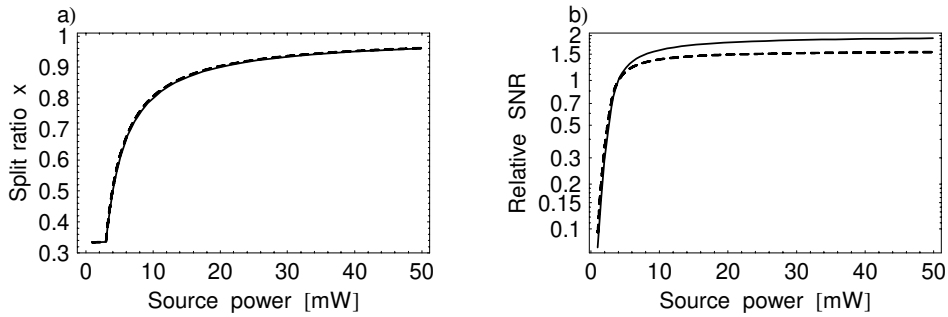

Figure 6.5: Demonstration of the limited advantage of increased source power in a conventional OCT system, where the coupler is reused to transport the sample light to the balanced detector. a) The split ratio x as a function of source power for the coated case (solid) and uncoated case (dash). b) The improvement factor relative to $\langle I_s \rangle = 4\,\mathrm{mW}$ as a function of source power for the coated case (solid) and uncoated case (dash).

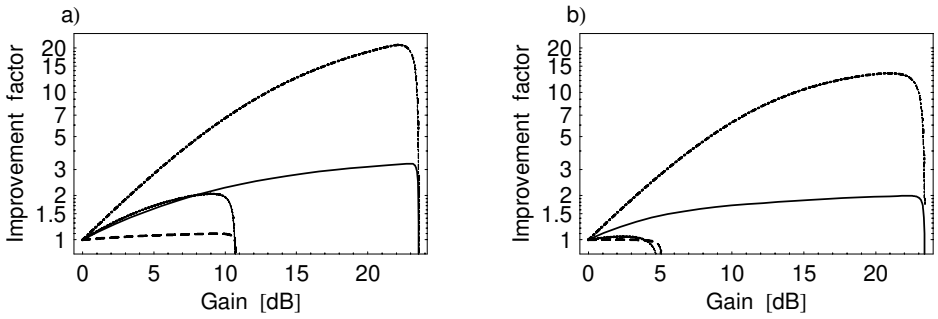

Figure 6.6: Improvement factor for inserting an optical amplifier ($n_{sp} = 2$) in a system where the detectors are just saturated. The electrical noise is considered in medium-noise case (coated case: solid ; uncoated case: dash) and the high-noise case (coated case: dot-dash ; uncoated case: dot). a) $\langle I_s \rangle = 4\,\mathrm{mW}$. b) $\langle I_s \rangle = 15\,\mathrm{mW}$

improvement from inserting the amplifier may be obtained.

As expected from section 5.5.2, the improvement factor increases with the gain of the amplifier until the system is saturated at the *saturation gain* (see section 5.5.2). The saturation gain is found, using Eq.(5.41) and $\langle I_s \rangle = 4\,\mathrm{mW}$, to 23.58 dB and 10.76 dB in the coated and uncoated case, respectively. The saturation gain is relatively modest in the uncoated case, because of the large specular reflection (see Eq.(5.41)). When comparing Figs. 6.6a and 6.6b, a weak dependence on the source power is observed in the coated case, where the obtainable improvement decreases with increasing source power. In the uncoated case, the extra source power results in a reduced saturation gain, as well as a considerable reduction of the improvement factor. This clearly illustrates the importance of reducing the specular reflections of the sample arm for this case. The obtainable improvement factor is, as expected, higher in the high noise case because in this case the added noise due to the optical amplifier is insignificant compared to the electrical noise.

Improvement with an ideal amplifier

The output power of the optical amplifier is, to some degree, dominated by ASE noise. This noise power influences the improvement factor (see

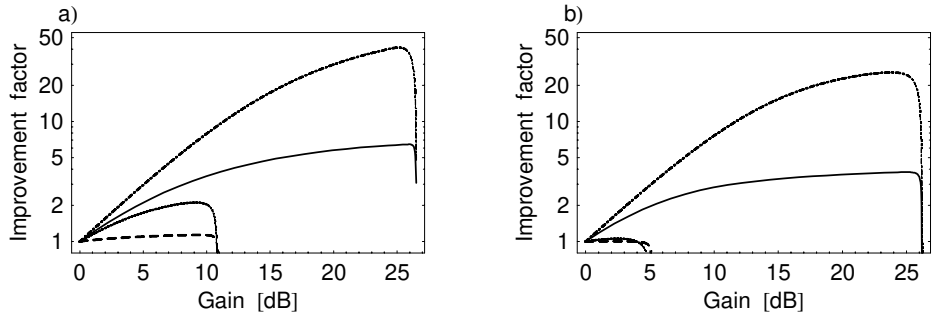

Figure 6.7: Improvement factor for inserting an ideal optical amplifier ($n_{sp} = 1$) in a system where the detectors are just saturated. The electrical noise is considered in medium-noise case (coated case: solid ; uncoated case: dash) and the high-noise case (coated case: dot-dash ; uncoated case: dot). a) $\langle I_s \rangle = 4\,\mathrm{mW}$. b) $\langle I_s \rangle = 15\,\mathrm{mW}$

Eq.(5.42)), saturation gain and the necessary offset from optimum splitting ratio (see Eqs.(5.41) and (5.40)). It is therefore interesting to investigate the effect of inserting an ideal amplifier with $n_{sp} = 1$. Amplifiers with characteristics close to this limit has been obtained for doped-fiber or Raman amplifiers [128].

The effect of the reduced amplifier noise can be seen in Fig. 6.7, where there is a significant increase of the improvement factor and saturation gain for the coated cases. In the uncoated case, the added beat noise masks the reduction in amplifier noise, and therefore little increase in the improvement factor is observed, which is expected from Eq.(5.42). Comparing the uncoated cases plotted in Figs. 6.6 and 6.7, it is seen that the saturation gain is unchanged by the reduction of amplifier noise. This is due to power from the specular reflection dominating the amplifier output, and, therefore, also the saturation gain. Figures 6.6 and 6.7 clearly illustrates the importance of reducing undesired reflections in the sample arm.

Improvement for high insertion loss in the reference scanner ; $R = 0.1$

Finally, consider the important case of a lossy reference scanner. As the split ratio is adjusted to saturation limit; it is expected that the power loss

will result in simple scaling of $\langle I_s \rangle$ compared to the lossless case. However, the extra power of the light source is expected to reduce the improvement factor to some degree by adding optical noise from the sample arm and reducing the saturation gain, especially in the uncoated case (see Eqs.(5.42) and (5.41)). This is illustrated in Fig. 6.8 where the improvement factor is plotted for an insertion loss of 90% of the reference scanner and $\langle I_s \rangle = 40\,\text{mW}$ and $\langle I_s \rangle = 150\,\text{mW}$, respectively. For $\langle I_s \rangle = 150\,\text{mW}$ it can be seen that the improvement factor for the coated case is reduced compared to Fig. 6.7b, whereas little difference is observed between Figs. 6.7a and 6.8a. The reduced saturation gain in the uncoated case is observed in Fig. 6.8a, whereas the detector is saturated even before insertion of the optical amplifier for $\langle I_s \rangle = 150\,\text{mW}$ ($4\% \times 150\,\text{mW}$=6 mW). However, this example illustrated the important result that with the expected scaling of the source power, an insertion loss of the reference scanner yields an increase in the improvement factor for constant source power.

In this context it is important to note that suitable broadband light sources with $\langle I_s \rangle = 40\,\text{mW}$ are very difficult to obtain [23], and that 150 mW is not currently realistic unless the more cumbersome and expensive femto–second laser are used [18]. Approximately 40 mW is the minimum source power for which the detector saturation limit may be obtained unless amplifier noise is substantial. Accordingly, Case 1 is likely to be the case relevant for systems with a high insertion loss in the reference scanner.

In summary; The examples of this subsection illustrated the important result that a substantial improvement may be obtained to a system in detector saturation limit, for the two relevant cases of the electrical noise. As expected, the best improvement was observed for moderate source power and high insertion loss of the reference scanner. However, for high insertion loss; Case 1, rather than the present case, is applicable unless very high irradiance of the light source can be obtained. Case 1 is therefore likely to be the case relevant for fast scanning OCT systems, due to the high insertion loss of suitable optical delay lines [26, 134]. The specular reflection of the uncoated case was observed to reduce the improvement factor, as well as the saturation gain, significantly. This strongly emphasizes the importance

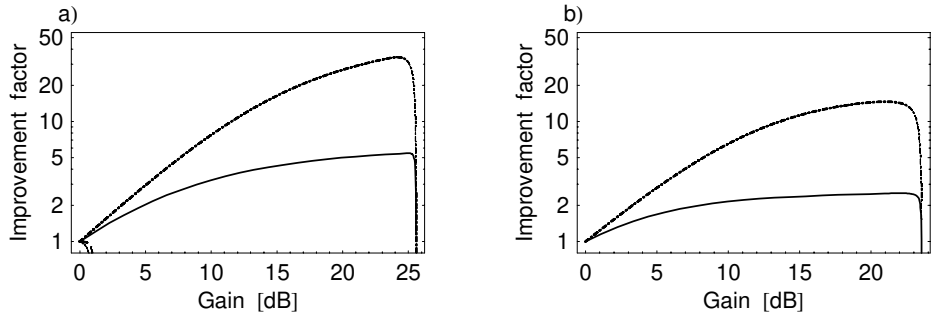

Figure 6.8: Improvement factor for inserting an ideal optical amplifier ($n_{sp} = 1$) in a system where the detectors are just saturated and the reference scanner has a 90% insertion loss. The electrical noise is considered in medium-noise case (coated case: solid ; uncoated case: dash) and the high-noise case (coated case: dot-dash ; uncoated case: dot). a) $\langle I_s \rangle = 40$mW. b) $\langle I_s \rangle = 150$mW

of reducing the specular reflections of the sample arm. Finally, the effect of inserting an ideal amplifier was investigated and shown to give a significant increase in the improvement factor compared to the more noisy amplifier otherwise used. This improvement was only observed in the coated case emphasizing the importance of reducing specular reflections once more.

6.1.4 Case 3: High-irradiance light source and enforced safety limit

In this case, the irradiance of the light source is sufficient to saturate the detector system, while the sample is irradiated with the maximum intensity according to safety considerations. In this case, a system designer will no longer have the option of increasing the split ratio and "spill" the optical power. This case is then particularly important because an increase in source power to improve the SNR is then not possible. As discussed in section 5.5.3, the added optical power by inserting an optical amplifier must be followed by a reduction in source power. This reduction is given by Eq.(5.44) which, in combination with Eq.(5.24), is the design expression for this case.

Improvement for lossless reference scanner; $R_{\mathbf{R}} = 1$

In the following example, the optical amplifier is inserted into a saturated system with a limited irradiation of the sample of 1 mW. This value is chosen rather arbitrarily but has been mentioned as a relevant limit for eye safety for a specific OCT system operating at 800 nm [32].[2] As it turns out, the specific limit has little effect on the improvement factor because the amplifier is assumed to be inserted into a saturated system. However, in the uncoated case, added power in the sample arm will increase the optical noise and therefore reduce the improvement factor (see Eq.(5.47)). An increase in the limitation of the power to the sample also increases the necessary source power to obtain system saturation.

In Figs. 6.9a and 6.9b the improvement factor is plotted as a function of gain for a system with a lossless reference scanner and $n_{sp} = 2$ and $n_{sp} = 1$, respectively. A substantial improvement very similar to Case 2 is observed, but with a reduction caused by the restriction of the split ratio. From section 5.5.3 it is expected that the improvement factor increases with increased gain to a maximum value, after which it decrease. This is confirmed by the plots in Figs. 6.9a and 6.9b. As in Case 2, the specular reflection of the uncoated case reduces the improvement factor and the saturation gain significantly. Reducing the amplifier noise has the opposite effect, and increases the improvement factor and the saturation gain (see Eqs.(5.45) and (5.47)). In Fig. 6.10 the effect of a reduced limit on the power to the sample of 0.1mW is shown. As expected from the discussion above, only the improvement factor in the uncoated case is affected by this change.

Improvement for high reference scanner insertion loss; $R = 0.1$

Finally, consider the case of a lossy reference scanner. As the initial system is assumed saturated, the absolute values of the light from the sample and the reference will be identical to the case of a lossless reference system. Accordingly, there is no change in the improvement factor of such a system

[2] For a cw sources, the specific safety limit will depend on the degree of focusing of the sample beam, exposure duration (i.e. sample scanning speed), and wavelength of the light [141].

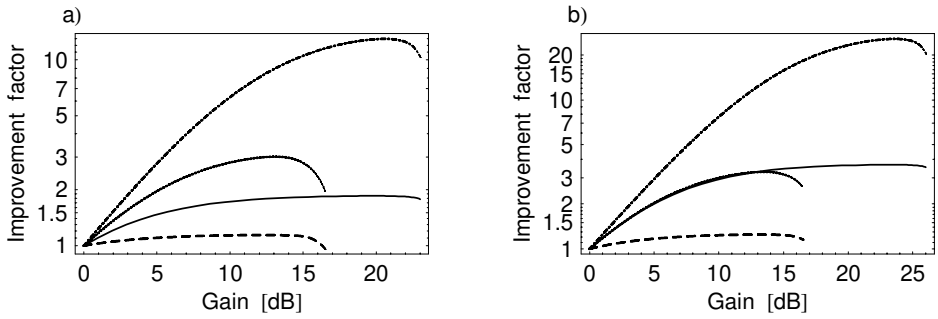

Figure 6.9: Improvement factor for inserting an optical amplifier in a system where the maximum power to the sample is 1 mW and the system is just saturated. The electrical noise is considered in medium-noise case (coated case: solid ; uncoated case: dash) and the high-noise case (coated case: dot-dash ; uncoated case: dot). a) $n_{sp} = 2$. b) $n_{sp} = 1$.

compared to a system with a lossless reference system. However, the required power of the light source to obtain saturation increases, which may render Case 1 relevant, if the source power is limited to a low value. As an example, consider source power requirement for the coated case: With a lossless reference system and a maximum allowable power to the sample of 1mW, the saturation power of the system is approximately 3 mW (1 mW to the sample arm and approximately 2 mW to the reference), whereas the saturation power is 21 mW for an insertion loss of 90%.

In summary; The examples of this subsection illustrated the important result that a saturated OCT system with maximum power to the sample and detectors will be improved by an optical amplifier. This is a particularly important case, because an increase in source power to improve the SNR is impossible. This improvement is, in the coated case, approximately independent of the specific limitations of the power to the sample. An insertion loss of the reference scanner does not change the obtainable improvement, but increases the necessary source power in order to obtain the assumed system saturation.

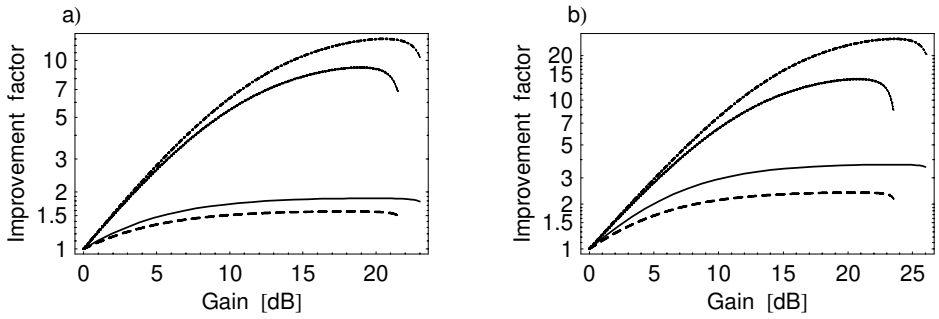

Figure 6.10: Improvement factor for inserting an optical amplifier in a system where the maximum power to the sample is 0.1 mW and the system is just saturated. The electrical noise is considered in medium-noise case (coated case: solid ; uncoated case: dash) and the high-noise case (coated case: dot-dash ; uncoated case: dot). a) $n_{sp} = 2$. b) $n_{sp} = 1$

6.2 Increased penetration depth

It may be shown [17, 40] that if the noise of a system is independent of the light from the probed reflection, $\langle I_{\text{coh}} \rangle$, the SNR may be found as

$$\text{SNR} = \Psi \text{SNR}_0, \tag{6.2}$$

where SNR_0 is the signal-to-noise ratio in the absence of scattering. The quantity Ψ is the heterodyne efficiency factor which was estimated using the new Monte Carlo model of the OCT signal presented in chapter 4. To investigate the increased penetration depth corresponding to an increase in SNR for a realistic application, the heterodyne efficiency factor has been obtained for a skin model using the new Monte Carlo model. The results are plotted as a function of depth z in Fig. 6.11. The reported penetration depth of an OCT system imaging skin is about 1.5 mm at 1300 nm [19]. The parameters for the skin model were obtained from the recent work of Troy *et al.* [142], where 22 human skin samples were measured *in vitro* using a double integrating sphere setup. Unfortunately, parameters were not measured for the individual layers of the skin, but presented as bulk parameters. From the compilation of data by Gemert *et al.* [96], which extends to $\lambda = 800$ nm, it is expected that there is little variation in the scattering

between epidermis and dermis (the two main layers of the skin) and approximately a factor of 10 higher absorption coefficient in the epidermis at longer wavelengths. Here, it is then assumed that the ratio of the absorption coefficient is maintained at 1300nm and that the value of absorption coefficient is dominated by the value for the thicker dermis. Furthermore, the usual very thin stratum corneum is ignored in this context. The skin in then simulated as a two-layer model with a 200 μm thick epidermis on top of a infinitely thick dermis, where the thickness of the epidermis is obtained from an OCT image by Ref. [19]. A scattering coefficient of $\mu_s = 14\,\mathrm{mm}^{-1}$ is assumed common for the epidermis and dermis, whereas the absorption is taken to be $\mu_a = 1\,\mathrm{mm}^{-1}$ and $\mu_a = 0.1\,\mathrm{mm}^{-1}$, respectively. The asymmetry parameter is $g = 0.9$ for both layers. The values for scattering and absorption coefficients are typical values from Ref. [142] and asymmetry factor, g, was taken from Roggan *et al.* [123] and the refractive index was set to 1.37 (water) [143].

If a system has a given maximum penetration depth, this will correspond to a minimum heterodyne efficiency factor, Ψ_{min}. An increase in SNR will correspond to a new minimum heterodyne efficiency factor given by $\Psi = \Psi_{\mathrm{min}}/Q$. Be inspection of Fig. 6.11 it is seen that an increase SNR by a factor of 3 will increase the penetration depth from 1.5 mm to 1.9 mm and an increase by a factor of 10 yields an increase to 2.4 mm. Improvement factors in this order of magnitude was shown for several cases in the preceding sections. Accordingly, an optical amplifier will provide a significant increase in penetration depth when applicable. It is clear that the increase will depend on the specific sample parameters, as well as the initial penetration depth, because of the decreased curve slope for larger depths. Similarly, an optical amplifier may be used to compensate for the reduction in SNR caused by a necessary increase in electrical bandwidth to facilitate faster scanning and/or higher resolution (see the discussion of the improvement factor in section 5.4). This example clearly demonstrates the practical importance that an optical amplifier may have to the use of OCT systems in biomedicine.

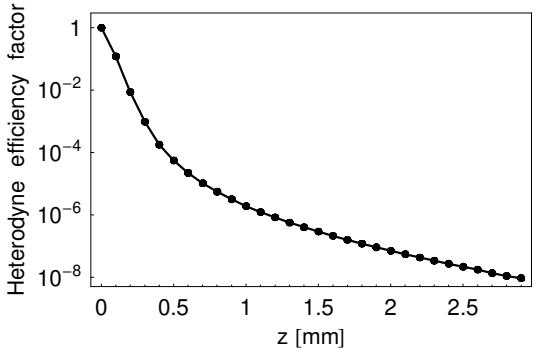

Figure 6.11: The Heterodyne efficiency factor as a function of z for a skin model (see text) obtained using Monte Carlo simulation. The sample beam is described by case 2 of table 3.1.

6.3 The amplified OCT signal: a preliminary measurement

Until now little has been discussed about the influence of an optical amplifier on the coherence of the broadband input and thus resulting shape of the OCT signal. It is clear that a wavelength dependent gain factor will serve to distort the signal, but phase distortion may also play an important role. In this section, the issue of signal shape after amplification will be discussed by studying a preliminary experiment. In this experiment, two erbium-doped-fiber amplifiers with an optical 3 dB bandwidth of 4 nm at 1535 nm were used. The spontaneous emission of the first amplifier is used as the light source, whereas the second amplifier is used to amplify the light from the sample. The gain profile of the amplifiers is not shaped and is therefore relatively far from the ideal Gaussian shape of the light source and a square shape for the amplifier. This, combined with a narrow bandwidth, renders these amplifiers irrelevant for OCT applied in biomedicine. However, erbium-doped fiber amplifiers have been used as light sources in optical low-coherence reflectometry systems applied to optical device testing [37, 144]. Figures 6.12a and 6.12b shows the envelope of the OCT signal without and with amplification of the sample light, respectively. A small distortion, as well as a broadening of the signal shape, can be seen

in the signal with amplification relative to no signal amplification. The 3 dB FWHM width of the signal with amplification is approximately twice that of the signal without amplification (0.38 mm versus 0.18 mm). Accordingly, the resolution obtainable with the system is reduced a factor 2 by insertion of the optical amplifier. However, this reduction is not taken to be a general result, but is expected to depend on the amplifiers ability to amplify all wavelengths of the light source equally. Accordingly, the broadening will depend on the properties of the amplifier relative to the light source. That it is possible to obtain any signal is not surprising, because investigations of an erbium-doped amplifier using a low-coherent reflectometer has been published [6]. However, to the best of my knowledge, this is the first time the coherence properties, i.e., signal shape, of an amplified broadband signal has been investigated. More experimental and theoretical work is necessary to establish the relationship between amplifier properties and signal shape.

The present experiment demonstrates that the overall shape of the OCT signal can be expected to be conserved when an optical amplifier is used to amplify the light from the sample. However, broadening of the signal and a corresponding reduction in resolution is, to some degree, to be expected depending on the properties of the amplifier relative to the light source. It is then up to the specific application whether a (perhaps) small reduction in resolution is tolerable to obtain an increased penetration depth through optical amplification.

6.4 Summary

In this chapter the improvement of the SNR by inserting an optical amplifier in an OCT system was quantified for fast-scanning OCT systems using the new model presented in chapter 5.

In chapter 5 it was shown that the benefit of an optical amplifier is suppression of the electrical noise of the system. Therefore, special attention was given to estimate this parameter for the quantitative analysis. With a commercially available balanced detector front-end, it was shown that optical shot-noise limit may be obtained if the detector is just sat-

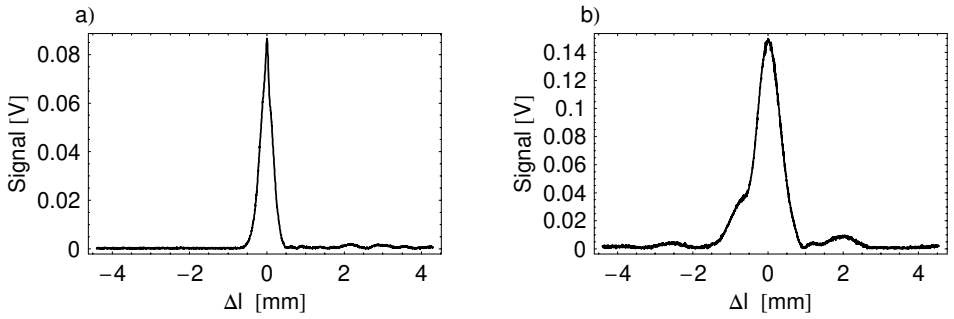

Figure 6.12: OCT signal obtained experimentally in an interferometer with balanced detection. a) Envelope of the OCT signal obtained when an erbium-doped-fiber amplifer is used as light source. b) Envelope of the OCT signal obtained when an identical erbium-doped-fiber amplifer is inserted into the system to amplify the light from the sample arm.

urated. The specific front-end was chosen because of its relatively large bandwidth, so that it may be used in fast scanning OCT systems. This bandwidth is accompanied by a necessary reduction in the electrical gain of the front-end, which in turn renders the system more sensitive to other sources of electrical noise. Therefore, three cases of the total electric noise, i.e., 1, 10, and 100 times the specified receiver noise of the front-end, were investigated. The improvement factor was then investigated for three case of the irradiance of the light source relevant to practical OCT: Case 1, where the irradiance of the light source is limited; Case 2, where the power of the light source if sufficient to saturate the detector system, and Case 3 where a safety limit on the power impinging on the sample also must be considered. Substantial improvement of the SNR of a state-of-the-art balanced OCT system with an optical circulator, was demonstrated using the theoretical model. Improvement were then shown for all three cases of the electrical noise for the important case of a limited power of the light source. The source power is likely to be limited to low values for high resolution applications, where a very wideband light source is required with smooth spectral properties. A reference scanner, with a high insertion loss such as the Fourier-domain rapid-scan optical delay line [14, 24, 31], will significantly increase the power of the light source required to overcome electrical

noise. However, if the source power is sufficient to obtain detector saturation, improvements were shown to be possible for an electrical noise of 10, and 100 times the receiver noise. These improvements were shown to be possible even when the maximum allowable power was incident on the sample. This is a particularly important case, because increasing source power to overcome electrical noise is not possible.

The increased penetration depth due to an increase in SNR was discussed using the Monte Carlo model of the OCT signal presented in chapter 4. Considering the application of OCT to imaging of human skin, it was found that a substantial increase in penetration depth of about 30-100% will be obtained by inserting an optical amplifier when applicable. Similarly, an optical amplifier may be used to compensate for the reduction in SNR caused by a necessary increase in electrical bandwidth to facilitate faster scanning and/or higher resolution (see the introduction to this chapter). Finally, the effect of amplification on the shape of the OCT signal was, as a novelty, investigated through a preliminary laboratory experiment. This experiment demonstrated that the general shape of the OCT signal can be expected to be conserved; however, accompanied with a minor reduction in resolution depending on the properties of the amplifier.

Chapter 7

Conclusion

Two new models of optical coherence tomography (OCT) have been developed. The first model is a Monte Carlo model of the OCT signal, and the second is an analytical model of the signal-to-noise ratio of a system with optical amplification of the reflected light from the sample.

There were three steps to the derivation of the Monte Carlo model :

Firstly, it was proven analytically that by calculating the mixing of the reference and sample beams in the conjugate plane to the probed discontinuity in the sample, the OCT signal may be calculated from the intensity distributions of the respective beams alone. This proved the viability of applying the incoherent Monte Carlo simulation method to an OCT system, because the requirement of coherence information is relaxed. This novel result is one of the main conclusions of this thesis.

Secondly, a new method of simulating focused Gaussian beams was derived and discussed. With this method the correct three-dimensional intensity distribution of a Gaussian beam in free space was achieved, and excellent performance for modeling beam propagation in scattering media was demonstrated. Furthermore, the novel focusing method was shown to be free of the discrepancies of previously published approaches, and this was obtained without increasing the simulation time relative to previous methods. Accordingly, the new method of modeling beam propagation using Monte Carlo simulation may also be valuable as a numerical phantom in its own.

Thirdly, the new expression for the OCT signal was used to derive a so-called detection scheme, which was used to determine the contribution of a single energy packet to the OCT signal. The new detection scheme in combination with the new focusing method constituted the new Monte Carlo model of the OCT signal. The new Monte Carlo model was validated by achieving excellent agreement with results obtained using an analytical model of OCT based on the extended Huygens-Fresenel principle for sample geometries where this model has been validated experimentally. It was demonstrated that the good performance of the model is independent of choice of scattering function, which is crucial because it extends the applicability of the present method to most tissues. Accordingly, it is concluded that the new Monte Carlo model of the OCT signal will perform as a powerful numerical phantom, which may serve as an excellent supplement to the wave equation based analytical OCT model. The Monte Carlo model is thus preferred when the analytical OCT model is either not applicable, too cumbersome to use because of complicated propagation geometries, or when corroborating validity should otherwise be obtained from difficult experiments.

A second analytical model of the signal-to-noise ratio (SNR) was derived to investigate the applicability of optical amplification in OCT. This model was obtained by extending the model of a conventional system to incorporate an optical amplifier. An important result of this analysis was that, although often inferred in the field, the shot-noise limit is only applicable to conventional OCT systems in special cases. Using the new model it was found that an optical amplifier will improve the SNR of a system dominated by receiver noise. Receiver noise, or electrical noise, was identified as being of practical concern, especially because of the often limited irradiance of available optical sources for OCT. It was found that this is emphasized in the important class of fast-scanning systems where receiver noise is likely to be increased, and high insertion loss of the reference scanner reduces the optical power impinging on the detector. To enable use of the model as an aid in system design, the important practical constraints of detector saturation and a safety limit on the irradiation of the sample were,

as a novelty included explicitly, and design expressions for these cases were given. These design expressions are also applicable to systems without optical amplification, and therefore extends the capabilities of the analysis of conventional systems.

Considerable improvement of the SNR was shown for a number of cases of fast scanning systems of practical interest, where the best improvement was obtained when undesired reflections from the optics of the sample arm were reduced to a minimum. Two of the cases were of particular interest. The first case was when the power of the light source was limited, so that receiver noise could not be suppressed by increasing the optical power in the interferometer. This was found particularly critical with high insertion loss of the delay-line scanner in the reference arm. The second case was when the maximum optical power was irradiating the sample, while the limit of detector system was just obtained. In this case the irradiance of the light source could not be increased to suppress receiver noise. Significant improvement in the order of a factor 2-40 of the SNR was demonstrated in each of these cases depending on receiver noise and irradiance of the light source.

It was then demonstrated how an improvement in penetration depth, corresponding to an improvement of the SNR, is quantified using the new Monte Carlo model of the signal. This example demonstrated that an increased penetration of 30% to a 100% can be expected in skin with an improvement of the SNR of a factor of 3 and 10, respectively. Similarly, an optical amplifier may be used to compensate for the reduction in SNR caused by a necessary increase in electrical bandwidth to facilitate faster scanning and/or higher resolution.

Finally, the effect of amplification on the shape of the OCT signal was investigated through a preliminary laboratory experiment. This experiment demonstrated that the general shape of the OCT signal can be expected to be conserved; however, accompanied with a minor reduction in resolution depending on the properties of the amplifier. Accordingly, it is concluded that using an optical amplifier in OCT will have a significant positive impact on system performance in several practical cases, especially for fast scanning systems of the future.

With the demonstrated practical applicability of both presented models, it is concluded that the two new models will pose as valuable tools in future development and optimization of OCT systems resulting extend imaging capabilities within biomedicine.

7.1 Outlook

With the flexibility of the general Monte Carlo simulation method, the new Monte Carlo model of the OCT signal poses as a powerful tool for numerical investigations of OCT systems and beam focusing in tissue. Further use of the Monte Carlo model may entail an examination of the effect of backscattering, and methods to include this property in a model based on the extended Huygens-Fresnel principle may be validated. It would also be interesting to study the feasibility of obtaining the optical parameters of single as well as a multiple layered samples from the OCT signal. Finally, it should be noted that the path-length distribution of photon packets contributing to the OCT signal is easily obtained from the simulations. Using this, it might be possible to investigate the influence of the coherence length of the light source on the signal. Such an investigation would further promote the understanding of the effect of multiple scattering on axial resolution.

With the new noise model, significant improvement from optical amplification was demonstrated theoretically. It is clear that this should be investigated in practice. In this implementation, the results of the new model will determine whether an (perhaps expensive) amplifier will improve this particular system. Furthermore, the model should aid the choice of the split ratio(s) of the coupler(s), and determine to what extent work should be done to reduce undesired reflections in the system. Such considerations are crucial to demonstrate better than state-of-the art performance. Another aspect is the effect of the amplifier on the coherence properties of the amplified signal. This should receive further attention to more accurately establish what amplifier design parameters are important for OCT. Such an understanding may also be of interest to other fields, such as optical communications and remote sensing.

Appendix A

Important results of the extended Huygens-Fresnel principle

The intensity distribution of a Gaussian beam propagating through a scattering sample medium as shown in Fig. A.1 may be written as [49]:

$$\langle I(\mathbf{q})\rangle = \left(\frac{k}{2\pi B}\right)^2 \int K(\boldsymbol{\rho}) \exp\left(\frac{ik}{B}\boldsymbol{\rho}\cdot\mathbf{q}\right) \Gamma_{\mathrm{PT}}(\boldsymbol{\rho})\, d^2\boldsymbol{\rho}. \tag{A.1}$$

Here K is the overlap integral of the unscattered field, U_0, given by

$$K(\boldsymbol{\rho}) = \int \exp\left(-\frac{ikA}{B}\boldsymbol{\rho}\cdot\mathbf{R}\right) U_0(\mathbf{R}+\boldsymbol{\rho}/2)\, U_0^*(\mathbf{R}-\boldsymbol{\rho}/2)\, d^2\mathbf{R}, \tag{A.2}$$

where $\mathbf{r}$ and $\mathbf{r}'$ are coordinates in the r-plane (see Fig. A.1), $\mathbf{R}$ and $\boldsymbol{\rho}$ are sum and difference coordinates given by

$$\mathbf{R}=\frac{1}{2}(\mathbf{r}+\mathbf{r}') \text{ and } \boldsymbol{\rho}=\mathbf{r}-\mathbf{r}' \tag{A.3}$$

and A and B are matrix elements in the $ABCD$ ray matrix for propagation from the r-plane to the q-plane within the sample (see Fig. A.1). Notice, that the q-plane in this case can be any transverse plane within the sample and that each integral are over the entire coordinate plane. The function

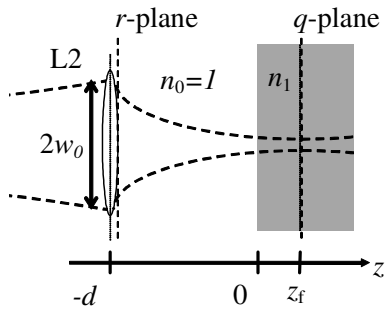

Figure A.1: The modeled geometry.

Γ_{PT} is the mutual coherence function of a spherical wave in the r-plane from a point source in the q-plane, which may be expressed by [47]

$$\begin{aligned} \Gamma_{PT}(\mathbf{r}-\mathbf{r}') &= \langle \exp[i\varphi(\mathbf{r},\mathbf{q}) - i\varphi(\mathbf{r}',\mathbf{q})] \rangle \\ &= \exp\{-\mu_s z[1-b_\varphi(|\mathbf{r}-\mathbf{r}'|)]\} \end{aligned} \tag{A.4}$$

where the function $\varphi(\mathbf{r},\mathbf{q})$ is the stochastic phase added to the phase of a spherical wave propagating from $\mathbf{r}$ to $\mathbf{q}$ due to the scattering medium. The function b_φ is the phase correlation function, and Ref. [17] showed that in the focal plane of a Gaussian beam in a single layered medium with a Gaussian phase function the phase correlation function is given by

$$b_\varphi(x) = \sqrt{\frac{\pi}{2(1-g)}} \frac{n_1 f}{kxz} \operatorname{erf}\left(\sqrt{\frac{1-g}{2}} \frac{kxz}{f}\right) \tag{A.5}$$

where erf () is the error function and n_1 is the refractive index of the sample. For such a propagation geometry $A = 1$ and $B = f$ and it is found that

$$K(\boldsymbol{\rho}) = P_S \exp\left(-\frac{\rho^2}{4w_0^2}\right) \tag{A.6}$$

where P_S is the power of the incident sample beam, w_0 is the initial $1/e$-width of this beam and ρ denotes the length of the vector $\boldsymbol{\rho}$.

The heterodyne efficiency factor, which describes the degradation of the OCT signal due to scattering, may, for the propagation geometry in

question, be shown to be given by [97]

$$\Psi_r = \frac{\int |K(\boldsymbol{\rho})|^2 \, |\Gamma_{\mathrm{PT}}(\boldsymbol{\rho})|^2 \, d^2\boldsymbol{\rho}}{\int |K(\boldsymbol{\rho})|^2 \, d^2\boldsymbol{\rho}}. \tag{A.7}$$

Appendix B

Measured current noise density versus receiver gain

In section 6.1, the importance of the conversion gain of the front-end receiver was discussed. It was argued that due to a necessary reduction in conversion gain for receivers for fast scanning OCT, such systems are more sensitive to external noise sources. To illustrate this fact, an experiment has been performed where the influence of the conversion gain of a balanced detector setup on the current noise spectral density due to electric noise was investigated. The conversion gain is the conversion factor of the input optical power to the output voltage, here calculated assuming a responsitivity of unity. The experiment was performed in the Bio-Optics Lab. at Risø National Laboratory, Denmark.

The setup consisted of two NewFocus 2011 batterty operated photoreceivers with integrated adjustable filters and adjustable conversion gain. Using short SMA cables, these were connected to a battery operated subtraction circuit designed by Finn Petersern, Risø National Laboratory. This subtraction circuit was shielded in a standard electronics box, and efforts were made to avoid ground-loops in the entire setup. The power spectral density of the output of the subtraction circuit was measured using a LeCroy 9304CM Digital Oscilloscope. The instrument noise of the oscilloscope was subtracted by measuring the noise floor of a 50Ω reference, and subtracting the theoretical value for the thermal noise in a resistor [130].

Conv. Gain/V W^{-1}	Noise Power/dBm Hz^{-1}	NEP/W $Hz^{-1/2}$
0.5×10^3	-105.487	1.88×10^{-9}
0.5×10^4	-105.465	1.88×10^{-10}
0.5×10^5	-105.437	2.18×10^{-12}
0.5×10^6	-105.051	1.97×10^{-12}
0.5×10^7	-103.342	0.24×10^{-12}

Table B.1: Measured noise power from a simple balanced receiver consisting of two New Focus 2011 receivers.

The power spectral density was obtained averaging 500 Fourier spectra *spanning* from DC to 125kHz using the ocilloscope. The bandpass filters of the receiver front-ends were set to 100Hz-30kHz, and the frequency span used to obtain the average value of the noise floor were 2kHz-10kHz. The measured data for various values of the conversion of the receiver are given in Table B.1. The total NEP for the system, i.e. both detectors, is calculated using the conversion gain setting as indicated in the table, and that the measured power spectral density (in dBm/Hz) is given as the power dissipated in a 50Ω resistor.

There is a significant constant noise contribution observed in the measurements, which is assumed to be caused by a rather large environmental electrical radiation at the laboratory facilities. From Table B.1 it is seen that for a low conversion gain of the receivers, the constant noise contribution has a significant influence on the NEP of the receiver (NEP=1.88×10^{-9} W $Hz^{-1/2}$), whereas this influence is reduced for higher gains. In fact, the specifications of a single 2011 receiver reports a typical NEP of 1pW $Hz^{-1/2}$ and a minimum NEP of 0.5pW $Hz^{-1/2}$ (reported at highest gain setting) [140], so for noise measurements with a conversion gain larger than 0.5×10^5 the system yields results close to the expected performance.

With the measured data the increased sensitivty of a detector setup with reduced conversion gain is well illustrated. However, because of a relatively open design of the system, it may be extra sensitive to any radiation from the sorrounding environment. Furthermore, a drawback to the setup is that the bandpass filtering occurs after the subtraction circuit. Therefore, these figures should not be considered typical, but merely an

example of the noise sensitivity resulting from a reduced conversion gain of the receiver front-end.

Appendix C

List of symbols

C.1 Chapters 1 through 4

Symbol	Description	Unit
*	Asterix denotes the complex conjugate.	
α	Detector responsivity.	A/W
$\Gamma_{\mathrm{R}}(\cdot)$, $\Gamma_{\mathrm{S}}(\cdot)$	Mutual coherence functions of the reference and sample fields, respectively.	$\mathrm{W/m^2}$
$\Gamma_{\mathrm{PT}}(\cdot)$	The mutual coherence function of a spherical wave in the r-plane from a point source in the q-plane.	$\mathrm{W/m^2}$
$\delta(\cdot)$	Dirac's delta function.	1
ζ, ξ	Pseudo random number evenly distributed between 0 and 1.	1
$\eta(\mathbf{q})$	Complex reflection coefficient on the discontinuity.	1
θ	Polar angle.	rad
θ_{r}	Reflection angle of the diffuse reflector.	rad
θ_{rms}	Root mean square of the scattering angle of the discrete scatterers in the sample.	rad
$\Delta\lambda$	Optical bandwidth of the light source.	m
λ_0	Center wavelength of the light source.	m
μ_{a}	Absorption coefficient of the sample.	$\mathrm{m^{-1}}$
μ_{s}	Scattering coefficient of the sample.	$\mathrm{m^{-1}}$
ν_{c}	Center frequency of the light source.	Hz

Symbol	Description	Unit
$\boldsymbol{\rho}, \tilde{\boldsymbol{\rho}}$	Difference vector of the vectors $\mathbf{r}$ and $\mathbf{r}'$, and $\tilde{\mathbf{r}}$ and $\tilde{\mathbf{r}}'$, respectively.	m
ρ_0	Lateral field correlation length.	m
τ	Time difference of propagation between the reference and sample fields.	s
φ	Azimuthal angle.	rad
φ_r	Azimuthal reflection angle of the diffuse reflector.	rad
$\varphi(\mathbf{q}, \mathbf{r})$	random phase added to the field due to scattering.	1
Ψ, Ψ_r, Ψ_p	Heterodyne efficiency factor. The reduction in signal due to scattering and absorption. A subscript designates the plane where the mixing of sample and reference fields is calculated.	1
Ψ_EHF	Heterodyne efficiency factor calculated using the extended Huygens-Fresnel principle.	1
Ψ_MC	Heterodyne efficiency factor calculated using Monte Carlo simulation.	1
A, B, D	Matrix components in an $ABCD$ matrix.	
A_L2	The area of lens L2.	m^2
B_e	The bandwidth of the electrical receiver circuit.	Hz
C	Constant related to the launch position of a photon.	1
c_n	Normalization constant.	1
d	Distance between focusing lens and the sample.	m
f	Focal length.	m
f_c	Center frequency of the light source.	Hz
$F\{\cdot\}$	Fourier Transform.	1
g	Scattering asymmetry parameter, g=$\cos(\theta_\mathrm{rms})$.	1
$g(\tau)$	Temporal coherence function.	1
G_0	Huygens-Fresnel Green's function for a general $ABCD$ matrix.	1
G_f	Huygens-Fresnel Green's function for propagating the distance f.	1
$G_{r-p}(\mathbf{r}, \mathbf{p})$	Huygens-Fresnel Green's function for propagation of a spherical wave from point $\mathbf{r}$ in the r-plane to point $\mathbf{p}$ in the p-plane.	1
i	Imaginary unit.	1

Symbol	**Description**	**Unit**
$i(t)$	Signal current.	A
$i_0(t)$	Signal current in the absence of random medium in front of the diffusely reflecting discontinuity.	A
$I_{\mathrm{S},m}$	Intensity contribution from the m'th photon packet.	$\mathrm{W/m^2}$
$I_{\mathrm{R}}(\cdot)$,$I_{\mathrm{S}}(\cdot)$	Intensity of the reference and sample fields.	$\mathrm{W/m^2}$
$I_{\mathrm{S},0}(\cdot)$	Intensity of the sample field in the absence of scattering and absorption.	$\mathrm{W/m^2}$
$I_q(\cdot)$	The intensity of the field $U_q(\mathbf{q})$.	$\mathrm{W/m^2}$
k	Wave number $\frac{2\pi}{\lambda_c}$.	$\mathrm{m^{-1}}$
$K(\cdot)$	The overlap integral of the unscattered field in the r-plane.	W
l_{c}	Coherence length of the light source.	m
L_{f}	Mean free path in the scattering medium.	m
n_0, n_1	Refractive index of the sample and surroundings.	1
$p(\theta, \varphi, g)$	Scattering function or phase function of the sample.	1
$\mathrm{p}(r)$	Probability density of finding a photon packet in the radius r at launch.	1
$\mathbf{p}$=(p_x, p_y)	Transverse vector in the p-plane.	m
$P_{\mathrm{R}}, P_{\mathrm{S}}$	Optical power of the reference and sample beams, respectively.	W
Δp^2	Differential area in which a photon packet contributes with intensity.	$\mathrm{m^2}$
q	The lenght of the vector **q.**	m
$\mathbf{q}$=(q_x, q_y)	Transverse vector in the region to the right of the focusing lens. Often inside the sample.	m
$\mathbf{r}$	Vector in the r-plane.	m
r	Length of the vector r.	m
$\mathbf{R}$	Sum vector of the vectors $\mathbf{r}$ and $\mathbf{r}$**´.**	m
R_{d}	Reflectance of the diffuse reflector.	1
s_{tr}	Transport reduced optical depth of the discontinuity.	m
$S(\nu)$	Spectrum of the light source.	W/Hz
$U_r(\mathbf{r})$	Reflected sample field in the r-plane.	V/m

Symbol	Description	Unit
$U_q(\mathbf{q})$	Field impinging upon the discontinuity in the q-plane.	V/m
$U_S(\cdot), U_R(\cdot)$	Sample and reference field, respectively.	V/m
v	Speed of path length change.	m/s
w_m	Weight or energy carried by the m'th photon packet	J
w_0, w_f	$1/e$-width of the beam at the focusing lens (p-plane) and focus, respectively.	m
$w(z)$	$1/e$-width of the beam at the focusing lens as a function of axial distance.	m
$w_\mathrm{photon}(z)$	Axial distance of an unscattered photon packet.	m
z	Position relative to the optical axis.	m
z_0	Rayleigh range of the focused Gaussian beam.	m
z_f	Position of the focal plane relative to the optical axis.	m
Δz, Δq	Grid sizes used to score photon packets in the Monte Carlo simulation.	m

C.2 Chapters 5 and 6

Note: Symbols with subscript b and u refers to quantities related to a balanced and unbalanced setup, respectively. With a subscript, p, the quantity may be taken to be either from the balanced or unbalanced setup depending on the context.

Symbol	Description	Unit
*	An asterix denotes the complex conjugate.	
α	Detector responsivity.	A/W
η	Detector quantum efficiency.	1
θ	Phase constant describing the phase of the beat signal.	1
λ_c	Center wavelength.	m
$\Delta\lambda$	Wavelength band of the light source.	m
ν	The optical center frequency of the light source.	Hz
$\delta\nu$	Optical bandwidth of the light source.	Hz

Symbol	**Description**	**Unit**
φ	Phase delay.	1
a, b	Coupling constants.	1
B_{e}	Bandwidth of the receiver system.	Hz
B_{o}	Bandwidth of the optical amplifier.	Hz
e	The electron charge=$1.60217733 \times 10^{-19}$.	C
f_{c}	Center frequency of the beat signal.	Hz
G	Gain factor of the optical amplifier.	1
G_0	Initial gain when investigating possible improvement due to increased gain.	1
h	Planck's constant $= 6.6260755 \times 10^{-34}$.	J s
i	The imaginary unit.	1
$i\,(t)$	Signal current.	A
$i_1\,(t)$, $i_2\,(t)$	Detector current output due to the fields $U_1(t)$ and $U_2(t)$, respectively.	A
$\langle i_s^2 \rangle$	Mean square signal power.	A^2/Hz
$\langle \Delta i^2 \rangle$	Total mean square noise power.	A^2/Hz
$\langle \Delta i^2_{\mathrm{intr}} \rangle$	Total mean square noise power in the system without optical amplification.	A^2/Hz
$\langle \Delta i^2_G \rangle$	Added mean square noise power due to insertion of an optical amplifier.	A^2/Hz
$\langle \Delta i^2_{\mathrm{rec}} \rangle$	Mean square noise power due to electrical components or coupling in the system.	A^2/Hz
$\langle \Delta i^2_{\mathrm{opt}} \rangle$	Mean square noise power due to light.	A^2/Hz
I_{ASE}	Accumulated intensity of $U_{\mathrm{ASE}}(t)$.	W
I_{coh}	Accumulated intensity of the field coherent with the reference field.	W
$I_{\mathrm{det,max}}$	Maximum power impinging on the detector before saturation or non-linearity in response.	W
$I_{\mathrm{det,tot}}$	Total power impinging on the detector system.	W
I_{s}	Power of the light source.	W
$I_{\mathrm{sam,max}}$	Maximum allowable power towards the sample.	W
$I_{\mathrm{sam}}\,(t)\,, I_{\mathrm{ref}}\,(t)$	Accumulated intensities of the fields U_{sam} and U_{ref},respectively.	W
n_{sp}	Inversion parameter of the optical amplifier.	1

Symbol	**Description**	**Unit**
Q	Improvement factor for insertion of an amplifier.	1
$Q_{\max}$	Maximum possible improvement factor.	1
R_{incoh}	Reflection coefficient expressing the accumulated reflections that are incoherent with the reference field.	1
R_{coh}	Reflection coefficient for the reflection coherent with the reference field.	1
R_{R}	Coefficient describing insertion loss of the reference scanner.	1
$\text{Re}(\cdot), \text{Im}(\cdot)$	Real and imaginary part, respectively.	1
s_{ASE}	Amplifier noise per gain factor above unity.	W/Hz
SNR_{amp}	Signal to noise ratio of the system with optical amplification.	1
SNR_{b},SNR_{u}	Signal-to-noise ratio.	1
t	Time.	s
T	Transport coefficient describing the power loss due to the path from the sample arm to the detector.	1
T_{R}	Transport coefficient relating the power of the light source to the received power from the reference.	1
T_{S}	Transport coefficient relating the power of the light source to the received power from the sample.	1
$T_{\text{R},0}, T_{\text{S},0}$	Transport coefficients for the system without optical amplification.	1
$U_{\text{sam}}(t), U_{\text{ref}}(t)$	Fields propagating toward the detector from the sample and reference arms, respectively.	V/m
$U_1(t)$,$U_2(t)$	Fields incident on detector 1 and 2 in the balanced detector setup.	V/m
$U_{\text{ASE}}(t)$	Output field of the optical amplifier due to amplified spontaneous emission (ASE).	V/m
$U_{\text{coh}}(t)$	Field that is coherent with the reference field.	V/m
$U_{\text{in}}(t)$	Input field to the optical amplifier.	V/m

Symbol	**Description**	**Unit**
$U_{\mathrm{incoh},n}(t)$	n'th field component that is incoherent with the reference field.	V/m
x	Split ration of the first splitter in the interferometer or fraction of the light guided towards the sample.	1
x_{opt}	Optimum splitting ratio given that no constraints are applicable.	1

Bibliography

[1] D. Huang, E. A. Swanson, C. P. Lin, J. S. Schuman, W. G. Stinson, W. Chang, M. R. Hee, T. Flotte, K. Gregory, C. A. Puliafito, and J. G. Fujimoto. Optical coherence tomography. *Science* **254**, 1178–1181 (1991).

[2] B. E. Bouma and G. J. Tearney (Eds.). "Handbook of Optical Coherence Tomography". M. Dekker Inc., New York (2002).

[3] R. C. Youngquist, S. Carr, and D. E. N. Davies. Optical coherence-domain reflectometry: A new optical evaluation technique. *Opt. Lett.* **12**, 158–160 (1987).

[4] K. Takada, I. Yokohama, K. Chida, and J. Noda. New measurement system for fault location in optical waveguide devices based on an interferometric technique. *Appl. Opt.* **26**, 1603–1606 (1987).

[5] K. Takada H. Yamada and M. Horiguchi. Loss distribution measurement of silica-based waveguides by using a jaggedness-free optical low coherence reflectometer. *Electronics Lett.* **30**, 1441–1443 (1994).

[6] K. Takada, M. Oguma, H. Yamada, S. Mitachi, and M. Golling. Gain distribution measurement of an erbium-doped silica-based waveguide amplifier using a complex OLCR. *IEEE Photonics Tech. Lett.* **9**, 1102–1103 (1997).

[7] S. Mechels, K. Takada, and K. Okamoto. Optical low-coherence reflectometer for measuring WDM components. *IEEE Phot. Tech. Lett.* **11**, 857–859 (1999).

[8] Y. Gottesman, E.V.K. Rao, D. Piot, E. Vergnol, and B. Dagens. An in-depth analysis of reflections in MMI couplers using optical low-coherence reflectometry: Design optimization and performance evaluation. *Appl. Phys. B: Lasers and Optics* **73**, 609–612 (2001).

[9] A. F. Fercher, K. Mengedoht, and W. Werner. Eye-length measurement by interferometry with partially coherent-light. *Opt. Lett.* **13**, 186–188 (1988).

[10] C. K. Hitzenberger. Optical measurement of the axial eye length by laser doppler interferometry. *Invest.Ophthalmol.Vis.Sci* **32**, 616–624 (1991).

[11] D. Huang, J. P. Wang, C. P. Lin, C. A. Puliafito, and J. G. Fujimoto. Micron- resolution ranging of cornea anterior-chamber by optical reflectometry. *Lasers Surg. Med.* **11**, 419–425 (1991).

[12] N. Wiener. Generalized harmonic analysis. *Acta Math.* **55**, 117–122 (1930).

[13] J.W. Goodman. "Statistical Optics". John Wiley and Sons, New York (1985).

[14] M. E. Brezinski and J. G. Fujimoto. Optical coherence tomography: High- resolution imaging in nontransparent tissue. *IEEE J. Select. Topics Quantum Electron.* **5**, 1185–1192 (1999).

[15] E. A. Swanson, D. Huang, M. R. Hee, J. G. Fujimoto, C. P. Lin, and C. A. Puliafito. High-speed optical coherence domain reflectometry. *Opt. Lett.* **17**, 151–153 (1992).

[16] J. M. Schmitt. Optical coherence tomography (OCT): A review. *IEEE J. Select. Topics Quantum Electron.* **5**, 1205–1215 (1999).

[17] L.Thrane. "Optical Coherence Tomography: Modeling and Applications". PhD thesis, Risø National Laboratory, Roskilde, Denmark (2001).

[18] B.E. Bouma and G.J.Tearney. Optical sources. In B.E. Bouma and G.J. Tearney, editors, "Handbook of Optical Coherence Tomography", pages 67–97, New York (2002). Marcel Dekker.

[19] J. Welzel. Optical coherence tomography in dermatology: A review. *Skin Research and Tech.* **7**, 1–9 (2001).

[20] B.E. Bouma, G.J. Tearney, S.A. Boppart, M.R. Hee, M.E. Brezinsky, and J.G. Fujimoto. High resolution optical coherence tomographic imaging using a modelocked ti:Al2O3. *Opt. Lett.* **20**, 1486–1488 (1995).

[21] W. Drexler, U. Morgner, F.X. Kartner, C. Pitris, S.A. Boppart, X.D. Li, E.P. Ippen, and J.G. Fujimoto. In vivo ultrahigh-resolution optical coherence tomography. *Opt. Lett.* **24**, 1221–1223 (1999).

[22] I.P. Bilinsky B.E. Bouma, G.J. Tearney, B. Golubovic, and J.G. Fujimoto. Self-phase-modulated kerr lens mode-locked cr:fosterite laser source for optical coherence tomography. *Opt. Lett.* **21**, 1839–1841 (1996).

[23] S. M. Reiss. OCT update: Pushing a promising technology to market. *Biophotonics International* **8**, 40–45 (2001).

[24] A. M. Rollins, M. D. Kulkarni, S. Yazdanfar, R. Ung-Arunyawee, and J. A. Izatt. In vivo video rate optical coherence tomography. *Optics Express* **3**, 219–229 (1998).

[25] J. Szydlo, H. Bleuler, R. Wälti, and R. P. Salatè. High-speed measurements in optical low-coherence reflectometry. *Meas. Sci. Technol.* **9**, 1159–1162 (1998).

[26] A.M. Rollins and J.A. Izatt. Reference optical delay scanning. In B.E. Bouma and G.J. Tearney, editors, "Handbook of Optical Coherence Tomography", pages 99–123, New York (2002). Marcel Dekker.

[27] A. M. Weiner, D. E. Leaird, J. S. Patel, and J. R. Wullert. Programmable femtosecond pulse shaping by use of a multielement liquid-crystal phase modulator. *Opt. Lett.* **15**, 326–328 (1990).

[28] K. F. Kwong, D. Yankelevich, K. C. Chu, J. P. Heritage, and A Dienes. 400-hz mechanical scanning optical delay line. *Opt. Lett.* **18**, 558–560 (1993).

[29] G. J. Tearney, M. E. Brezinski, B. E. Bouma, S. A. Boppart, C. Pitris, J. F. Southern, and J. G. Fujimoto. In vivo endoscopic optical biopsy with optical coherence tomography. *Science* **276**, 2037–2039 (1997).

[30] G. J. Tearney, B. E. Bouma, and J. G. Fujimoto. High speed phase- and group-delay scanning with a grating-based phase control delay line. *Opt. Lett.* **22**, 1811–1813 (1997).

[31] A. M. Rollins, R. Ung-Arunyawee, A. Chak, R. C. K. Wong, K. Kobayashi, M. V. Sivak, and J. A. Izatt. Real-time in vivo imaging of human gastrointestinal ultrastructure by use of endoscopic optical coherence tomography with a novel efficient interferometer design. *Opt. Lett.* **19**, 1358–1360 (1999).

[32] A. Gh. Podoleanu. Unbalanced versus balanced operation in an optical coherence tomography system. *Appl. Opt.* **39**, 173–182 (2000).

[33] M.R. Hee. Optical coherence tomography: Theory. In B.E. Bouma and G.J. Tearney, editors, "Handbook of Optical Coherence Tomography", pages 41–66, New York (2002). Marcel Dekker.

[34] W. V. Sorin and D. M. Baney. A simple intensity noise reduction technique for optical low-coherence reflectometry. *IEEE Photon. Technol. Lett.* **4**, 1404–1406 (1992).

[35] B. E. Bouma and G. J. Tearney. Power-efficient nonreciprocal interferometer and linear-scanning fiber-optic catheter for optical coherence tomography. *Opt. Lett.* **24**, 531–533 (1999).

[36] A. M. Rollins and J. A. Izatt. Optimal interferometer designs for optical coherence tomography. *Opt. Lett.* **24**, 1484–1486 (1999).

[37] K. Takada. Noise in optical low-coherence reflectometry. *IEEE J. of Quant. Electronics* **JQE-34**, 1098–1108 (1998).

[38] J. A. Izatt, M. R. Hee, G. M. Owen, E. A. Swanson, and J. G. Fujimoto. Optical coherence in microscopy in scattering media. *Opt. Lett.* **19**, 590–592 (1994).

[39] J. A. Izatt, M. D. Kulkarni, H. W. Wang, K. Kobayashi, and M. V. Sivak. Optical coherence tomography and microscopy in gastrointestinal tissues. *IEEE J. Select. Topics Quantum Electron.* **2**, 1017–1028 (1996).

[40] L. Thrane, H. T. Yura, and P. E. Andersen. Calculation of the maximum obtainable probing depth of optical coherence tomography in tissue. *Proc. SPIE* **3915**, 2–11 (2000).

[41] J. M. Schmitt, A. Kntittel, and R. F. Bonner. Measurement of optical proper- ties of biological tissues by low-coherence reflectometry. *Appl. Opt.* **32**, 6032–6042 (1993).

[42] M. J. Yadlowsky, J. M. Schmitt, and R. F. Bonner. Multiple scattering in optical coherence microscopy. *Appl. Opt.* **34**, 5699–5707 (1995).

[43] Y. Pan, R. Birngruber, J. Rosperich, and R. Engelhardt. Low-coherence optical tomography in turbid tissue - teoretical analysis. *Appl. Opt.* **35**, 6564–6574 (1995).

[44] Y. Pan, R. Birngruber, and R. Engelhardt. Contrast limits of coherence-gated imaging in scattering media. *Appl. Opt.* **36**, 2979–2983 (1997).

[45] D. J. Smithies, T. Lindmo, Z. Chen, S. Nelson, and T. E. Milner. Signal attenuation and localization in optical coherence tomography studied by monte carlo simulations. *Phys. Med. Biol.* **43**, 3025–3044 (1998).

[46] G. Yao and L.V. Wang. Monte carlo simulation of an optical coherence tomography signal in homogeneous turbid media. *Phys. Med. Biol.* **44**, 2307–2320 (1999).

[47] H. T. Yura. Signal-to-noise ratio of heterodyne lidar systems in the presence of atmospheric turbulence. *Opt. Acta* **26**, 627–644 (1979).

[48] L. Thrane, H. T. Yura, and P. E. Andersen. Analysis of optical coherence tomography systems based on the extended huygens-fresnel principle. *J. Opt. Soc. Am. A* **17**, 484–490 (2000).

[49] H. T. Yura and S. G. Hanson. Optical beam wave propagation through complex optical systems. *J. Opt. Soc. Am. A* **4**, 1931–1948 (1987).

[50] J. G. Fujimoto, C. Pitris, S. A. Boppart, and M. E. Brezinski. Optical coher- ence tomography: An emerging technology for biomedical imaging and optical biopsy. *Neoplasia* **2**, 9–25 (2000).

[51] A. Tycho, T.M. Jørgensen, H.T. Yura, and P.E. Andersen. Derivation of a monte carlo method for modeling heterodyne detection in optical coherence tomography systems. Submitted for publication in Applied Optics (January 2002).

[52] P. E. Andersen, A. O. Bjarklev, and A. Tycho. Optical amplification in coherence reflectometry. Filed as patent application PCT/DK01/00573, September 2001 (Danish patens app. September 2000). Authors are listed alphabetically.

[53] A. Tycho, T. M. Jørgensen, and L. Thrane. Investigating the focusing problem in OCT: Comparison of monte carlo simulations, the extended huygens-fresnel principle and experiments. *SPIE Proc.* **3915**, 25–35 (2000).

[54] S.R. Chinn, E.A. Swanson, and J.G. Fujimoto. Optical coherence tomography using a frequency-tunable optical source. *Opt. Lett.* **22**, 340–342 (1997).

[55] P. E. Andersen, A. O. Bjarklev, and A. Tycho. Optical amplification in coherent optical frequency modulated continuous wave reflectometry. Filed as patent application PCT/DK01/00721, October 2001 (Danish patens app. October 2000). Authors are listed alphabetically.

[56] N. Metropolis and S. Ulam. The monte carlo method. *J. Am. Statistical Association* **44**, 335–341 (1949).

[57] H. Rief, E. M. Gelbard, R. W. Schaefer, and K. S. Smith. Review of monte carlo techniques for analyzing reactor perturbations. *Nucl. Sci. and Eng.* **92**, 289–297 (1986).

[58] E. Egenter, T. Lux, and D. Stauffer. Finite-size effects in monte carlo simulations of two stock market models. *Physica A* **268**, 250–256 (1999).

[59] M. H. Kalos and P. A. Whitlock. "Monte Carlo Methods I: Bascis". John Wiley and Sons, New York (1986).

[60] I. Lux and L. Koblinger. "Monte Carlo Particle Transport Methods: Neutron and Photon Calculations". CRC Press, Boca Raton (1991).

[61] A. Ishimaru. "Wave Propagation and Scattering in Random Media". IEEE Press, New Jersey (1997).

[62] H. Kahn and T. E. Harris. Estimation of particle transmission by random sampling. In "Monte Carlo Method", volume 12. U. S. Government Printing Office (1951).

[63] B. C. Wilson and G. Adam. A monte carlo model for the absorption and flux distributions of light in tissue. *Med. Phys.* **10**, 824–830 (1983).

[64] S.T. Flock, B.C. Wilson, and M.S. Patterson. Monte carlo modeling of light propagation in highly scattering tissues II: Comparison with measurements in phantoms,. *IEEE Trans. Biomed. Eng.* **36**, 1169–1173 (1989).

[65] S. A. Prahl, M. Keijzer, S. L. Jacques, and A. J. Welch. A monte carlo model for light propagation in tissue. *Dosimetry of Laser Radiation in Medicine and Biology, SPIE Institute Series* **IS 5** (1998).

[66] L.-H. Wang, S. L. Jacques, and L.-Q. Zheng. MCML - monte carlo modeling of photon transport in multi-layered tissues. *Computer Methods and Programs in Biomedicine* **47**, 131–146 (1995).

[67] A. H. Hielscher, L. Hanli, B. Chance, F. K. Tittel, and S. L. Jacques. Time-resolved photon emission from layered turbid media. *Appl. Opt.* **35**, 719–728 (1996).

[68] E. Okada, M. Schweiger, S. R. Arridge, M. Firbank, and D. T. Delpy. Experimental validation of monte carlo and finite-element methods for the estimation of the optical path length in inhomogeneous tissue. *Appl. Opt.* **35**, 3362–3371 (1996).

[69] L. Bergougnoux. Monte carlo calculation of backscattered light intensity by suspension: Comparison with experimental data. *Appl. Opt.* **35**, 1735–1741 (1996).

[70] E. Okada, M. Firbank, M. Schweiger, S. R. Arridge, M. Cope, and D. T. Delpy. Theoretical and experimental investigation of near-infrared light propagation in a model of the adult head. *Appl. Opt.* **36**, 21–31 (1997).

[71] F. Bevilacqua, P. Marquet, O. Coquoz, and C. Depeursinge. Role of tissue structure in photon migration through breast tissues. *Appl. Opt.* **36**, 44–51 (1997).

[72] R. J. Crilly, W.-F. Cheong, B. Wilson, and J. R. Spears. Forward adjoint fluorescence model: Monte carlo integration and experimental validation. *Appl. Opt.* **36**, 6513–6519 (1997).

[73] A. Pifferi, P. Taroni, G. Valentini, and S. Andersson-Engels. Real-time method for fitting time-resolved reflectance and

transmittance measurements with a monte carlo model. *Appl. Opt.* **37**, 2774–2780 (1998).

[74] P. Y. Sinichkin, R. S. Utz, A. H. Mavliutov, and H. A. Pilipenko. In vivo fluorescence spectroscopy of the human skin: Experiments and models. *J. of Biomed. Opt.* **3**, 201–211 (1998).

[75] M. Johns, C. A. Giller, and H. Liu. Theoretical and in-vivo investigation of optical reflectance from human brain to assist neurosurgery. *J. of Biomed. Opt.* **3**, 437–445 (1998).

[76] C.-L. Tsai, Y.-F. Yang, C.-C. Han, J.-H. Hsieh, and M. Chang. Measurement and simulation of light distribution in biological tissues. *Appl. Opt.* **40**, 5770–5777 (2001).

[77] A. Talsma, B. Chance, and R. Graaff. Corrections for inhomogeneities in biological tissue caused by blood vessels. *J. Opt. Soc. Am. A* **18**, 932–939 (2001).

[78] M. Kobayashi, Y. Ito, N. Sakauchi, I. Oda, I. Konishi, and Y. Tsunazawa. Analysis of nonlinear relation for skin hemoglobin imaging. *Optics Express* **9**, 802–812 (2001).

[79] I. V. Yaroslavsky, A. N. Yaroslavsky, V. V. Tuchin, and H.-J. Schwarzmaier. Effect of the scattering delay on time-dependent photon migration in turbid media. *Appl. Opt.* **36**, 6529–6538 (1997).

[80] F. Martelli, D. Contini, A. Taddeucci, and G. Zaccanti. Photon migration through a turbid slab described by a model based on diffusion approximation. II. comparison with monte carlo results. *Appl. Opt.* **36**, 4600–4612 (1997).

[81] A. Kienle, M. S. Patterson, N. Dögnitz, R. Bays, G. Wagnières, and H. Van Den Bergh. Noninvasive determination of the optical properties of two-layered turbid media. *Appl. Opt.* **37**, 779–791 (1998).

[82] G. Alexandrakis, T. J. Farrell, and M. S. Patterson. Monte carlo diffusion hybrid model for photon migration in a two-layer turbid medium in the frequency domain. *Appl. Opt.* **39**, 2235–2244 (2000).

[83] A. Kienle, F. K. Forster, and R. Hibst. Influence of the phase function on determination of the optical properties of biological tissue by spatially resolved reflectance. *Opt. Lett.* **26**, 1571–1573 (2001).

[84] F. Martelli, A. Sassaroli, Y. Yamada, and G. Zaccanti. Analytical approximate solutions of the timedomain diffusion equation in layered slabs. *J. Opt. Soc. Am. A* **19**, 74–80 (2002).

[85] J. R. Zijp and J. J. Ten Bosch. Anisotropy of volume-backscattered light. *Appl. Opt.* **36**, 1671–1680 (1997).

[86] G. Alexandrakis, T. J. Farrell, and M. S. Patterson. Accuracy of the diffusion approximation in determining the optical properties of a two-layer turbid medium. *Appl. Opt.* **37**, 7401–7409 (1998).

[87] J. Qu and B. C. Wilson. Monte carlo modeling studies of the effect of physiological factors andother analytes on the determination of glucose concentration in vivoby near infrared optical absorption and scattering measu. *J. of Biomed. Opt.* **2**, 319–325 (1997).

[88] M. Moscoso, J. B. Keller, and G. Papanicolaou. Depolarization and blurring of optical images by biological tissue. *J. Opt. Soc. Am. A* **18**, 948–960 (2001).

[89] S. L. Jacques and L. H. Wang. Monte carlo modeling of light transport in tissue. In A. J. Welch and M. J. C. Van Gemert, editors, "Optical Thermal Response of Laser Irradiated Tissue", New York (1995). Plenum Press.

[90] C.F. Bohren and D. R. Huffman. "Absorbtion and Scattering of Light by Small Particles". John Wiley and Sons, New York (1998).

[91] H. C. Van de Hulst. "Light Scattering by Small Particles". John Wiley and Sons, New York (1957).

[92] A. Tycho and T. M. Jørgensen. Comment on 'excitation with a focused, pulsed optical beam in scattering media: Diffraction effects. *Accepted for publication in Appl. Opt.* (2001).

[93] V. R. Daria, C. Saloma, and S. Kawata. Excitation with a focused, pulsed optical beam in scattering media: Diffraction effects. *Appl. Optics* **39**, 5244–5255 (2000).

[94] J. M. Schmitt and A. Kntittel. Model of optical coherence tomography of heterogeneous tissue. *J. Opt. Soc. Am. A.* **14**, 1231–1242 (1997).

[95] F. Lexer, C. K. Hitzenberger, W. Drexler, S. Molebny, H. Sattmann, M. Sticker, and A. F. Fercher. Dynamic coherent focus OCT with depth independent transversal resolution. *J. Mod. Opt.* **46**, 541–553 (1999).

[96] M. J. C. Van Gemert, S. L. Jacques, H. J. C. M. Sterenborg, and W. M. Star. Skin optics. *IEEE Trans. Biomed. Eng.* **36**, 1146–1154 (1989).

[97] H. T. Yura, L. Thrane, and P. E. Andersen. Closed-form solution for the wigner phase-space distribution function for diffuse reflection and small-angle scattering in a random medium. *J. Opt. Soc. A* **17**, 2464–2474 (2000).

[98] H. T. Yura and S. G. Hanson. Effects of receiver optics contamination on the performance of laser velocimeter systems. *J. Opt. Soc. Am. A.* **13**, 1891–1902 (1996).

[99] R. F. Lutomirski and H. T. Yura. Propagation of a finite optical beam in an inhomogeneous medium. *Appl. Opt.* **10**, 1652–1658 (1971).

[100] N. Bloembergen. Laser-induced electric breakdown in solids. *EEE J. of Quant. Elec.* **QE-10**, 375–386 (1974).

[101] J. Manyak, A. Russo, P. Smith, and E. Glatstain. Photodynamic therapy. *J. Clin. Oncol.* **6**, 380–391 (1988).

[102] Z. Song, K. Dong, X.H. Hu, and J. Q. Lu. Monte carlo simulation of converging laser beams propagating in biological materials. *Appl. Opt.* **38**, 2944–2949 (1999).

[103] J.M. Schmitt, A. Knüttel, and M. Yadlowski. Confocal microscopy in turbid media. *J. Opt. Soc. A* **11**, 2226–2235 (1994).

[104] J. M. Schmitt and K. Ben-Letaief. Efficient monte carlo simulation of confocal microscopy in biological tissue. *J. Opt. Soc. Am. A* **13**, 952–961 (1996).

[105] A. K. Dunn, C. Smithpeter, A. J. Welch, and Rebecca Richards-Kortum. Sources of contrast in confocal reflectance imaging. *Appl. Opt.* **35**, 3441–3446 (1996).

[106] C. M. Blanca and C. Saloma. Monte carlo analysis of two-photon fluorescence imaging through a scattering medium. *Appl. Opt.* **37**, 8092–8102 (1998).

[107] C. M. Blanca and C. Saloma. Efficient analysis of temporal broadening of a pulsed focused gaussian beam in scattering media. *Appl. Opt.* **38**, 5433–5437 (1999).

[108] L.V. Wang and G. Liang. Absorption distribution of an optical beam focused into a turbid medium. *Appl. Opt.* **38**, 4951–4958 (1999).

[109] Yu. D. Berezin and S. A. Eremenko. Use of the monte carlo method for calculating the three-dimensional distribution of laser radiation with wavelengths of 1.06 and 2.09 ţm in biological tissues. *J. Opt. Technol.* **67**, 139–142 (2000).

[110] Yu. D. Berezin and S. A. Eremenko. Use of the monte carlo method for calculating the three-dimensional distribution of laser radiation with wavelengths of 1.06 and 2.09 micrometers in biological tissues. *J. Opt. Technol.* **67**, 139–142 (2000).

[111] A. Tycho. Modeling of a focused beam in a semi-infinite highly scattering medium. *SPIE Proc.* **3597**, 118–129 (1999).

[112] B. E. A. Saleh and M.C. Teich. "Fundamentals of Optics". John Wiley and Sons, New York (1991).

[113] H. T. Yura. Private communications. (1999).

[114] L. G. Henyey and J. L. Greenstein. Diffuse radiation in the galaxy. *Astro- physical J.* **93**, 70–83 (1941).

[115] W. Cheong, S. Prahl, and A. J. Welch. A review of the optical properties of biological tissues. *IEEE J. of Quant. Elec.* **26**, 2166–2185 (1990).

[116] W. Denk, J. Strickler, and W. Webb. Two-photon laser scanning fluorescence microscopy. *Science* **248**, 73–76 (1990).

[117] A. E. Siegman. "Lasers". University Science Books, Mill Valley (1986).

[118] C. Sturesson and S. Andersson-Engels. Mathematical modeling of dynamic cooling and pre-heating, used to increase the depth of selective damage to blood vessels in laser treatment of port wine stains. *Phys. Med. Biol.* **41**, 413–428 (1996).

[119] H. T. Yura and S. G. Hanson. Second-order statistics for wave propagtion through complex optical systems. *J. Opt. Am. A* **6**, 564–575 (1989).

[120] S. L. Jacques, C. A. Alter, and S. A. Prahl. Angular dependence of he-ne laser light scattering by human dermis. *Lasers Life Sci.* **1**, 309–333 (1987).

[121] A. E. Siegman. The antenna properties of optical heterodyne receivers. *Appl. Opt.* **5**, 1588–1594 (1966).

[122] J. W. Goodman. "Introduction to Fourier Optics". McGraw-Hill, New York (1996).

[123] A. Roggan, J. Beuthan, S. Schrunder, and G. Mueller. Diagnostik und therapie mit dem laser. *Phys. Bl.* **55**, 25–30 (1999).

[124] L. Thrane, H. T. Yura, and P. E. Andersen. Calculation of the maximum obtainable probing depth of optical coherence tomography in tissue. *Proc. SPIE* **3915**, 2–11 (2000).

[125] G. P. Agrawal and N. K. Dutta. "Semiconductor Lasers". Kluwer Academic Press, Dordrecht (1993).

[126] T. Okoshi and K. Kikuchi. "Coherent Optical Fiber Communications". Kluwer Academic Publishers, Dordrecht (1988).

[127] N. A. Olson. Lightwave systems with optical amplification. *IEEE J. of Lightw. Tech.* **7**, 1071–1082 (1989).

[128] P. C. Becker, N. A. Olsson, and J. R. Simpson. "Erbium-Doped Fiber Amplifiers". Academic Press, San Diego (1999).

[129] A. Bjarklev. Private communications. (2002).

[130] G. P. Agrawal. "Fiber-Optic Communication Systems". John Wiley and Sons, New York (1997).

[131] N. Jolley J. D. Minelly and Y. Nakano, editors. "Trends in Optics and Photonics Series, Optical Amplifiers and their Applications", volume 60. OSA (2001).

[132] S. Jiang and R. W. Keys, editors. "Rare-Earth-Doped Materials and Devices VI", volume 4645. SPIE (2002).

[133] S. Ryu. "Coherent Lightwave Communication Systems". Artech House, Norwood (1995).

[134] L. Thrane. Private communications. (2002).

[135] J. Singh. "Semiconductor Optoelectronics". McGraw-Hill, London (1995).

[136] S. Ramo, J. R. Whinnery, and T. Van Duzer. "Fields and Waves in Communication Electronics". John Wiley and Sons, New York (1965).

[137] P. E. Green. "Fiber Optics Networks". Prentice-Hall, New Jersey (1993).

[138] Xingde Li, W. Drexler, C. Pitris, R. Ghanta, C. Jesser, J. Herrmann, D. Stamper, D. Golden, S. Martin, J. G. Fujimoto, and M. Brezinski. Imaging of osteoarthritic cartilage with optical coherence tomography: Micron-structure and polarization sensitivity. In "Summaries of Papers Presented at the Conference on Lasers and Electro-Optics, 1999", page 339. Opt. Soc. America.

[139] New focus corporation: Online product catalog (www.newfocus.com) (2002).

[140] New focus models 2001 and 2011 user's manual: Front-end optical receivers. **200110 Rev. B** (2001).

[141] J. A. Izatt, A. M. Rollins, R. Ung-Arunyawee, and S. Yazdanfar. System integration and signal/image processing. In B.E. Bouma and G.J. Tearney, editors, "Handbook of Optical Coherence Tomography", pages 143–174, New York (2002). Marcel Dekker.

[142] T. L. Troy and S. N. Thennadil. Optical properties of human skin in the near infrared wavelength range of 1000 to 2000 nm. *J. of Biomed. Opt.* **6**, 167–176 (2001).

[143] P. Ray. Broadband complex refractive indices of ice and water. *Appl. Opt.* **11**, 1836–1844 (1972).

[144] K. Takada and H. Masaharu. Jaggedness-free millimeter-resolution low coherence reflectometry. *J. of Lighwave Tech.* **12**, 658–663 (1994).